University of Alberta

High Surface Area Nanoelectromechanical Systems via the Integration of Glancing Angle Deposition Thin Films

by

Jocelyn N. Westwood

A thesis submitted to the Faculty of Graduate Studies and Research
in partial fulfillment of the requirements for the degree of

Master of Science
in
Microsystems and Nanodevices

Department of Electrical and Computer Engineering

Fall 2013
Edmonton, Alberta

To my parents Laurie and Bill, for encouraging my pursuit of graduate studies.
And to Danny, for always having faith in me.

Abstract

High surface area nanoelectromechanical systems (NEMS) are fabricated using glancing angle deposition (GLAD) thin films as the high surface area layer. The GLAD films are deposited on already-released NEMS cantilevers and doubly clamped beams (DCBs) with good uniformity. The resonance frequencies of the coated devices are lower than uncoated NEMS due to mass loading. The resonance frequencies of the coated cantilevers can be predicted accurately. The resonance frequencies of the DCBs are difficult to predict because of compressive stress in the substrate from which the devices are fabricated. The quality factors of the coated devices are approximately one order of magnitude smaller than the uncoated devices due to a semi-continuous layer at the base of the GLAD film. The GLAD film introduces a compressive stress of 5.3–9.3 MPa. The quantification of the stress introduced by the GLAD indicates that these devices may also be useful as stress sensors.

Acknowledgements

I would like to thank my supervisor Dr. Jeremy Sit for his advice throughout my program. The members of the ENL Lab, Dr. Jonathan Kwan and Graham Hunt, gave valuable advice and helped orient me to the lab when I began this journey two years ago. Thanks also go out to the members of the GLAD lab, especially Allan Beaudry for many hours of SEM imaging and training on the deposition systems. Joshua Siewert, who kept me guessing about the fridge. Steven Jim, Dr. Jason Sorge, Ben Bathgate, and Ryan Shewchuk, for providing entertaining lunch hours saving the world and practicing the art of deception.

This project would not have been possible without the resources provided by Dr. Wayne Hiebert and his group. Thanks to Vincent Sauer and Dr. Zhu Diao for help with fabrication process development and teaching me how to use the lab equipment. Thanks especially to Wayne for the use of the optical interferometry system and the insightful discussions.

There were many staff members at the University of Alberta who contributed to this project. I would like to acknowledge the significant contribution of George Braybrook, who ran the SEM and helped me to diagnose many of the issues with my devices. Thanks also to the NanoFab staff, especially Jolene Jalota, Scott Munro, Stephanie Bozic, and Les Schowalter who trained me on many different systems.

My family and friends were an invaluable source of support and encouragement throughout my M.Sc. I would especially like to thank my parents Laurie and Bill. They have always encouraged me to learn more, be curious, and chase my dreams. Without that encouragement I very much doubt I would have had the courage to pursue graduate studies. I am also grateful to my wonderful fiancée Danny for his endless patience, love, and support.

I would like to thank my financial supporters, the Natural Science and Engineering Research Council of Canada, Alberta Innovates Technology Futures, and the Canadian Federation of University Women. With the support of these agen-

cies, I was able to pursue my research wholeheartedly. Finally, I am grateful to the University of Alberta, the Faculty of Engineering, and especially the Department of Electrical and Computer Engineering for providing me with a welcoming place to study and grow. I have been given many opportunities to volunteer on campus, and as a result have met many amazing people. I am truly grateful for the many opportunities provided by the Faculty and the Department.

Contents

1 Introduction **1**

1.1 Motivation 1

1.2 Outline 4

2 Background **5**

2.1 Nanoelectromechanical Systems 5

2.1.1 Resonance Frequencies 6

2.1.2 Phase Shifts 12

2.1.3 Quality Factor 13

2.1.4 Nanoelectromechanical Systems as Sensors 16

2.2 Glancing Angle Deposition 18

2.2.1 Incorporating GLAD into Devices 21

2.3 Combining GLAD and NEMS 22

2.3.1 Similar High Surface Area Devices in the Literature 23

3 Fabrication and Characterization of High Surface Area Nanomechanical Devices **24**

3.1 Fabrication Process Flow 24

3.2 Fabrication Challenges 29

3.2.1 Clumping 29

3.2.2 Edge Effects 30

3.2.3 Surface Residues 32

3.3 Device Design 35

3.4 Characterization Techniques 37

3.4.1 Scanning Electron Microscopy 39

3.4.2 Optical Interferometry 40

4 Results and Analysis for NEMS **43**

4.1 Cantilevers 48

4.1.1 Quality Factor 49

4.1.2 Resonance Frequencies 52

4.1.3 Phase . . . 53
4.2 Doubly Clamped Beams . . . 53
4.2.1 Resonance Frequencies . . . 54
4.2.2 Quality Factor . . . 57
4.2.3 Phase . . . 60
4.3 Summary of NEMS Analysis . . . 61

5 Results and Analysis for GLEMS **62**
5.1 Quality Factor . . . 63
5.2 Resonance Frequencies . . . 67
5.2.1 Cantilevers . . . 67
5.2.2 Doubly Clamped Beams . . . 76
5.3 Phase . . . 79
5.4 Summary of GLEMS Analysis . . . 81

6 Conclusions **82**
6.1 Directions for Future Work . . . 83
6.2 Summary . . . 84

Bibliography **85**

A Gnuplot Curve Fitting **92**

List of Figures

2.1 Schematic of a doubly clamped beam. L is the length of the beam, w is the width, and t_b is the thickness. The coordinate system is also labeled, with the origin at one end of the beam. 8

2.2 Schematic of a singly clamped beam, or cantilever. L is the length of the beam, w is the width, and t_b is the thickness. The coordinate system is also labeled, with the origin at the base of the cantilever. . 12

2.3 A schematic of the GLAD deposition process. The deposition angle is labeled α and the substrate rotation is described by ϕ. Figure reproduced with permission from [1]. 19

2.4 A schematic of the shadowing phenomenon. The incident flux cannot deposit in the shadowed region as that area is blocked by the existing structures. Figure reproduced with permission from [2]. 19

2.5 Illustration of columnar structures adding little mechanical contribution to NEMS resonators: (a) a coated device without bending; (b) the same device under flexural motion. Ideally, the pillars will not interact. 22

3.1 A schematic of the process flow used to fabricate the GLEMS. (a) Diced and cleaned and SOI chip. (b) ∼140 nm of ZEP 520A resist spin coated on. (c) Resist patterned with EBL, then developed. (d) ICPRIE used to etch Si. (e) Resist removed with Remover PG and O_2 plasma etch. (f) BOE etch removes BOX and releases devices. (g) GLAD deposited on released NEMS to create GLEMS. 25

3.2 Top-down SEM image of a NEMS cantilever, 400 nm wide, 3.5 μm long, 145 nm thick. 27

3.3 Top-down SEM image of a GLEMS cantilever, 400 nm wide and 3.75 μm long. 28

3.4 Illustration of the design to eliminate edge effects. (a) shows the view of the devices from a low incident angle, and (b) shows the view at a high incident angle, close to 90°. Note that the device outline essentially vanishes at a high incident angle, meaning that the incident flux sees a nearly planar substrate. 31

3.5 The test structure used to determine the optimal gap width, coated with ∼300 nm of GLAD SiO_2 vertical posts. (a) shows both the 300 nm and 250 nm widths. The line on the left has a gap of 300 nm, and edge effects are visible on the outline of the structure. The line on the right has a gap width of 250 nm. Edge effects are not noticeable here. (b) is a zoomed-in image of the 250 nm width only, and shows minimal edge effects at high magnification. 31
3.6 A DCB destroyed by the presence of surface residues. Note the non-uniform GLAD deposition that causes the GLAD to grow in the gap between the beam and the substrate. No oxygen plasma etches were used in the fabrication of this beam, and a pentane release method was used instead of critical point drying. 32
3.7 SEM images of buckled DCBs. (a) shows a beam that is buckled up, and (b) shows a beam that is buckled down. In both cases the shadowing of the GLAD films provides a stong indicator of the device failure. These DCBs were fabricated near each other on the same chip. 33
3.8 Schematic of the devices written using the Raith 150-TWO software. The rightmost image shows all of the devices written in each session. The modified devices are visible in the array labelled "Test" in this schematic. The array on the top left is the cantilever array. All devices of the same length are labelled alphabetically, and each column is labelled numerically, giving a unique designation for each device. The DCBs measured are shown at the bottom left of the figure, with an identical naming scheme. 35
3.9 SEM images of devices with narrowed clamping points. (a) shows a doubly clamped beam with 100 nm wide clamping points coated with 300 nm of GLAD vertical posts deposited at 86°. (b) is a cantilever with a 100 nm wide clamping point coated with 100 nm of GLAD vertical posts deposited at 86°. (c) A zoomed-out view of an uncoated NEMS device with no support pad. Notice the square etched around the outside, designed to limit any coupling of vibrations between devices. 37
3.10 Measurements of the reflectance of an uncoated SOI sample compared to the reflectance of a SOI substrate coated with ∼300 nm of GLAD SiO_2 vertical posts deposited at 86° over a range of wavelengths at a 20° angle of incidence. At a wavelength of 633 nm, the reflectances of the two samples are within error, indicating that scattering is negligible in the optical interferometry measurements. 39

3.11 Schematic of the optical interferometry setup. The HeNe laser self-interferes when focused on the NEMS. The resonance signal is detected by the photodiode. The devices are mechanically actuated by a piezoelectric disk and read out using a network analyzer. Figure courtesy of Vincent Sauer; used with permission. 41

4.1 A sample resonance curve for a 3.5 μm long cantilever with no GLAD coating. The black curve shows that amplitude response and the blue curve shows the phase response. The inset shows the curve fit to the amplitude. The solid red line is the fit. 44

4.2 A standard NEMS DCB with nominal length 8 μm. The red arrow shows the bright line that is the edge of the undercut caused by the BOE etch. The blue arrows show the points between which the length measurements were taken. 45

4.3 Measured length plotted versus the nominal length for (a) cantilevers and (b) DCBs. The slopes of both are very near 1. When the slope of forced to 1, the intercepts provide insight into the magnitude of the undercut. 47

4.4 Quality factors of uncoated cantilevers. There are two trends in the data, one increasing as the length increases, and one decreasing as the length increases. The latter has a significantly lower Q. 49

4.5 Comparison of quality factors of devices before and after SEM imaging. Column 2 devices show a substantial decrease in quality factor compared to devices of all other columns, indicating that damage during SEM imaging may be the cause of a decrease in Q. 50

4.6 Resonance frequency plotted versus length of uncoated cantilevers. The data was fit using Equation 2.10 with the thickness of the device layer as the fitting variable. This produced a thickness of 147.5 $\pm$ 0.3 nm, well within the specifications of the SOI wafer. 52

4.7 The phase shift for a 3.5 μm long cantilever has been plotted in polar coordinates. The phase goes through the origin and is circular, as expected. 53

4.8 Sample resonance results for a 10 μm long uncoated DCB. The amplitude curve is a Lorentzian peak with a fairly narrow linewidth. The phase response is noisier than its cantilever equivalent. These results are typical of the uncoated DCBs. 54

4.9 Resonance frequencies of DCBs versus length. The frequencies are much lower than expected, leading to the conclusion that compressive stress is present in the SOI. The results have been fitted using Equation 2.6, with σ as the fitting variable. The fit resulted in a stress of $\sigma = -32.5 \pm 0.3$ MPa. 56
4.10 Quality factors of uncoated DCBs. The quality factors tend to decrease as the length increases. The data has been fit with Equation 4.6, with σ and E_2 used as fitting variables. The fit results in $\sigma = -35.9 \pm 3.5$ MPa and $E_2 = 16.3 \pm 1.6$ MPa. 57
4.11 Phase shift on resonance for an 10 μm uncoated DCB. This phase data is the same shown in Figure 4.8, plotted in polar coordinates. This result shows a very slightly asymmetric phase change. 60

5.1 Quality factors of uncoated and coated cantilevers. There is approximately a one order-of-magnitude decrease in Q between the uncoated and coated devices. There is no effect of the coating thickness on Q. 63
5.2 Quality factors of uncoated and coated DCBs. The quality factor is approximately one order-of-magnitude lower for the coated devices. There is no effect of the coating thickness on the Q. 63
5.3 Quality factors of uncoated and coated devices with narrowed clamping points. Each device shows approximately a one order-of-magnitude decrease in quality factor after GLAD coating. 65
5.4 Cross sections (top) and top-down (bottom) views of (a) 100 nm thick GLAD posts and (b) 300 nm thick GLAD posts. At the base of the cross sectional views, a thin layer of quasi-continuous film is observed. The 100 nm posts are also closer together than the 300 nm posts with a significant amount of material visible between the larger posts. In (b), the nucleation layer is obscured by the taller, wider posts. These images suggest there may be a quasi-continuous layer at the base of the GLAD film. 66
5.5 Sample resonance frequencies and phase shifts of (a) 100 nm GLAD-coated and (b) 300 nm GLAD-coated cantilevers. Both devices are 3.5 μm long and are representative of the other coated cantilevers. . 68
5.6 Resonance frequencies of 100 nm and 300 nm GLAD-coated cantilevers plotted versus cantilever length. The lines show the upper and lower bounds on the mathematical model derived to predict the resonance frequencies for the 100 nm (solid lines) and 300 nm (dotted lines) GLAD coatings. 69

5.7 300 nm GLAD coated cantilevers of varying lengths showing the GLAD film coverage. The coverage worsens as the beams increase in length. The nominal beam lengths are (a) 4.75 μm, (b) 5.00 μm, (c) 5.50 μm, and (d) 6.00 μm. 71
5.8 The methodology for calculating $\Delta z_{\min}$. This is a simple geometric argument showing that GLAD deposition cannot occur if the cantilever is deflected more than $\Delta z_{\min}$. This is because the side walls shadow the incoming flux. The dotted green line is $\Delta z_{\min}$. This figure shows that $\Delta z_{\min} = \Delta z_{\mathrm{a}} + \Delta z_{\mathrm{b}}$. Since the width of the cantilever is known (400 nm) and the gap width is known (250 nm), $\Delta z_{\min}$ can be easily calculated using simple trigonometry. 72
5.9 A nominally 7 μm long cantilever coated with 100 nm of GLAD film. It is very difficult to determine the point on the beam at which the GLAD ceases to deposit, and so these devices were excluded from the surface stress analysis. 73
5.10 The total deflection is calculated using simple geometry based on this figure. L and L_2 are known from SEM images, and therefore L_1 can be calculated using the formula on the figure. The radius of curvature can then be calculated using $\Delta z_{\min}$ and L_1. R and L_2 are then used to calculate θ_2, which can finally be used to calculate Δz. 73
5.11 The cantilever deflections were plotted versus their length squared in order to find the slope of the linear fit. This slope was then used to calculate the surface stress using Equation 5.5, also shown on this plot. The two points on the right (labeled "stictioned") were excluded from the fit, as their deflections indicated that the beams had become stictioned. This is because their deflections are very close to the depth of the oxide etched out by the BOE. 75
5.12 Sample resonance peaks and phase shifts of 10 μm long DCBs that are coated with (a) 100 nm GLAD film and (b) 300 nm GLAD film. The amplitude responses are typical of the coated DCBs. 77
5.13 Resonance frequencies of the coated DCBs plotted versus the length. The experimental results from the 100 nm and 300 nm GLAD-coated DCBs are shown by the black and blue points, respectively. The red and green lines show fits to the data using Equation 5.6. 78
5.14 Polar phase plots of the coated devices. (a) 100 nm GLAD-coated 3.5 μm long cantilever, (b) 100 nm GLAD-coated 10 μm long DCB, (c) 300 nm GLAD-coated 3.5 μm long cantilever, (d) 300 nm GLAD-coated 10 μm long DCB. 80

List of Tables

3.1 Yields for each category of device fabricated. 29

4.1 Cantilever beam lengths were experimentally determined from SEM images. The corresponding error estimate is included with each measurement. The experimental lengths are compared to the nominal lengths. 46

4.2 Doubly clamped beam lengths were experimentally determined from SEM images. The corresponding error estimate is included with each measurement. The experimental lengths are compared to the nominal lengths. 46

4.3 Summary of important results from the NEMS. These results will be used in Chapter 5 for the analysis of the GLEMS. 61

5.1 Summary of important results from the GLEMS 81

Chapter 1

Introduction

1.1 Motivation

Fifty years ago, "nanotechnology" was something from a science fiction novel. Now, micro- and nanotechnology are commonplace in our everyday world. Computers, which we use for almost everything including writing, communication, mathematics, and entertainment, have ushered in a new era of miniaturization. One category of devices that has been swept up in the trend towards miniaturization is sensors. Sensors are used to connect electronics to the physical world. They take in information from their surrounding environment, often resulting in a physical change to the sensor. This information is transformed into an electronic signal that can be transmitted to a controller.

One subset of sensing technology is gas sensors. These sensors detect the presence, and often the concentration, of specific gases. Gas sensors are also subject to miniaturization. Smaller sensors are cheaper to manufacture, and so more of them can be used. In industrial settings where fast detection of hazardous gases can save lives, the deployment of more gas sensors is an important safety measure. For example, the detection of H_2S is of crucial importance in many oil and gas operations. In addition to the decreased cost, smaller gas sensors are often more sensitive than larger sensors. As the size of the detector decreases, it becomes more comparable to the size of the gas particles. A single particle can, therefore, have a large influence on a small sensor, and cause the sensor to positively identify the presence of the gas. In contrast, larger sensors may require the observation of many particles before the sensor can respond. High sensitivity is desirable so that trace amounts of hazardous gases can be easily detected. By detecting trace amounts of carbon monoxide, sensors in homes could give residents early notice of the hazard.

In addition to industrial or residential applications, highly sensitive and miniaturized gas sensors may also be useful in scientific applications. Some examples

are gas chromatography and mass spectrometry. Inexpensive sensors in these cases would allow the size and cost of these important scientific tools to be decreased, making them more widely available and increasing the ease with which complex gas analysis could be performed. There are many applications where miniaturized and inexpensive gas sensing is highly important.

Miniaturized gas sensors can be made using micro- and nanomechanical devices. These small devices can be fabricated using standard, top-down microfabrication techniques. There are many different types of micro- and nanomechanical sensors but they share in common the ability to detect trace amounts of the gas under analysis. The gas species of interest is called the analyte. These sensors can be label-free or they can be functionalized to act as receptors for specific analytes. Label-free means that the sensors will detect any substances present in the system that interact with the sensor, regardless of their chemical composition. These types of sensors are useful in applications such as mass spectrometry, where the mass of the analyte molecule is the desired output. Functionalized devices, alternatively, have been coated with a layer specifically tuned to detect certain molecules. This is done using a chemical process called surface functionalization. These types of sensors are useful when detection of specific gases is needed, such as in industrial applications or in gas chromatography. This thesis work focuses on the development of nanomechanical sensors for detecting specific gases, and in particular, gravimetric nanomechanical sensors.

The basis of our gravimetric sensors are nanoelectromechanical systems (NEMS). These devices have critical dimensions on the order of hundreds of nanometres and vibrate at a characteristic resonance frequency. In order to detect analyte molecules, the resonance frequency is tracked. When an analyte molecule is adsorbed onto the surface of the device, a shift in the resonance frequency is induced. This shift can be correlated to the analyte mass or concentration. A frequency shift due to added mass on a functionalized resonator is the basic principle behind gravimetric detection.

The resonance frequencies of NEMS are highly dependent on their geometries; the smaller the devices, the higher their resonance frequencies. The resonance frequency is an important factor in the mass sensitivity of NEMS. As the resonance frequency increases, the sensitivity to analyte molecules also increases. This means the smallest devices are also the most sensitive. In label-free systems, the end goal is to maximize sensitivity, which usually means making the devices as small as possible. In gravimetric systems, there are additional complications. In order to functional-

ize the surface of the NEMS, a sensing layer is added. The overall sensitivity of a gravimetric system is then a function of the mass sensitivity of the NEMS, and the sensitivity of the sensing layer to the specific analyte. This overall sensitivity can be described using a figure of merit called the limit of detection (LOD). The LOD describes the smallest concentration of analyte that can be detected by a given sensor and is typically expressed as parts per million or parts per billion. The best sensors have the smallest LOD. The equation describing the LOD is as follows [3]:

$$LOD = \frac{2M_{\text{eff}}\sigma_A}{KSt_f\rho_g} \tag{1.1}$$

where M_{eff} is the effective mass of the sensor, σ_{A} is the Allan deviation, K is the partition coefficient, S is the surface area of the sensing layer, t_{f} is the thickness of the sensing layer, and ρ_{g} is the density of the gas being detected. The effective mass of the resonator is related to the geometry of the NEMS. The Allan deviation is a measure of the noise in the system and will vary based on how the NEMS are detected. The partition coefficient is a property of the sensing layer and depends on the chemistry used for surface functionalization. K and σ_{A} are complex parameters that require significant optimization. The most easily controlled components of this system are related to the geometry of the sensor; that is, the effective mass of the resonator, and the surface area and thickness of the sensing layer.

The simplest parameter to address is the effective mass of the resonator, and so NEMS are usually scaled down as much as possible to decrease their effective mass. Unfortunately, this also decreases the surface area substantially. The sensing layer is a planar layer that is added to the top of the NEMS resonator, and does not contribute any additional surface area to the sensor. The thickness of the sensing layer is also generally much less than the thickness of the NEMS, so the mass of the sensing layer is much smaller than the mass of the NEMS. This prevents the sensing layer from damping the resonator's motion and helps maintain a high resonance frequency.

The idea behind this thesis is that a high surface area, low density sensing layer could reduce the LOD of gravimetric NEMS-based sensors. The effective mass of the NEMS would remain very small, but a substantial contribution to the surface area of the sensing layer would be added, thus reducing the LOD. In this way, a high surface area nanomechanical resonator with low LOD could provide excellent gravimetric sensing performance.

This thesis successfully demonstrates the addition of a high surface area layer to nanomechanical resonators. To our knowledge, this is the first demonstration of

a high surface area layer incorporated onto NEMS. The high surface area material used here is glancing angle deposition (GLAD) thin films. The addition of the high surface area GLAD film to NEMS was not a straightforward process, and so the fabrication of these devices will be discussed in detail. Furthermore, the effects of the high surface area layer on the resonance performance of the NEMS will be explored, both experimentally and using the derived theoretical framework. The goal was to describe the physics behind these devices as fully as possible so the high surface area NEMS could be easily incorporated into gravimetric sensing schemes in the future.

1.2 Outline

The first half of Chapter 2 will discuss the background of nanoelectromechanical systems, including a detailed discussion on how they can be used in gravimetric sensing applications. The second half of Chapter 2 will be devoted to a literature review of glancing angle deposition thin films. Chapter 2 will conclude by bringing these two fields of nanotechnology together and elucidate the reasoning behind the use of GLAD thin films as the high surface area layer.

Chapter 3 will specifically discuss the fabrication of the high surface area NEMS. In particular, it will address the fabrication challenges associated with using GLAD thin films as the high surface area layer. Also included will be a discussion on the various characterization techniques used throughout this thesis.

Chapter 4 will discuss the results from the uncoated devices. The analysis on the resonance frequencies and dissipation of the uncoated NEMS will provide a baseline for the analysis of the coated devices.

The coated devices will be analyzed in detail in Chapter 5. The resonance frequencies will be examined in detail, and a theoretical framework to describe and predict the resonance frequencies of the high surface area devices will be derived. The effect of the high surface area layer on the dissipation will also be discussed. A thorough analysis on the dissipation of the high surface area devices has been performed in order to understand some of the physical mechanisms at work within these devices. A theoretical framework for surface losses will be developed.

Finally, Chapter 6 will present conclusions and suggest directions for future work on this topic, including the integration of these high surface area devices into a gravimetric sensing platform.

Chapter 2

Background

Nanoelectromechanical systems and glancing angle deposition are both extensive fields. To explain how they have been combined in this thesis work, the theory behind each must be explained. First, NEMS will be explored. The essential theory will be discussed, including an overview of NEMS sensing principles. Then, GLAD and the relevant theory will be introduced. The incorporation of GLAD into other devices in the literature will be reviewed. Finally, the rationale for combining GLAD and NEMS will be explained. The chapter will conclude with a discussion of similar high surface area devices in the literature.

2.1 Nanoelectromechanical Systems

Nanoelectromechancial systems have been studied since the 1990s and were a natural extension of the field of microelectromechanical systems (MEMS). Originally, NEMS were defined as nanoscale mechanical systems driven by an electrical force, as the name implies [4]. The definition has since expanded, and the term "NEMS" has come to encompass a much broader range of devices. Currently, NEMS can be driven (or actuated) by mechanical, electrical, magnetic, or optical forces [5, 6, 7]. The devices may have piezoresistive or piezoelectric elements [8, 9] for excitation and readout. Readout, or transduction, is a particularly challenging problem for NEMS. This is because NEMS are very small, and therefore only move by tens of nanometres. Detecting this motion accurately, and above the noise floor of the necessary electronics, is difficult and has therefore been the focus of significant research since the emergence of NEMS. Often, optical interferometry is used to detect NEMS in a method similar to that used in atomic force microscopy (AFM) [10]. This is a sensitive and simple technique, but has the disadvantage that external optics and electronics are required. Piezoresistive transduction, where the NEMS are detected by piezoresistive circuitry deposited on top of the NEMS, has been shown to have great force sensitivity, however, adding these extra components directly onto the chip greatly increases the fabrication complexity [11]. Recently, all-optical trans-

duction has become popular, and has allowed the incorporation of NEMS devices into photonic circuits [7, 12].

In addition to the wide range of actuation and transduction methods available for NEMS, there are also many different geometric configurations for the devices. Some common configurations for NEMS are doubly-clamped beams [13], singly-clamped beams (cantilevers) [14], paddle resonators [15], and disk resonators [16]. Recently, many groups are working with long, thin doubly clamped beams that have string-like behaviour [17, 18]. The doubly- and singly-clamped beams are the simplest devices, and so this work will focus on these types of NEMS.

NEMS are versatile nanostructures due to all of these different driving mechanisms, transduction techniques, and geometric configurations. This versatility is a major advantage of NEMS, and allows them to be used in many applications and integrated into both electrical and optical circuits. Some of the current applications for NEMS devices being explored are contact switches and optical switches for logical operations in computing [19, 20], mass sensors for mass spectrometry [21], and gas sensors for gas chromatography [22]. NEMS-based sensors have also shown potential in biological and chemical sensing applications [23, 24].

Despite their wide range of applications, transduction mechanisms, and configurations, NEMS generally operate in a similar manner and according to the same basic theory. This theory is called Euler-Bernoulli beam theory.

2.1.1 Resonance Frequencies

The common feature between all configurations of NEMS is that they mechanically vibrate at a natural resonance frequency. This is a very important phenomenon as this vibration is what allows NEMS to act as sensors. The natural frequencies of NEMS depends on their geometry and material properties, and can be described very well using Euler-Bernoulli beam theory. Although the theory was originally designed to describe the movement of macroscopic thin, flexible beams, it has since been adapted to the micro- and nanoscale regimes with great success [25]. The basis for much of the mathematical description of nanoscale beams is Equation 2.1, a form of the wave equation:

$$EI\frac{\partial^4 u(x,t)}{\partial x^4} = -\rho A\frac{\partial^2 u(x,t)}{\partial t^2} \tag{2.1}$$

where E is the Young's Modulus, a description of the elasticity of the resonator material. I is the moment of inertia. For a rectangular beam vibrating in the flex-

ural (out of plane) mode, the moment of inertia is $I = wt_{\mathrm{b}}^3/12$. w is the width of the rectangular beam, and t_{b} is the height, or thickness, of the beam. $u(x,t)$ is the function describing the shape of the flexural motion as a function of time. ρ is the density of the material comprising the beam, A is the cross-sectional area of the beam, and t is time.

To allow separation of the time-dependent and time-independent parts of this equation, we can assume a solution of the form $u(x,t) = u(x)\mathrm{e}^{i\omega t}$, where ω is angular frequency. Substituting this into Equation 2.1 gives the following:

$$\frac{\mathrm{d}^4 u(x)}{\mathrm{d}x^4} = \frac{\rho A}{EI}\omega^2 u(x) \tag{2.2}$$

This differential equation has solutions of the form $u(x) = \mathrm{e}^{\kappa x}$, where $\kappa = \pm\beta, \pm i\beta$ and β is the eigenvalue of the solution. Taking the real part gives:

$$u(x) = a\cos(\beta x) + b\sin(\beta x) + c\cosh(\beta x) + d\sinh(\beta x) \tag{2.3}$$

For a more detailed derivation of Equations 2.2 and 2.3, the reader should consult Reference [25], a comprehensive textbook on nanomechanics. The coefficients in Equation 2.3 can be solved for different boundary conditions, such as a doubly-clamped beam or a cantilever.

In addition to giving an expression for $u(x)$, Equation 2.2 can also give an expression for the natural resonance frequencies of the beam for various modes. Analogous to a vibrating string, NEMS can vibrate at a number of natural modes. NEMS typically have resonance frequencies in the mega- to gigahertz range. $u(x)$ is often called the mode shape function, as it describes the shape of the beam when it is vibrating at a given mode.

Although NEMS vibrate at their characteristic resonance frequency without any external forces due to Brownian motion [26], NEMS are often driven using an external force in order to sustain the oscillations and produce larger amplitude vibrations that are more easily detectable. The external force is usually modulated to match the resonant frequency of the NEMS to drive them at their natural resonance frequencies. This means that NEMS generally operate at the frequencies described by Equation 2.2, despite the fact that Equation 2.2 does not include any driving forces. The exception to this are NEMS driven using a parametric amplification technique [27]. These devices are driven at twice their resonance frequency for amplification of the mechanical motion. This type of driving scheme is outside the scope of this thesis.

The next two sections will solve Equation 2.3 for the specific cases of the fundamental modes of doubly clamped beams (DCBs) and cantilevers. Only the fundamental mode will be examined because of experimental limitations that prevent the measurement of higher modes. These experimental limitations will be addressed further in Chapter 3. The following sections will also discuss some of the unique issues that can arise with each type of device.

Doubly Clamped Beams

The earliest NEMS were DCBs because of their relative ease of fabrication and actuation [6]. A schematic of an ideal DCB is shown in Figure 2.1. The length of the beam (L), width (w) and thickness (t_b), as well as the axes that will be used in the remainder of the thesis are all labeled in Figure 2.1.

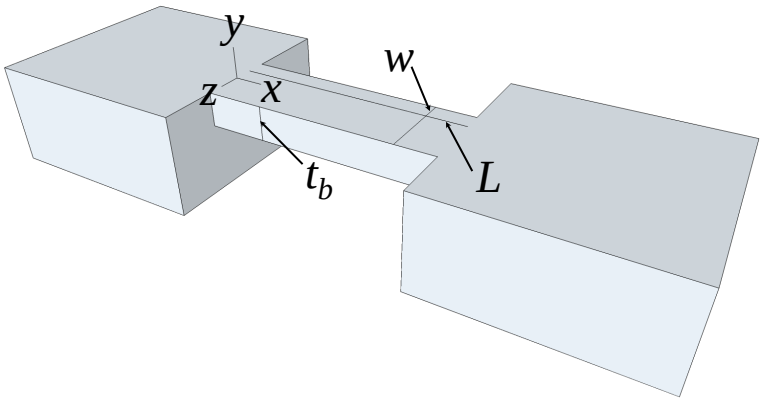

Figure 2.1: Schematic of a doubly clamped beam. L is the length of the beam, w is the width, and t_b is the thickness. The coordinate system is also labeled, with the origin at one end of the beam.

Since the beam is attached firmly at both ends, the boundary conditions that describe this configuration are $u(0) = 0, u(L) = 0, \mathrm{d}u(0)/\mathrm{d}x = 0$, and $\mathrm{d}u(L)/\mathrm{d}x = 0$. Setting both the displacement and slope to zero creates the "clamped" boundary condition. Substituting these boundary conditions into Equation 2.3 gives $a = -c$ and $b = -d$. β can also be solved using a transcendental equation obtained from Equation 2.3, which gives the set of values $\beta_\mathrm{n}L = 0, 4.73, 7.85, 10.996...$ Discarding the trivial zero solution gives $\beta_0 = 4.73/L$ for the fundamental mode. Substituting these results into Equation 2.3 gives the mode shape function for the fundamental mode of a doubly clamped beam:

$$u_0(x) = a_0(\cos(^{\beta_0 x}/_L) - \cosh(^{\beta_0 x}/_L)) + b_0(\sin(^{\beta_0 x}/_L) - \sinh(^{\beta_0 x}/_L)) \tag{2.4}$$

a_0 and b_0 represent the amplitudes of vibration. Although an explicit solution for these values cannot be obtained with boundary conditions alone, the relative amplitude a_0/b_0 can be shown to be -1.01781 [28].

In addition to the mode shape, an expression for the resonance frequency can be derived from Equation 2.2. Substituting in $u(x) = e^{\kappa x}$, $\kappa = \pm\beta_0, \pm i\beta_0$, and solving Equation 2.2 for ω gives the angular resonance frequency for a doubly clamped beam. Dividing this result by 2π and substituting in for β_0 gives the result in the frequency domain for the fundamental mode. This final result is shown in Equation 2.5.

$$f_0^{DCB} = \frac{1.03 t_b}{L^2}\sqrt{\frac{E}{\rho}} \tag{2.5}$$

Equations 2.4 and 2.5 are for the simple case of a doubly clamped beam with no external forces. This is typically not the case, since there is usually some type of stress, which can be compressive or tensile. There are many potential causes of stress. One of the most common types of stress is residual stress, which is a result of stress in the resonator material. For example, DCBs fabricated from silicon-on-insulator (SOI) technology typically exhibit some kind of compressive stress due to the SOI fabrication process [20]. Doubly clamped resonators fabricated from silicon nitride, on the other hand, show high tensile stress [29]. Surface stresses are also a very common source of stress in doubly clamped beams and may occur during fabrication. One example of a surface stress is a stress caused by oxide growth on silicon beams [30]. Stress has a significant impact on the resonance frequency. Compressive stress decreases the resonance frequency, while tensile stress increases the resonance frequency.

It is important to account for residual stress as it can have a large magnitude, and therefore a significant effect on the resonance frequency. To account for stress, a stress term can be added to the right hand side of Equation 2.2. This term usually has the form $-\sigma A \mathrm{d}^2u(x)/\mathrm{d}x^2$, where σ is the total additional stress in the system and A is the cross-sectional area of the beam. After adding this term, the PDE no longer has an analytical solution. There have been several approaches to solving this equation numerically, and therefore different results for the resonance frequency. One often-cited solution is given by Bokaian [31]:

$$f_0^{\sigma} = f_0^{DCB}\sqrt{1 + \frac{\sigma L^2}{3.4 E t_b^2}} \tag{2.6}$$

This numerical solution has been used by many authors [32, 33] but does not differentiate between the different stresses present. A recent work by Postma *et al.* separates the contribution from the residual stress (σ_0) from the bending-induced stress. Bending-induced stress is another type of stress that occurs as the DCBs bend during the course of one oscillation. This result for the resonance frequency is shown in Equation 2.7 [34].

$$f_0^{\sigma_0} = \frac{2\pi}{L^2}\sqrt{\frac{Et_b^2}{36\rho} + \frac{\sigma_0 L^2}{12\pi^2\rho}} \tag{2.7}$$

Both proposed solutions have similar forms; however, Equation 2.7 does not reduce to Equation 2.5 when the residual stress is zero. This is because Equation 2.7 is solved numerically using the Galerkin method, a discretization procedure. This numerical method does not take into account any of the physical characteristics of the system. Given the added complexity of the initial partial differential equation due to the separation of the bending and residual stress terms, the numerical solution becomes quite complicated. Thus, additional numerical coefficients are required to improve the overall solution. Unfortunately, this also means that Equation 2.7 overestimates the resonance frequency when the stress approaches zero. Equation 2.6 is also a numerical solution, but is obtained by numerically solving a transcendental equation that is the solution to the original partial differential equation. Thus, Equation 2.6 is a more physically accurate solution as the stress approaches zero.

Buckling is a phenomenon that can occur when DCBs are under a large compressive stress. Buckled beams have a non-zero displacement when no driving force is applied. In certain applications, buckling can be useful, for example use an non-volatile mechanical memory [20]. In most other applications, buckling is undesirable because buckled beams behave nonlinearly. Buckling is often avoided by using specially designed microstructures [16, 35]. For this thesis, the best approach is simply to avoid buckled structures.

The critical buckling stress σ_c is the stress at which buckling occurs in a DCB, shown mathematically in Equation 2.8 [35]. The critical buckling length L_c of a DCB is the maximum length of beam that will be unbuckled at the critical buckling stress, described by Equation 2.9 [35].

$$\sigma_c = \frac{\pi^2 E}{3}\left(\frac{t_b}{L}\right)^2 \tag{2.8}$$

$$L_c = \pi t_b \sqrt{\frac{E}{3\sigma_c}} \tag{2.9}$$

The buckling length can be used in the design process to avoid DCBs near their buckling limit. The equation for buckling stress can also be used to determine whether DCBs are operating near their buckling point if the magnitude of the compressive stress is known.

Doubly clamped beams have many benefits, as they are well-studied devices that are relatively simple to fabricate. They have drawbacks as well, including the complications from additional stresses, and the potential for buckling.

Cantilevers

Cantilevers have become more popular than DCBs in the literature due to their versatility. They have larger oscillation amplitudes than DCBs, which simplifies detection and transduction. Cantilevers also do not have bulk stress, such as residual stress. Since one end is free, residual stress relaxes when the devices are released. Cantilevers are used at both micro- and nanoscales and can be used in either static or dynamic operating modes. Typically, microscale cantilevers are used in static mode, and the nanoscale cantilevers operate in dynamic mode. In static operation, the static deflection of the cantilever due to a surface stress on one side of the cantilever is detected. This surface stress is caused by the adsorption of analyte molecules on one surface of the cantilever [36, 37]. Alternatively, dynamic mode operation depends on the detection of the cantilever's resonance frequency. Although the static method could potentially benefit from the addition of high surface area thin films [38], we will focus on the dynamic mode of operation to gain a better understanding of the effect of high surface area films on the resonance frequencies of the cantilevers.

Figure 2.2 shows a schematic of a cantilever beam, which has dimensions length (L), width (w), and thickness (t_b). The coordinate system, whose origin is at the base of the cantilever, has x denoting position along the length of the beam.

Similarly to the case of doubly clamped beams, Equation 2.3 can be solved for cantilevers by substituting in the appropriate boundary conditions. These boundary conditions are $u(0) = 0$, $\mathrm{d}u(0)/\mathrm{d}x = 0$, $\mathrm{d}^2u(L)/\mathrm{d}x^2 = 0$, and $\mathrm{d}^3u(L)/\mathrm{d}x^3 = 0$ [25]. The first two boundary conditions specify that the displacement and slope must be zero at the clamping point. The third boundary condition states that there is no force in the y-direction on the free end of the cantilever. The fourth boundary condition states that there is zero torque at the free end. These boundary conditions result in the same form of solution for the mode shape as for the DCBs (Equation 2.4).

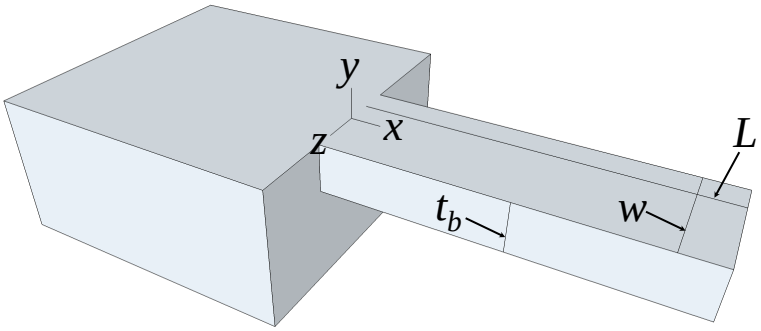

Figure 2.2: Schematic of a singly clamped beam, or cantilever. L is the length of the beam, w is the width, and t_b is the thickness. The coordinate system is also labeled, with the origin at the base of the cantilever.

For the cantilever solution, the eigenvalues are $\beta_\mathrm{n} L = 1.875, 4.694, 7.855...$ resulting in $\beta_0 = 1.875/L$. The relative amplitudes are also different, with $a_0/b_0 = -1.3622$. Finally, by solving Equation 2.2 for the specific values for the cantilever and dividing by 2π, the equation for the resonance frequency of a cantilever can be obtained:

$$f_0^C = \frac{0.162 t_b}{L^2}\sqrt{\frac{E}{\rho}} \tag{2.10}$$

This equation is of the same form as Equation 2.5 with a different coefficient due to the different value of β_0. Comparing Equation 2.5 with Equation 2.10, it can be observed that for a DCB and cantilever with the same dimensions, the cantilever resonance will be much lower due to the smaller coefficient.

DCBs and cantilevers were both used in this thesis to test whether the different boundary conditions would affect the formation of the high surface area layer. The effect of the high surface area layer on the frequency was uncertain, and so having two distinct types of devices to test would be highly valuable.

2.1.2 Phase Shifts

When NEMS resonate, they have an amplitude signal and also a phase signal. The phase of NEMS is similar to that of a simple RLC circuit in that for each resonance peak, there should be a corresponding 180° phase shift. The phase can be a very useful quantity. In particular, a phase-locked loop (PLL) is a feedback circuit able to track the resonance peak [26, 39]. PLL circuitry is very important technology for the commercialization of NEMS, as accurate tracking of the resonance peak is im-

portant in nearly all sensing applications. A degradation in the phase signal means that a PLL would not function properly, and so it is important that any NEMS fabricated have a clear phase shift.

2.1.3 Quality Factor

Energy dissipation in NEMS is measured by the expression $1/Q$, where Q is the quality factor. The quality factor can be described as the overall energy in the system divided by the energy lost per oscillation. Mathematically:

$$Q = \frac{2\pi U}{\Delta U} \tag{2.11}$$

where U is the total energy stored in the resonator and ΔU is the energy dissipated in one period of oscillation. There are many different causes of energy dissipation in NEMS. The following equation highlights how different dissipative mechanisms can combine to give a single Q for a system:

$$\frac{1}{Q_{\text{total}}} = \frac{1}{Q_{\text{surface}}} + \frac{1}{Q_{\text{clamping}}} + \frac{1}{Q_{\text{TED}}} + \frac{1}{Q_{\text{visc}}} + \frac{1}{Q_{\text{other}}} \tag{2.12}$$

$1/Q_{\text{surface}}$ is the dissipation due to surface effects, $1/Q_{\text{clamping}}$ is the clamping loss, $1/Q_{\text{TED}}$ is the thermoelastic dissipation, $1/Q_{\text{visc}}$ is the loss due viscous air damping, and $1/Q_{\text{other}}$ is the contribution from other loss mechanisms, such as defects in the crystal lattice of the resonator material.

One of the most well-understood and easily prevented sources of dissipation is viscous air damping. Viscous air damping occurs when the NEMS operate in the viscous flow regime [8, 40]. In this regime, the surrounding air acts as a fluid around the NEMS to damp their movement. At lower pressures, the molecular flow regime can be reached, and only individual air molecules damp the movement of the NEMS. The molecular flow regime causes far less dissipation than the viscous flow regime, and so it is often desirable to have the NEMS operate under vacuum. The vacuum required for operation in the molecular flow regime varies according to the size of the NEMS [8]. Smaller devices can operate at higher pressures. For example devices less than one micron long can operate relatively successfully at atmospheric pressure. For devices longer than one micron, vacuum operation is necessary to prevent significant damping.

Thermoelastic dissipation is another type of loss that has been well studied in the literature [41, 42, 43, 44]. Thermoelastic dissipation arises from heat generation in the resonator. As NEMS oscillate, they generate high energy thermal phonons

due to repeated straining of the crystal lattice. These phonons are lost into the surrounding environment, causing energy loss. This mechanism is very important for NEMS operating at low temperatures, however, it tends to be less important for NEMS operating at room temperatures. The mathematical description of the thermoelastic dissipation for the fundamental flexural mode of a rectangular beam is [25, 41]:

$$Q_{\mathrm{TED}}^{-1} = \frac{6\Delta_E}{\xi^2}\left(1 - \frac{\sinh\xi + \sin\xi}{\xi(\cosh\xi + \cos\xi)}\right) \tag{2.13}$$

where Δ_{E} is the relaxation strength of the material. ξ is:

$$\xi = \frac{\beta_0^2}{4\sqrt{3}}\frac{w^3}{L^2 l_T} \tag{2.14}$$

where l_{T} is the thermal diffusion length of the material. This equation shows that thermoelastic dissipation increases as the size of the devices decreases.

Clamping loss is also important in NEMS. The clamping losses originate from energy loss into the support structure that anchors the resonator to the substrate. These losses are also referred to as attachment losses, support losses, or anchor losses. Originally, it was thought that the geometry of the anchor point was the sole determining factor in clamping loss [45, 46]. Recently, however, a new theory has been developed by Wilson-Rae that indicates clamping loss is due to phonon tunneling from the resonator into the support structure [47]. This theory has been tested experimentally with good agreement [48]. For a rectangular beam, the Q_{clamping} for the clamping loss of a beam operating in its fundamental flexural mode can be described as [47]:

$$Q_{\mathrm{clamping}} = \frac{3.9}{\pi^4 \delta C_0}\frac{L^5}{w t_b^4}\left(\frac{3\pi}{2k_0 L}\right)^4 \tag{2.15}$$

where:

$$\delta = \begin{cases} 1, & \text{cantilevers} \\ 2, & \text{DCBs} \end{cases} \tag{2.16}$$

$$k_0 \approx \begin{cases} 0.60\pi/L, & \text{cantilevers} \\ 1.51\pi/L, & \text{DCBs} \end{cases} \tag{2.17}$$

$$C_0 = \tanh^{-2}\frac{k_0 L}{2} \tag{2.18}$$

These equations show that the clamping loss is highly dependent on the length and that the loss will increase as the length decreases.

Several works in the literature acknowledge that surface effects can be a major cause of dissipation; however, a comprehensive theoretical description of the surface losses is still unavailable. Surface losses can be caused by several mechanisms including, but not limited to, surface stresses [49], surface adsorption noise [50], surface defects from fabrication processes [18], and thin films on the surface of the resonators [51]. Yasumura *et al.* derive an expression for surface losses in microcantilevers in [43], which can be adapted to account for the addition of thin films such as gold or polymers [52]. This expression uses the complex Young's modulus, also called the loss modulus, to calculate a value for Q. As this value is not an experimentally known material parameter for most materials (including Si), it is difficult to use the expression developed by Yasumura *et al.* as a predictive equation. The Kotthaus group recently developed a similar framework for devices under stress to model the damping in their devices [18]. This method also depends on the complex Young's modulus and cannot be used predictively. Their model is also unable to differentiate between surface and bulk losses. A recent work from the Sader group gives a theoretical description of surface losses of NEMS based on the existence of a localized surface stress at the base of the resonator [49]. This description unfortunately does not match well with experimental data. There are many different mechanisms and theories present for surface losses, and so this is still an area where much research is required to develop a consistent framework.

There are many different sources of dissipation, making the quality factor difficult to explain theoretically. Q is, however, relatively simple to measure experimentally as it can be obtained directly from the resonance peak of the NEMS oscillator. Q can be estimated by using the simple relation that Q is the resonance frequency divided by the full width at $1/\sqrt{2}$ of the maximum when the amplitude is plotted on a linear scale, or the resonance frequency divided by the full width at half of the maximum when the amplitude is plotted on a logarithmic scale. A curve fit of the Lorentzian function:

$$y(f) = y_0 + \gamma \frac{1}{\sqrt{(f^2 - f_0^2)^2 + (f_0^2/Q)^2}} \tag{2.19}$$

allows the extraction of y_0, f_0, γ and Q. f is the frequency, f_0 is the resonance frequency, y_0 is an offset in the amplitude, and γ is a coefficient that represents the maximum amplitude of the peak. Equation 2.19 is a Lorenztian function that can be fit to the NEMS resonance peak to obtain an accurate value for Q. A full derivation of Equation 2.19 can be found in [25] and [10]. Curve fitting using Equation 2.19 was used to obtain values of Q for this thesis.

The Q can be thought of as a measure of the width of the peak, where higher

Q results in a narrower resonance peak. Due to this correlation to peak width, Q is also a measure of the resolution of the system in gas sensing applications. If the Q is very high, the peak will be very narrow and small shifts in the resonance frequency will be easily measured. If the peak is broad, a small shift in the resonance frequency will be difficult to observe. A low Q therefore limits the resolution of the NEMS-based gas sensors.

2.1.4 Nanoelectromechanical Systems as Sensors

NEMS mass sensing is based on the principle of mass loading. When a molecule is adsorbed to the surface of the NEMS devices, the added mass shifts the natural resonance frequency of the NEMS according to the following relationship [26]:

$$\mathcal{R} = -\frac{f_0}{2M_{\text{eff}}} \approx \frac{\Delta f_0}{\Delta M} \tag{2.20}$$

$\mathcal{R}$ is the mass responsivity of the resonator, ΔM is the mass of the adsorbed molecule, and M_{eff} is the effective mass of the resonator. ΔM is also known as the mass sensitivity, and is a measure of the minimum detectable mass. This relationship indicates that so long as the resonance frequency of the NEMS can be tracked accurately, the mass of an adsorbed molecule can be measured through the frequency shift after an adsorption event. This technique is demonstrated in [21], where distinct jumps in the resonance frequency are observed for each adsorption event. This general method has been refined further by the Boisen group, who have been able to account for the position, as well as the mass, of the adsorbed particle on cantilever devices [53, 54].

The usual strategy for improving NEMS-based sensors is to maximize the mass responsivity. From Equation 2.20, it can be seen that increasing the resonance frequency, while decreasing the effective mass, will result in the highest responsivity. Decreasing the size of the resonators will accomplish both goals simultaneously. Since the resonance frequency depends on material properties as well as size (Equations 2.5 and 2.10), different materials such as silicon carbide [55] and carbon nanotubes [56] with high ratio of Young's modulus to density have also been used to increase the resonance frequency. The current state-of-the-art mass sensitivity is 1.7×10^{-24} g, which was achieved using carbon nanotube resonators [57]. For reference, the mass of a proton is 1.67×10^{-24} g [58].

The examples cited above are label-free detectors where superb mass sensitivity is the main requirement. For certain applications, such as gas chromatography, gravimetric sensors are much more desirable because in these applications differentiation between gaseous species is required. Gravimetric NEMS operate on the same

principle of a mass loading-induced resonance frequency shift, and typically have a sensing layer to provide specificity. The sensing layer is usually a thin polymer layer functionalized to act as a receptor for specific substances or a gold layer that acts as the formation site for a self-assembled monolayer (SAM), which also acts as a specific receptor [14, 22]. The addition of the sensing layer complicates the system significantly. First, a method to deposit the sensing layer must be devised. This is not necessarily a straightforward process, especially if the devices are already very small. Polymers can be drop-coated onto the NEMS, however, this is a fairly imprecise technique and can result in variation in the polymer film thickness [8]. The inclusion of a gold layer into the fabrication process greatly increases the complexity of the device fabrication. Secondly, the surface functionalization procedure must be designed to bond to the desired substance only to avoid false positive results. Lastly, the addition of a sensing layer may detract significantly from the quality factor of the resonators. It has been demonstrated that thin layers of only 100 nm of gold on cantilevers of thickness 850 nm can decrease the Q by an order of magnitude, and that as the thickness of the sensing layer increases, the Q continues to decrease [51].

One of the first demonstrations of a NEMS resonator with a functionalized surface was a paddle resonator with a small Au disk positioned at the end of the resonator [59]. The resonator with the Au contact was then exposed to thiolate molecules, which formed a SAM on the Au. The resonators were then used to measure the mass of the SAM using optical interferometry with the devices under vacuum. A mass resolution of 0.39×10^{-18} g was obtained. SAMs were used because they can be designed to have specific tail functional groups, and so the resonators could be tuned for specific analytes. A few years later in 2007, the Roukes group demonstrated atmospheric detection of 1,1-difluoroethane with their polymer-coated silicon carbide cantilevers [8]. These cantilevers utilized a piezoresistive transduction mechanism based on gold piezoresistive elements instead of the traditional highly doped Si elements. Their devices had a mass resolution of $\sim 100 \times 10^{-21}$ g at atmosphere. A completely different strategy was used in a 2008 work based on silicon and rhodium nanowires [60]. The nanowires were fabricated off-chip using the vapour-liquid-solid technique and integrated into arrays via the application of an electric field. These resonators were coated with peptide nucleic acids, which can be used to detect hepatitis C or hepatitis B viruses. A later work by the same group showcased sensing of PCA3 RNA for the detection of circulating tumour cells by using the same type of nanowire resonator array with an estimated detection limit of 1 circulating tumour cell/10 mL of blood by using resonators with less than 10^{-18} g mass sensitivity in moderate vacuum of $\sim$0.1 Torr [61].

There is also much interest in the NEMS community in using NEMS for gas chromatography (GC). This is because the use of NEMS in GC could improve the sensitivity and reduce the cost of the technique. The first work in the literature that used NEMS for GC was a 2010 paper from the Roukes group [22]. In this work, polymer-coated piezoresistive NEMS fabricated from silicon nitride were used as the back-end detector in a commercially available μGC column. This setup had a sensitivity of $\sim$0.6 parts per billion (ppb) with a 10 s equilibration time. This work also demonstrated the differentiation of 13 different chemicals with a 5 s equilibration time. The experiments were done at atmospheric pressure. In 2011, a group from CEA-LETI in France demonstrated the fabrication of a μGC column specially designed to accompany a NEMS-based back end detector [62]. Their setup could differentiate between four different gases in an 80 s window. Finally, the most recent work by the Roukes group uses arrays of millions of NEMS in a GC experiment at atmospheric pressure. Their arrays had densities of up to 6 million NEMS/cm^2 and an equilibration time of 2 s. The piezoresistive devices, fabricated from SOI, were surface functionalized using a polymer layer but were not used to differentiate between different gases.

Clearly, improvements to the sensing layer, both in terms of deposition techniques and surface chemistry, could dramatically improve the performance of gravimetric sensors. Notably, the equilibration time could be improved through better sensing layers as it is generally fairly long for all of the NEMS-GC setups described above. Improvements to gravimetric detectors can also be made by reducing the limit of detection. The LOD, described in Equation 1.1, highlights that there are several parameters of the sensing layer and the resonator that can be optimized to improve gravimetric NEMS performance [3], including the thickness and surface area of the sensing layer. Gravimetric NEMS are a relatively new branch of NEMS sensor technology, and so there is significant potential for optimization of their sensing performance.

2.2 Glancing Angle Deposition

Glancing angle deposition (GLAD) is a thin film deposition technique that was developed in the 1990s. It has been used to fabricate structured thin films for a wide variety of applications including photovoltaics [63], humidity sensors [64] and photonic crystals [65]. GLAD uses physical vapour deposition, typically electron beam evaporation, at highly oblique angles between the substrate normal and the incident flux to produce columnar nanostructures [66]. A simplified diagram of the apparatus used is shown in Figure 2.3. The angle between the substrate normal

and the incident flux is typically labeled α. High α, above 70°, causes shadowing to occur. This shadowing phenomenon prevents material from depositing behind existing structures and therefore results in well-defined, individual nanostructures. Shadowing is described in Figure 2.4. The addition of a substrate rotation, denoted as ϕ, produces a wide range of morphologies, including slanted posts, vertical posts, helices, and zig-zags [65].

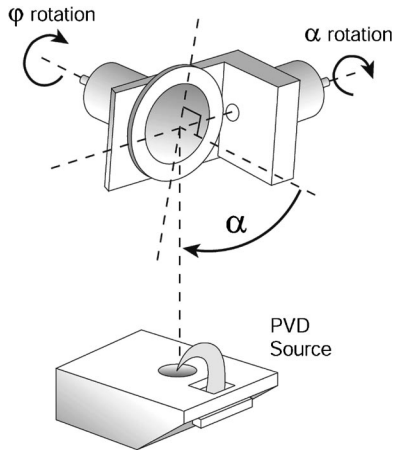

Figure 2.3: A schematic of the GLAD deposition process. The deposition angle is labeled α and the substrate rotation is described by ϕ. Figure reproduced with permission from [1].

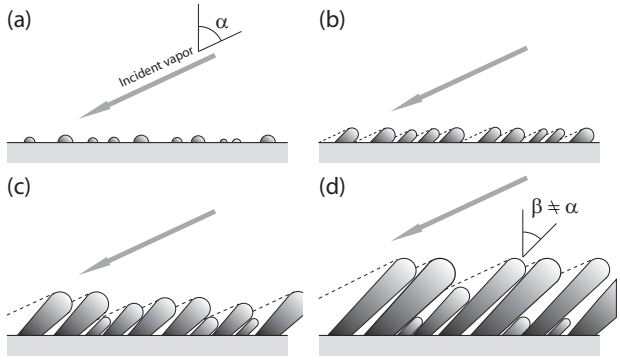

Figure 2.4: A schematic of the shadowing phenomenon. The incident flux cannot deposit in the shadowed region as that area is blocked by the existing structures. Figure reproduced with permission from [2].

Since GLAD films are formed by shadowing, GLAD post growth is a competitive process. That is, as the film continues to grow, some posts will receive more flux than others simply due to the random spacing of the posts on the substrate. The posts that receive less flux will cease to grow, having been edged out by their neighbours. This is called column extinction, and results in a greater number of smaller posts being present at the base of the film, and fewer, larger posts being

present at the top of the film. Column extinction can be prevented by "seeding" the substrate. Carefully designed and spaced seeds provide an initial growth point for the GLAD, thus creating a uniformly distributed film with no column extinction [67]. These seeds are typically fabricated using electron beam lithography, which can significantly complicate the fabrication of the GLAD films. Without seeds, however, the location of the posts is stochastic and many posts will inevitably become extinct.

In addition to column extinction, the competitive growth process of GLAD results in column broadening. Column broadening occurs because as posts become extinct, the remaining posts receive more flux. This causes them to have a much larger diameter at their tops than at their bases. The posts are not, therefore, uniformly cylindrical structures but are instead tapered. Column broadening can be reduced by using a specialized technique called PhiSweep [2], which adds additional substrate motion to counteract the column broadening. Column broadening can also be reduced by seeding, as with greatly reduced column extinction, the posts all receive roughly equal flux and do not broaden as dramatically as unseeded films [67].

The deposition angle α is an important parameter in GLAD films. As α increases, the density of the film decreases because the spacing between the posts increases. To maximize the post spacing and minimize the film density, the highest α possible should be chosen [68]. α also has a strong effect on the surface area of the film. The α that will result in the highest surface area is material dependent. In TiO_2, for example, it is approximately 60°, whereas in SiO_2 it is approximately 65° [68]. The lower deposition angle results in a higher surface area because the columnar structures are deposited more closely together, and so there are effectively more columns on the substrate than films deposited at higher angles. Column broadening is also an important factor in the surface area and tends to reduce the overall surface area of a GLAD film. Larger, broader columns contribute less surface area to the GLAD films than many, thinner columns. The choice of deposition angle is important when optimizing both density and surface area.

The rate of rotation, $\mathrm{d}\phi/\mathrm{d}t$, is an important parameter in determining the morphology of the GLAD films. If the substrate is stationary, that is $\mathrm{d}\phi/\mathrm{d}t \equiv 0$, slanted posts will be produced. If $\mathrm{d}\phi/\mathrm{d}t$ is constant and non-zero, either helices or vertical posts will be produced depending on the rate of rotation. A low and constant $\mathrm{d}\phi/\mathrm{d}t$ will produce helices. The pitch of the helices can be controlled by increasing or decreasing $\mathrm{d}\phi/\mathrm{d}t$. If $\mathrm{d}\phi/\mathrm{d}t$ is constant and high, then vertical posts will be produced. Essentially, at very high rates of rotation, the helices are so tightly coiled that they become vertical posts. More complex structures can be grown by simply

varying $\mathrm{d}\phi/\mathrm{d}t$ in different ways. For example, $\mathrm{d}\phi/\mathrm{d}t$ can also be varied during the deposition to produce a wide range of structures. Zig-zags can be formed by alternating 180° rotations in ϕ with large periods of $\mathrm{d}\phi/\mathrm{d}t = 0$. The ease with which the morphology, density, and surface area can be controlled is one of the major benefits of GLAD films. Another benefit of GLAD films is that many materials can be deposited using the technique, including metals, dielectrics, and organics [69, 70, 68].

2.2.1 Incorporating GLAD into Devices

GLAD films have been incorporated into a number of devices, including many sensing devices. GLAD films can be deposited on countersunk interdigitated electrodes to create capacitive sensing devices. These devices have been demonstrated for humidity and alcohol sensing [71, 72]. The humidity sensors fabricated in this manner have very fast response times of ∼40 ms. The alcohol sensors are selective and can differentiate between methanol, ethanol, and 2-propanol. Another application for GLAD films is in optical filters. These optical filters can be used as circular polarizers [73] or as sensors. Sensors based on GLAD optical filters have been used for humidity sensing [64], and although the response times for these sensors are somewhat slower than their capacitive equivalents, they are still very fast with response times in the range of 270 ms. Recently, GLAD optical filters have been demonstrated for the first time in the optical detection of ultrasound, which could potentially be used in health care applications [74]. A completely different type of GLAD-based sensor was used in [75]. In this work, the GLAD films were incorporated into a surface acoustic wave (SAW) based sensor for humidity sensing. GLAD films have also found application in photovoltaic devices. The columnar morphology of GLAD films makes them desirable for high surface area electrodes in organic solar cells [63]. There are many different applications for GLAD films, and GLAD films can be incorporated into many sensing devices.

Despite the large number of applications for GLAD films, their integration into MEMS has been limited. Many efforts have been made to develop GLAD films for different MEMS applications, such as polymer structures [76]. Furthermore, GLAD films with specially designed friction properties have been developed for use in microgrippers [77]. One example of GLAD integration into MEMS can be found in [78]. This work demonstrates the use of MgF_2 GLAD helices as a humidity sensing layer on large-scale polysilicon piezoresistive cantilevers. Although very preliminary, this work showed some promising initial results indicating that the GLAD films improved the sensitivity of the resonant cantilevers to humidity. There are no SEM images of the completed devices in the paper, however, and so the film uniformity

on the devices cannot be compared to results from this thesis work. There are also no further publications on this topic from Strembicke *et al.* so there is limited information available on these devices. To the best of our knowledge, GLAD films have not yet been integrated into NEMS.

2.3 Combining GLAD and NEMS

As discussed previously, the sensing layer of gravimetric NEMS is an area of the sensor where substantial development is still required. An ideal sensing layer would have a high surface area in order to reduce the LOD, have a low density so as to add as little extra mass as possible to the NEMS, and should not greatly affect the mechanical properties of the resonators. GLAD films have the potential to fulfill all of these requirements, if the deposition parameters are chosen carefully. Krause demonstrated specific surface areas of up to ~675 m^2/g for silicon dioxide GLAD films deposited at $\alpha = 65°$ [68]. However, films deposited at higher deposition angles have the lowest density and the most isolated stuctures. More isolated structures are highly desirable for our application because well-defined columnar structures should theoretically bend with the NEMS vibrating in the flexural mode without adding a significant mechanical contribution to the system. This is schematically shown in Figure 2.5. In order to obtain the most isolated structures possible, a deposition angle of 86° has been used in this work. This is approaching the maximum deposition angle of the deposition system. Silicon dioxide thin films with $\alpha = 86°$ have specific surface areas of 475 m^2/g [68], which is still a significant improvement over the equivalent planar films, which have specific surface areas of less than 50 m^2/g. Additionally, using a high deposition angle of 86° will keep the film density very low to add as little mass as possible to the NEMS. This should keep the resonance frequencies higher in order to maintain the high sensitivity of the NEMS.

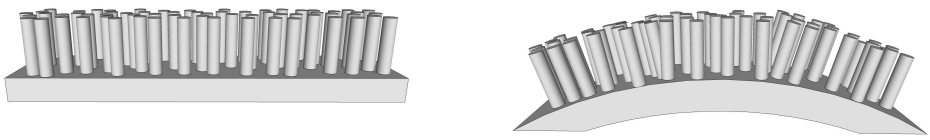

(a) (b)

Figure 2.5: Illustration of columnar structures adding little mechanical contribution to NEMS resonators: (a) a coated device without bending; (b) the same device under flexural motion. Ideally, the pillars will not interact.

We have chosen to deposit silicon dioxide GLAD films, primarily because they can successfully be surface functionalized [79], which is necessary for gravimetric sensing. Silicon dioxide is also compatible with high temperatures required for CMOS processing, which is an added benefit considering that sensing layers comprised of gold or polymer layers are not compatible with high temperatures.

GLAD films may also improve the response time of gravimetric NEMS sensors. As previously mentioned, GLAD films have been demonstrated to be highly effective humidity sensors with very fast response times of less than 200 ms for films thinner than 1 μm [80]. This is a much faster response time than those reported in the literature for polymer sensing layers on NEMS; for example, Bargatin *et al.* saw a 2 s equilibration time in their polymer-coated NEMS [22]. Using GLAD may allow faster equilibration times and improve gravimetric NEMS performance.

For these many reasons, the theory shows that GLAD films are an excellent choice for high surface area sensing layers on NEMS. The remainder of this work will explore the fabrication of these devices and assess their performance. Resonance frequency and quality factor of the GLAD-coated NEMS (henceforth called GLEMS) will be the two main indicators of performance because of their direct correlations to sensitivity and resolution.

2.3.1 Similar High Surface Area Devices in the Literature

A thorough search of the literature revealed that to our knowledge, this is the first experimental work on the fabrication of high surface area micro- or nanomechanical devices. The only similar work is theoretical in nature and comes from Huiling Duan at Peking University in China [38]. In this work, they have proposed a theoretical framework to describe the static and dynamic sensitivities of cantilevers coated with micro- and nanoporous materials. This is done by simultaneously analyzing the surface stress produced by the high surface area layer and the potential for increased adorption mass. Their conclusions were that nanoporous materials provide the largest improvements for both static and dynamic sensitivities. The material they suggested for the high surface area layer is an Au film with pores produced through dealloying. This material is in some sense the reverse of GLAD films, where the pores are etched into a solid film and are therefore connected by very thin strands of material. GLAD posts, alternatively, are deposited directly onto the substrate and for the most part are not connected to each other. The authors present only a theoretical framework, and do not show experimental results, indicating that the work presented in this thesis is an innovative contribution to both the NEMS and GLAD communities.

Chapter 3

Fabrication and Characterization of High Surface Area Nanomechanical Devices

The first goal in this project was to develop a fabrication process for high surface area NEMS. This was not trivial, as these types of devices have never before been fabricated. This chapter will first discuss the development of the fabrication process flow and device designs. Then, the characterization tools used, including scanning electron microscopy and optical interferometry, will be described.

3.1 Fabrication Process Flow

The fabrication process flow was developed iteratively, with all of the fabrication completed at the University of Alberta NanoFab. Several generations of devices were fabricated, with slight variations in the process flow for each generation. This iterative method allowed for full optimization of the fabrication process, and so the final process flow is reliable and repeatable. The process flow outlined here is the final, optimized, process flow. The process flow is shown in Figure 3.1.

The substrates were silicon-on-insulator (SOI) purchased from CMC Microsystems and manufactured by Soitec. The SOI had a 145 nm $\pm$ 10% thick (100) silicon device layer and a 1 μm buried oxide (BOX) layer. These wafers were fabricated using Soitec's SmartCut^{TM} technique, which is capable of producing very thin device layers [81]. SmartCut^{TM} implants hydrogen ions into an oxidized silicon wafer. The hydrogen ions then cause the silicon to break at the implantation depth, leaving a thin layer of silicon on silicon dioxide. The oxide is then bonded to the handle

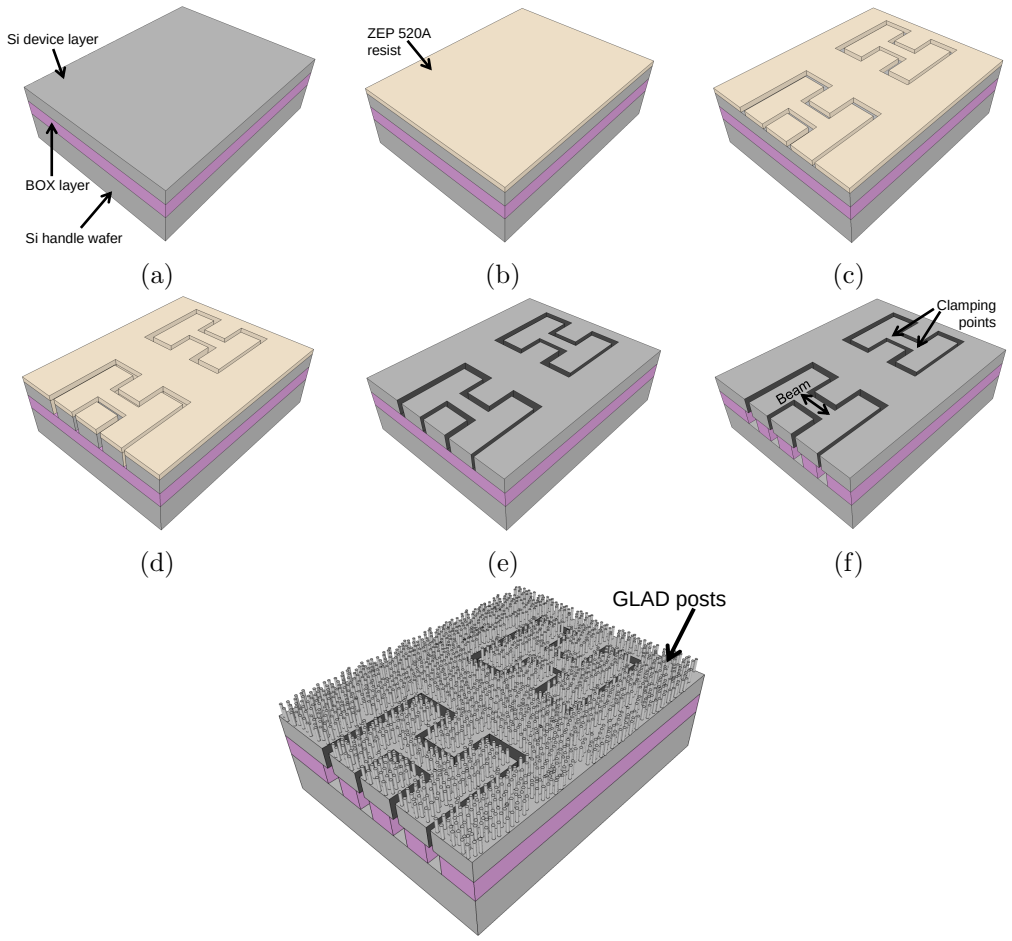

Figure 3.1: A schematic of the process flow used to fabricate the GLEMS. (a) Diced and cleaned and SOI chip. (b) ∼140 nm of ZEP 520A resist spin coated on. (c) Resist patterned with EBL, then developed. (d) ICPRIE used to etch Si. (e) Resist removed with Remover PG and O_2 plasma etch. (f) BOE etch removes BOX and releases devices. (g) GLAD deposited on released NEMS to create GLEMS.

wafer to form a silicon-oxide-silicon wafer. For more detailed information on the fabrication of these wafers, please refer to Reference [81]. The original SOI wafer was 20 cm in diameter, and was cleaved into quarters. One quarter of the wafer was then diced into 1 cm by 1 cm chips using the Disco DAD 321 dicing saw. The small pieces were then cleaned in a Piranha bath (3:1 sulfuric acid to hydrogen peroxide) for 15 min. Once the substrates were prepared, they were spin-coated with a 1:1 mixture of ZEP 520A positive resist and anisole solvent, shown in Figure 3.1b. The addition of the anisole reduces the thickness of the spun-on resist layer, giving a resist thickness of ∼140 nm. The resist was spun on using a Brewer spinner with a 500 rpm spread cycle for 5 s and a 5000 rpm spin cycle for 40 s. The substrates were then baked on a Brewer hotplate for 10 minutes at 170 °C to drive off excess solvent.

The next step was to use the Raith 150-TWO electron beam lithography (EBL) system to pattern the devices, shown in Figure 3.1c. EBL is capable of writing very small features, such as those desired for NEMS. During the lithography step, a 10 μm aperture and 10 kV accelerating voltage were used. Since ZEP 520A is a positive resist, the chemical bonds were weakened in the exposed areas. On each 1 cm^2 chip, four identical patterns were written in each corner. This expedited the process development as four identical samples were produced with each EBL write. After the writing procedure, the chips were developed in ZED N50 developer for 40 s. The chips were then transferred to a 1:3 mixture of methyl isobutyl ketone (MIBK) to isopropyl alcohol (IPA) for 30 s to stop the development. Finally the chips were rinsed in IPA for 30 s and another 30 s in deionized (DI) H_2O. The development process removes the resist with weakened bonds, and so all of the exposed resist is removed.

The next step was to etch the silicon device layer, illustrated in Figure 3.1d. This was done using the STS inductively-coupled plasma reactive ion etch (ICPRIE). This is a dry etch that tends to etch anisotropically because the substrate is biased to draw the etchant ions directly perpendicular to the substrate. This results in vertical sidewalls, which are desirable for creating the most uniform and rectangular beams possible. In this case, SF_6 gas was used as the etchant due to its high selectivity of silicon over silicon dioxide. The etch was carried out for 30 s.

After the ICPRIE step, the resist had to be removed, as shown in Figure 3.1e. This was done by soaking the chip in Remover PG for 10 min, and then soaking the chip in IPA for 5 min to remove any Remover PG residues. As surface cleanliness proved to be of critical importance, any further residues were removed using an oxygen plasma etch for 4 min in the μEtch system.

The next step was to release the silicon devices from the BOX layer underneath (Figure 3.1f). A wet buffered oxide etch (BOE) was used. BOE is a 10:1 mixture of ammonium fluoride to hydrofluoric acid. This released the devices; however, without proper drying, the devices would fail due to static friction, or stiction. Stiction occurs in micro- and nanoscale mechanical devices when water is left in the space between the device and the substrate. The capillary forces caused by the water are quite strong, and as a result when the water evaporates slowly, the devices bend toward the substrate. When the water evaporates completely, the device is left adhered to the substrate, usually permanently. Stiction is a very common failure mode in MEMS/NEMS. In order to avoid stiction, critical point drying was used.

Immediately after the BOE etch, the samples were rinsed in DI H_2O and then transferred to IPA as quickly as possible to minimize exposure to air. The chip was then placed in IPA in the Tousimis critical point drier. Critical point drying floods the sample with liquid CO_2 to replace the IPA. Then, the pressure and temperature are increased to reach the critical point of CO_2, above which CO_2 is a supercritical fluid. This means that the CO_2 transitions from liquid to vapour phase without crossing a phase boundary, and so the likelihood of stiction is greatly reduced as no evaporation occurs. After the critical point drying is done, the NEMS devices are complete. An SEM image of a completed NEMS cantilever is shown in Figure 3.2. The next step is to add the GLAD film to the surface of the NEMS.

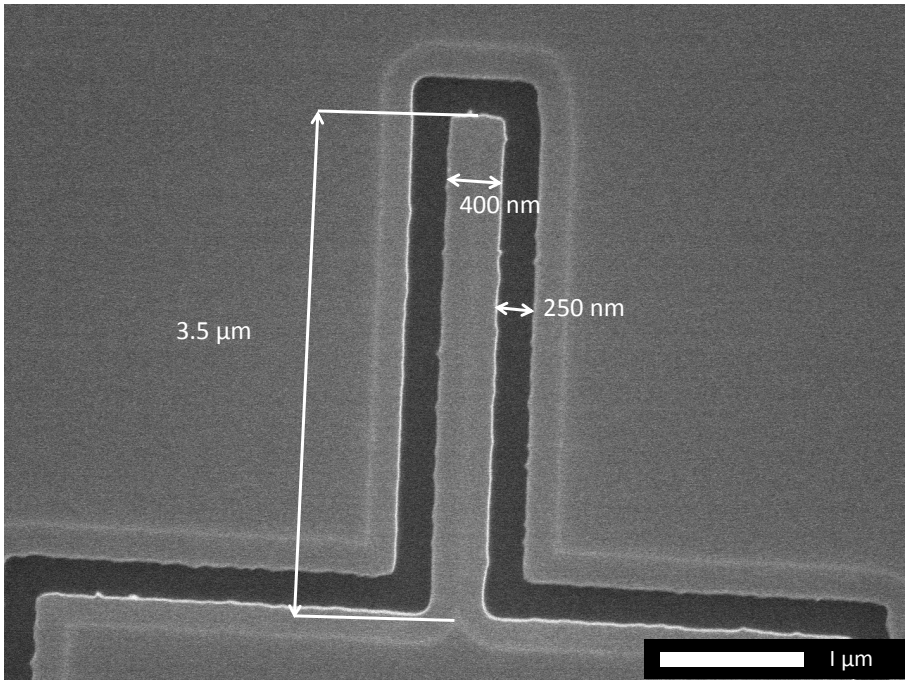

Figure 3.2: Top-down SEM image of a NEMS cantilever, 400 nm wide, 3.5 μm long, 145 nm thick.

Since each 1 cm^2 chip had four sets of devices, the chip was cleaved into smaller pieces to give four separate samples. Cleaving was done simply with a diamond scribe. One of the four pieces was left untouched to act as a control sample. Two of the samples were coated with GLAD films, illustrated in Figure 3.1g. The fourth was left as a spare in case an error occurred during the deposition. The samples were prepared for GLAD coating by first being attached first to a glass slide with double sided kapton tape. The glass slide was then taped using kapton tape to the deposition chuck, adjacent to one quarter of a silicon wafer. For each deposition, a quarter

wafer of (100) Si was also coated to serve as a witness sample. This provided a large sample of GLAD films so that the thickness and morphology of the posts could be easily analyzed. The chuck was then placed into the deposition system. The GLAD films were grown using AXXIS systems (Kurt J. Lesker). The base pressure was $\sim 2\times10^{-7}$ Torr, and deposition pressures were $\sim 2\times10^{-6}$ Torr. The material used was SiO_2 (Cerac, 99.99% pure, 1–3 mm pieces). The deposition angle was 86° and the pitch of the films was 5 nm. The pitch is the amount of material deposited in one 360° rotation in ϕ. A 5 nm pitch is relatively small, which means the substrate rotation will be quite fast, resulting in the growth of vertical posts as opposed to helices. Two different film thicknesses were grown: 100 nm and 300 nm. After the film deposition, the GLEMS were complete. A scanning electron microscope (SEM) image of the finished devices are shown in Figure 3.3.

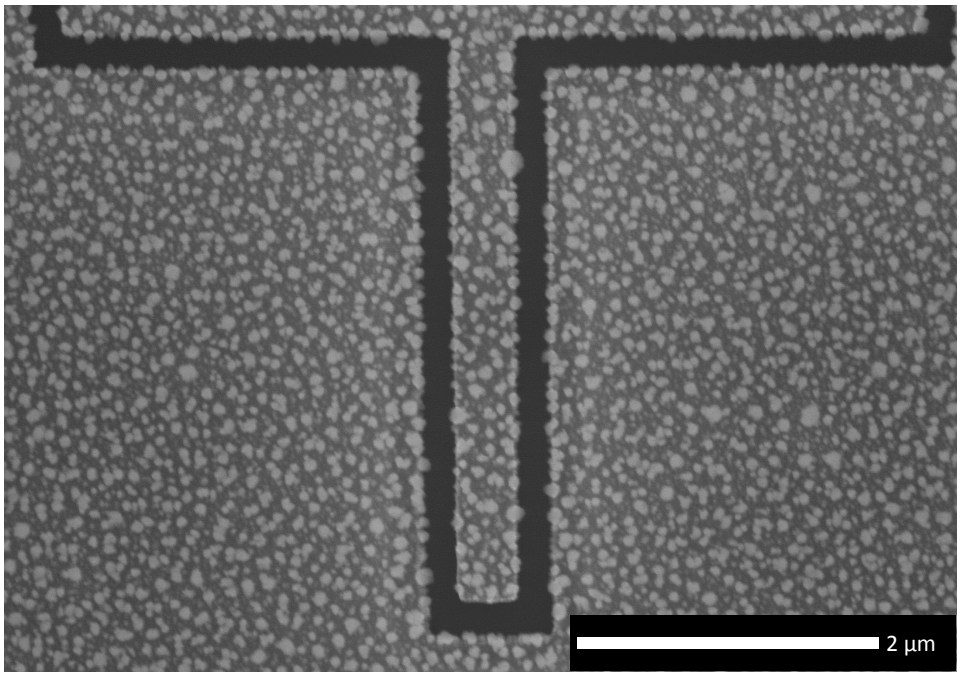

Figure 3.3: Top-down SEM image of a GLEMS cantilever, 400 nm wide and 3.75 μm long.

The yields of each type of device are listing in Table 3.1. The uncoated DCBs, 300 nm GLAD-coated DCBs, and 100 nm GLAD-coated cantilevers have the highest yields. This indicates that the thickness of the GLAD film does not affect the yield for the DCBs. The failed DCBs on the 100 nm GLAD-coated sample were mid-length, and near each other on the chip, which indicates that a piece of debris may be the cause of device failure. The cantilever devices, alternatively, seem to have a

reduced yield when the thicker GLAD films are deposited. This is most likely due to the surface stress introduced by the deposition process, and will be dicussed further in Chapter 5. The failed cantilever devices are always the longer devices, indicating that stiction is the most likely failure mechanism.

Table 3.1: Yields for each category of device fabricated.

Device Type	Yield (%)
Uncoated Cantilevers	86
Uncoated DCBs	100
100 nm GLAD-coated cantilevers	100
100 nm GLAD-coated DCBs	92
300 nm GLAD-coated cantilevers	70
300 nm GLAD-coated DCBs	100

The following section highlights the rationales behind different aspects of the fabrication process.

3.2 Fabrication Challenges

3.2.1 Clumping

It may seem strange that the GLAD film deposition is the final step to occur in the GLEMS fabrication sequence. In a typical process flow, the majority of the layers are deposited first, and then alternating patterning and etching creates the desired device. The reason the typical process sequence cannot be used for GLAD films is because the as-deposited GLAD films are incompatible with wet processing. When exposed to liquids such as water, resist, or developer solution, the individual posts comprising the GLAD films clump together due to capillary forces between the posts. This mechanism is nearly identical to stiction and is described more fully by the group of Zhao *et al.* in References [82] and [83]. Clumping is also known as clustering or the nanocarpet effect.

Clumping is highly undesirable. It drastically reduces the surface area of the GLAD films and effectively destroys the well-defined columnar morphology. Some work has been done to alter the GLAD films post-deposition in order to stiffen them and prevent clumping. Ion milling has been shown to improve the GLAD film's resistance to clumping after exposure to water [84]. For NEMS fabrication, repeated exposure to liquids is required. Ion milling does not make the posts sufficiently robust to endure this process. Ion milling also reduces the surface roughness of the posts, and therefore also reduces the surface area of the GLAD films. A reduction in surface area is highly undesirable for this thesis work. Clumping is one of the

primary reasons that GLAD films have experienced difficulty being integrated into devices. Without the ability to directly pattern the GLAD films, it is challenging to use GLAD films in micro- and nanoscale devices. To avoid clumping, the GLAD deposition had to be the last step in the GLEMS fabrication process.

3.2.2 Edge Effects

Placing the GLAD deposition at the end of the process flow introduced another issue. This issue, called edge effects, occurs when GLAD films are deposited on substrates with uneven topography. The uneven topography, combined with the highly oblique angle of the incident flux, results in solid films growing on the edges of the topography, and porous films growing near the centre of the feature [85]. If a device, such as a NEMS resonator, is present on the substrate, the incident flux will observe a nearly zero incident angle along the sides of the device. This results in the deposition of a solid thin film on the sides of the beam. On the top surface of the beam, the incident flux sees the expected oblique angle and widely spaced GLAD posts are deposited. When these two extremes meet at the corner of the NEMS beam, the result is an extremely non-uniform film composed of large, poorly-defined columns. Edge effects reduce the surface area dramatically and the solid layer along the edge of the beams is detrimental to their mechanical performance.

To eliminate this issue, the NEMS were inset into the silicon. Instead of removing a large amount of the silicon device layer to expose the resonators, which is the approach typically used in MEMS/NEMS fabrication, only the outline of the resonators was removed. A narrow outline was written using EBL. The narrower the line, or gap, the fewer the edge effects. This is because the flux is incident at such an oblique angle that it will not "see" small gaps in the silicon. Figure 3.4 shows a schematic of what the incident flux would see at a very low α (Figure 3.4a) and at a very high α (Figure 3.4b). At high α, the incident flux sees only a continuous substrate if the gap is sufficiently small. In order to eliminate the edge effects, very narrow gaps had to be written. Writing very narrow gaps and removing very little silicon also dramatically reduced the EBL write-time, which allowed fast prototyping and more efficient processing.

The width of the gap had to be optimized. Very narrow gaps were difficult to fabricate, reducing the yield and repeatability of the process. Narrow gaps also made the devices more difficult to find on the chip, increasing the difficulty of characterization. On the other hand, wide gaps caused edge effects to occur. To optimize the gap width, a test chip was written. This chip contained lines with varying widths from 50 nm wide to 500 nm wide in increments of 50 nm. $\sim$300 nm of SiO_2 GLAD

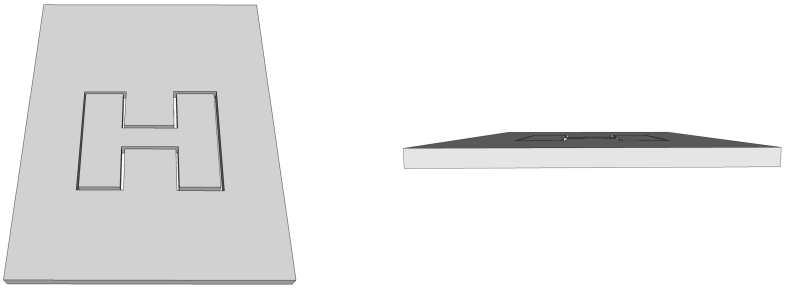

(a) (b)

Figure 3.4: Illustration of the design to eliminate edge effects. (a) shows the view of the devices from a low incident angle, and (b) shows the view at a high incident angle, close to 90°. Note that the device outline essentially vanishes at a high incident angle, meaning that the incident flux sees a nearly planar substrate.

vertical posts were grown at $\alpha = 86°$ on the test chip. The lines were then imaged to determine the widest gap without edge effects. The 50 nm gaps were very difficult to locate with the SEM, suggesting that that devices with gaps this narrow would be difficult to characterize. The gaps with widths greater than 300 nm all showed obvious edge effects. An SEM image comparing the 300 nm width to the 250 nm width is shown in Figure 3.5, with the 300 nm gap on the left and the 250 nm gap on the right. From this image, it was determined that a gap width of 250 nm eliminated edge effects and was also straightforward to fabricate. Therefore, a 250 nm wide gap was used throughout the remainder of the study.

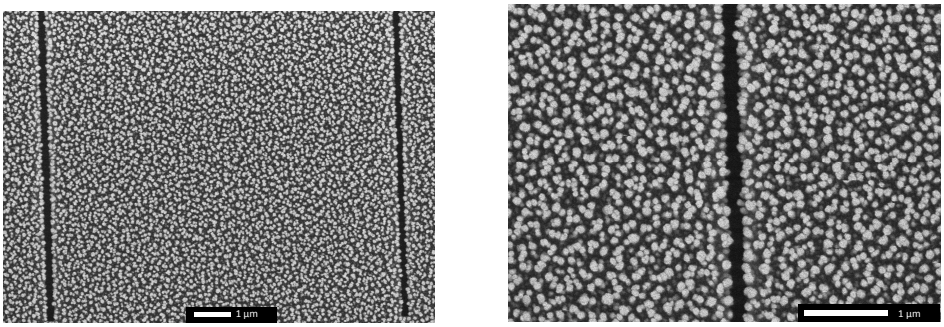

(a) (b)

Figure 3.5: The test structure used to determine the optimal gap width, coated with ~300 nm of GLAD SiO_2 vertical posts. (a) shows both the 300 nm and 250 nm widths. The line on the left has a gap of 300 nm, and edge effects are visible on the outline of the structure. The line on the right has a gap width of 250 nm. Edge effects are not noticeable here. (b) is a zoomed-in image of the 250 nm width only, and shows minimal edge effects at high magnification.

3.2.3 Surface Residues

Another issue that proved quite troublesome during the development of the fabrication process was surface residues. Since all of the NEMS fabrication had to be completed before the GLAD deposition, there were many opportunities for the chips to become contaminated with debris or residues. Since the GLAD films tend to deposit preferentially on raised surfaces, and because topography creates edge effects, the GLAD film uniformity was destroyed when deposited on surface residues. The residues were not always found on devices, but when they were, the defects produced were device-disabling. Figure 3.6 shows an SEM image of a device destroyed by surface residues. The GLAD film in this case was deposited in a strange pattern on top of the residues and bridged the gap between the resonator and the rest of the substrate.

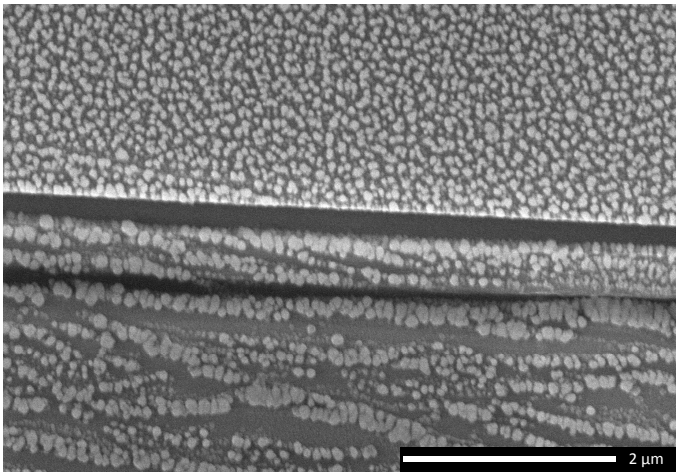

Figure 3.6: A DCB destroyed by the presence of surface residues. Note the non-uniform GLAD deposition that causes the GLAD to grow in the gap between the beam and the substrate. No oxygen plasma etches were used in the fabrication of this beam, and a pentane release method was used instead of critical point drying.

It was initially thought that performing an oxygen plasma etch after all of the processing steps and prior to the GLAD deposition would clean the chip sufficiently to eliminate the surface residues. The process cleaned the substrates effectively, but unfortunately it also induced buckling in the doubly clamped beams. The buckling was extremely obvious in the GLAD-coated devices, as buckled-up beams produced shadowed areas, and buckled-down beams did not have any GLAD posts deposited on them. SEM images of the buckled devices are shown in Figure 3.7.

Oxygen adsorption onto silicon can cause surface stresses [86]; these surface

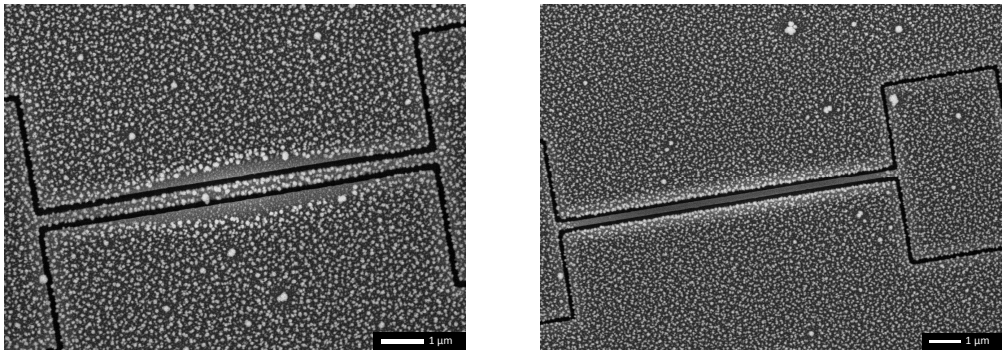

(a) (b)

Figure 3.7: SEM images of buckled DCBs. (a) shows a beam that is buckled up, and (b) shows a beam that is buckled down. In both cases the shadowing of the GLAD films provides a stong indicator of the device failure. These DCBs were fabricated near each other on the same chip.

stresses have been shown to affect both the resonance frequency and quality factor of cantilevers [30]. It is conceivable that while undergoing the oxygen plasma etch, a relatively thick oxide layer could have formed on the NEMS, inducing stress and causing buckling. However, both [86] and [30] state that oxygen adsorption onto a (100) Si surface causes tensile stress, whereas buckling is caused by compressive stress. A different mechanism than oxygen adsorption may be the cause; perhaps damage to the silicon surface caused by the etch. Also of note is that there was no consistent trend to predict which devices would be buckled up and which would be buckled down. Often, a buckled-up beam was adjacent to a buckled-down beam on the same chip. A further study specifically on this phenomenon would be required to understand the mechanism causing the buckling.

Thermal treatments such as annealing have been shown to reduce both compressive and tensile stress in silicon [87, 88, 89, 44]. The temperature and duration of treatment required to fully relax the silicon varies in the literature; however, most of the temperatures are 1000 °C or greater. The times vary widely, with anywhere from 30 min to 120 min reported. Annealing was attempted to relax the stress in the buckled beams. Two buckled samples were annealed in argon. The first was done for 30 min at 1000 °C. The second was done for 60 min at 1100 °C. Optical microscope images of the annealed beams showed the surface debris worsened after the thermal process. There was also no obvious relaxation of the buckling. It was decided to simply avoid the use of an oxygen plasma etch after the NEMS completion and before the GLAD deposition. As mentioned in Chapter 2, buckled beams behave nonlinearly, and so buckling had to be prevented to keep the devices

operating in the linear regime.

Since an oxygen plasma etch at the end of the fabrication process could not be used, the next course of action was to go through the fabrication process step-by-step to determine the source of the debris. This was done by inspecting the devices with optical microscopy after each step in the fabrication process and carefully recording where residues were introduced. The two steps that introduced the most debris onto the chip were the resist removal step and the critical point drying step. The resist removal step left many large, thin, organic residues on the chip. The critical point dry step left large, isolated pieces of debris. The residues from the resist removal were the most important residues to focus on eliminating as they were the residues causing the problems shown in Figure 3.6, and affected many devices at once. The debris from the critical point dry, alternatively, was very isolated and only affected one or two devices on each chip.

One attempt was made to eliminate the residues from the critical point drier. A pentane release technique was used on one generation of devices. A pentane release takes advantage of the fact that pentane evaporates very quickly in ambient conditions. Immediately after the BOE release and subsequent DI H_2O rinse, the chip is placed quickly in a small amount of IPA. Pentane is then added in small increments to the IPA until the mixture is mainly pentane. The chip is then transferred quickly to pure pentane, and then removed from the pentane and dried with dry nitrogen. This step successfully eliminated all of the large pieces of debris from the process. Unfortunately, it also added organic residues to the chip. Since the organic residues destroyed more devices than the critical point drier debris, only the critical point dry step was used for the remaining generations of devices.

Initially, the resist was removed using only Remover PG, a wet chemical. During the course of the residue-isolating experiments, it was determined that either leftover resist or possibly a residue from the Remover PG was the source of the residues on the NEMS. The addition of an IPA rinse after the Remover PG seemed to improve the device yield, albeit inconsistently. To improve the consistency of the residue removal, an oxygen plasma etch was introduced immediately after the resist removal with Remover PG/IPA. The idea was that since the devices were not released, any SiO_2 grown on the surface of the silicon would be removed during the subsequent BOE release step and the devices would remain unaffected by the oxygen plasma etch. This proved to work well, and resulted in clean and unbuckled devices.

3.3 Device Design

The devices were designed using the Raith 150-TWO software, a 2D CAD program intended to accompany the EBL writing system. Figure 3.8 shows the design output by the software. Designing the DCBs and cantilevers was relatively straightforward; the only design rules that were used were that the anchor pad should be much larger than the width of the beam, and that each resonator should be isolated from the rest of the device layer to prevent coupling of device resonances. The anchor pads were 6.5 μm wide and 4 μm long, substantially wider than the 400 nm wide beams. The gaps were designed to be 250 nm wide, as described in the Section 3.2.2 above.

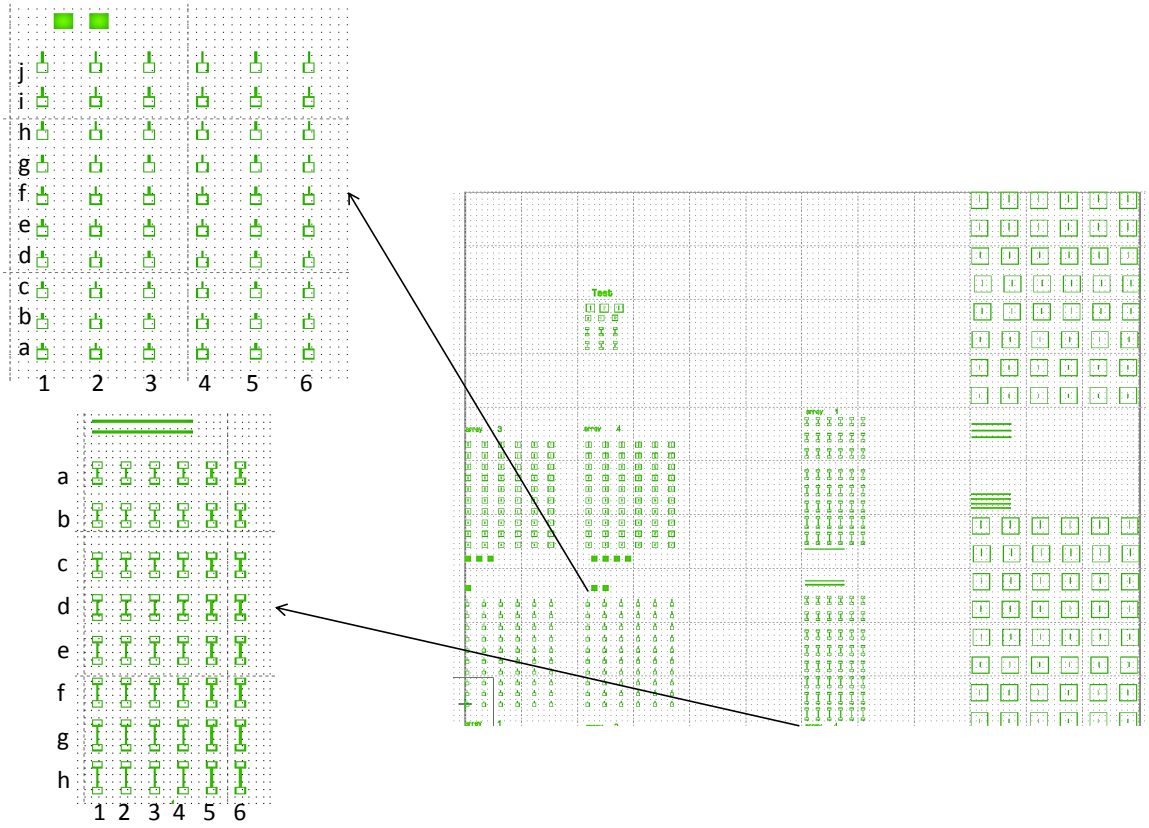

Figure 3.8: Schematic of the devices written using the Raith 150-TWO software. The rightmost image shows all of the devices written in each session. The modified devices are visible in the array labelled "Test" in this schematic. The array on the top left is the cantilever array. All devices of the same length are labelled alphabetically, and each column is labelled numerically, giving a unique designation for each device. The DCBs measured are shown at the bottom left of the figure, with an identical naming scheme.

The lengths of the beams were designed according to Equations 2.5 and 2.10

in order to ensure that the resonance frequencies of the devices would be easily detected by the optical interferometry system. This resulted in lengths of 3.5 μm, 3.75 μm, 4 μm, 4.25 μm, 4.5 μm, 4.75 μm, 5 μm, 5.5 μm, 6 μm, and 7 μm for the cantilevers. These devices had nominal resonance frequencies ranging from $\sim$15 MHz to $\sim$4 MHz, well within the limits of the optical detection system. The doubly clamped beams ranged in length from 7 μm to 14 μm in increments of 1 μm. This led to a range of resonance frequencies between $\sim$25 MHz to $\sim$6 MHz according to Equation 2.5. The highest frequencies would be difficult to detect with the optical interferometry system. However, there was an uncertain amount of compressive stress present in the SOI, as the effects of compressive stress had been observed in previous experiments. It was estimated the resonance frequencies of the doubly clamped beams would be detectable by the interferometry system as the compressive stress would lower the resonance frequencies.

The beam widths were chosen somewhat arbitrarily, since the width has no effect on the resonance frequency. The beam width was 400 nm. Typically, the width of NEMS is narrower. In this case, however, additional width acted to increase the surface area of each resonator, and so it was decided to keep the width larger in order to increase the number of GLAD posts on each beam. In the final design, shown in Figure 3.8, each device was repeated six times on the chip to ensure that several working devices would be present. This meant that there was an array of 6×10 cantilevers and an array of 6×7 DCBs. The length varied in each row (labeled alphabetically in Figure 3.8). Each column was labeled numerically and contained duplicate devices. For example, for the cantilevers, column 1 was identical to column 4. Row "a" contained the shortest devices and row "j" contained the longest devices.

In addition to the standard DCBs and cantilevers, modified NEMS were fabricated to test the effect of the GLAD on the clamping point of the resonators. These modified devices were done with both singly and doubly clamped configurations and featured narrow clamping points of 100 nm. The devices then widened out to 400 nm in the centre. SEM images of a modified doubly clamped beam and a modified cantilever are shown in Figure 3.9. The length of the modified DCBs were 7 μm and 8 μm long. The length of the modified cantilevers was 4 μm long. Three of each device were fabricated on the chip for a total of nine modified devices.

One other design was fabricated, shown in Figure 3.9b and Figure 3.9c. This design featured a device with no specific support structure. Rather, the devices were supported by a large area of the substrate. To prevent the coupling of device resonances, the devices were all surrounded by large squares. These devices were

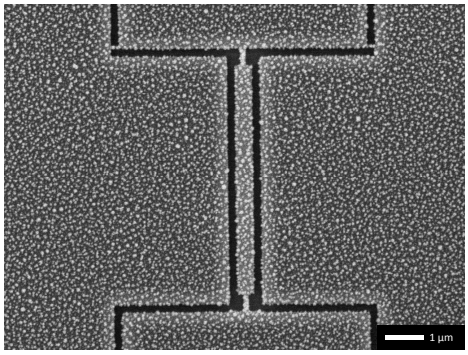

(a)

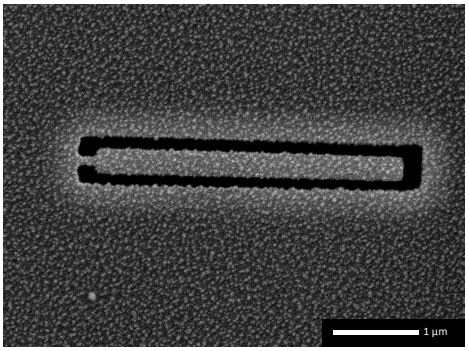

(b)

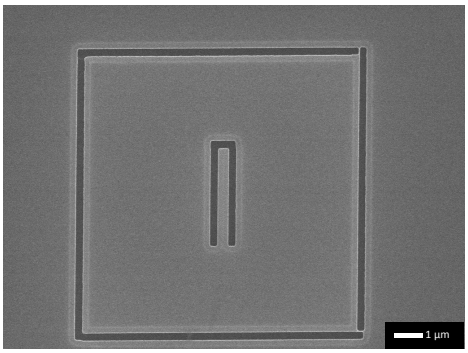

(c)

Figure 3.9: SEM images of devices with narrowed clamping points. (a) shows a doubly clamped beam with 100 nm wide clamping points coated with 300 nm of GLAD vertical posts deposited at 86°. (b) is a cantilever with a 100 nm wide clamping point coated with 100 nm of GLAD vertical posts deposited at 86°. (c) A zoomed-out view of an uncoated NEMS device with no support pad. Notice the square etched around the outside, designed to limit any coupling of vibrations between devices.

also tested, but showed no obvious differences in frequency, phase, or quality factor to the more traditional devices shown in Figure 3.3. In fact, these devices proved somewhat more difficult to measure in the optical interferometry system because the alignment was much more difficult without the support structure to use as a visual reference. For this reason, the traditional devices were used for all of the measurements and analysis in Chapters 4 and 5.

3.4 Characterization Techniques

Two main characterization techniques were used to determine the success of the devices. The first was scanning electron microscopy, which provided visual feedback

on the fabrication process. The second was optical interferometry, which detected and recorded the resonance peaks and phase signals of the devices. These two techniques will be described in more detail in the following subsections.

Other characterization techniques used were optical microscopy and variable angle spectroscopic ellipsometry (VASE). Optical microscopy was used throughout the fabrication process design to detect the presence of surface residues and to confirm the success of various steps, such as development and resist removal. Optical microscopy proved invaluable in isolating the residue-producing steps and mitigating the effects of the surface residues.

VASE was used to determine the reflectance of the GLAD film to confirm that optical interferometry was a viable detection technique. Ideally, the GLAD film should not scatter the laser light required for the sensitive optical interferometry measurements so the signal-to-noise ratio is maximized. VASE was used to test the scattering effect of the GLAD film by comparing the reflectance of a SOI substrate coated with ∼300 nm of SiO_2 GLAD vertical posts to an uncoated SOI sample. The reflectance measurements were done over a wavelength range of 500 nm to 1000 nm at incident angles of 20° to 70°. Figure 3.10 shows the results for an incident angle of 20° over the entire wavelength range for the uncoated and GLAD-coated SOI.

The optical interferometry setup operates at a wavelength of 633 nm and an incident angle of zero. Unfortunately, the ellipsometer does not have the ability to measure the reflectance at incident angles less than 20°, and so the conditions of the optical interferometry setup could not be mimicked exactly. By comparing the reflectance at the lowest angle of incidence (20°) at the desired wavelength of 633 nm, an estimate of the scattering can be obtained. Figure 3.10 demonstrates that the GLAD film should have a negligible scattering effect on the optical interferometry results.

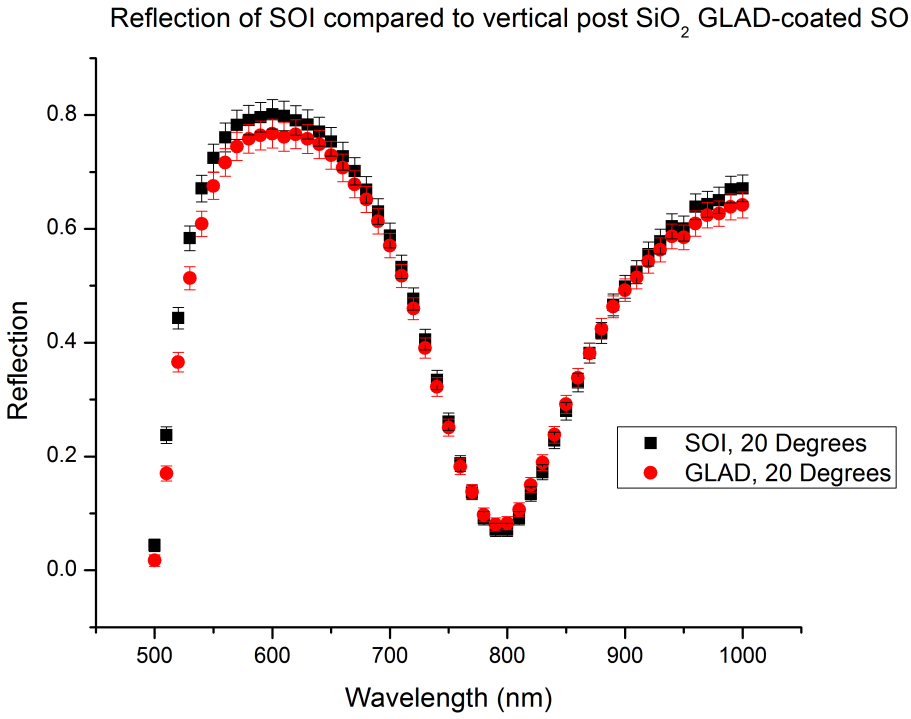

Figure 3.10: Measurements of the reflectance of an uncoated SOI sample compared to the reflectance of a SOI substrate coated with ∼300 nm of GLAD SiO_2 vertical posts deposited at 86° over a range of wavelengths at a 20° angle of incidence. At a wavelength of 633 nm, the reflectances of the two samples are within error, indicating that scattering is negligible in the optical interferometry measurements.

3.4.1 Scanning Electron Microscopy

Scanning electron microscopy (SEM) was used to image the devices. This technique uses secondary electrons generated from the sample to map the topography. Two different SEM instruments were used during the course of this research; a field-emission JEOL 6301F (Department of Earth and Atmospheric Sciences), and a field-emission Hitachi S-4800 (National Institute for Nanotechnology). The majority of the initial imaging was done using the JEOL 6301F. When higher resolutions were required for close examination of the devices, the devices were imaged using the Hitachi S-4800. The accelerating voltages used ranged from 15 kV to 20 kV.

All of the samples containing released devices were imaged without a metallic coating. Often, metallic coatings such as gold or chrome are used to increase the conductivity of a sample and prevent charge buildup from distorting the images. In this case, the coating would significantly alter the released devices, perhaps rendering them inoperable. Even a thin gold coating can dramatically decrease the

quality factor of resonant cantilevers [51], and so no conductive coatings were used. This may have reduced the image quality in some cases. The chips containing NEMS/GLEMS were also attached to the SEM stubs using carbon tape. While this method increases carbon contamination of the SEM system, it also allows the chips to be easily removed from the stubs, which is important to ensure they can be reused after SEM imaging.

The samples containing only GLAD films were prepared for SEM imaging much differently than the device-containing samples. The GLAD films were carefully cleaved from the quarter-wafer witness sample to ensure that one edge remained untouched to provide the best cross-sectional image possible. These samples, typically $\sim$1 cm^2 in area, were attached to the SEM stubs with silver paint. This provided a conductive path for the electrons to move from the sample to the stub. The samples were baked at 100 °C for 30 minutes in atmosphere to drive off the solvent in the Ag paint. Finally, the GLAD samples were coated with a thin layer ($\sim$1 nm) of chrome in order to improve the conductivity and image quality. Reducing the charging as much as possible was important for obtaining accurate film cross-sections and therefore GLAD film thickness measurements.

3.4.2 Optical Interferometry

The resonance frequencies of the devices were measured using the optical interferometry setup described in Reference [10]. During the measurements, the devices were kept under vacuum. The pressure was less than 1×10^{-5} Torr to prevent any damping from the surrounding air. The experimental setup used a helium neon (HeNe) laser operating at 633 nm wavelength to detect the motion of the NEMS. The laser was focused onto the NEMS using a microscope objective (50×, 0.45 numerical aperture). Alignment was performed by adjusting the x- and y- axes using a piezoelectric flexure stage. Rough alignment was performed manually; however, fine alignment was done by using computer software written in LabVIEW to control the stage. The focus was adjusted by manually moving the stage's z-axis. Once the laser was focused correctly, it reflected off both the resonating devices and the substrate underneath. The changing distance between the device and the substrate produced oscillating optical interference. The reflected signal was directed onto a photodiode by a 50/50 beam splitter. The photodiode converted the optical signal to an electrical signal, which was sent to a network analyzer. A schematic of the optical interferometry setup is shown in Figure 3.11.

The devices were actuated mechanically using a piezoelectric (PZ) disk. The

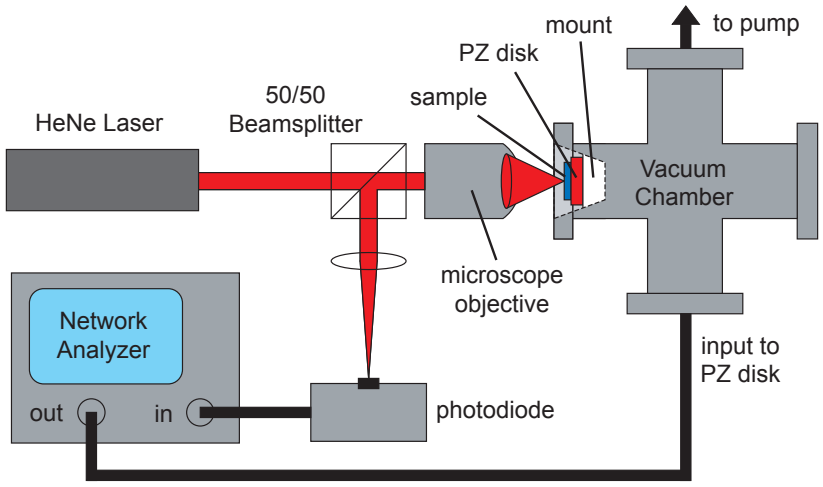

Figure 3.11: Schematic of the optical interferometry setup. The HeNe laser self-interferes when focused on the NEMS. The resonance signal is detected by the photodiode. The devices are mechanically actuated by a piezoelectric disk and read out using a network analyzer. Figure courtesy of Vincent Sauer; used with permission.

PZ disk takes an electrical signal from the network analyzer and converts it to mechanical motion. The NEMS chip was mounted on the PZ disk with double sided tape. The movement of the PZ disk shakes the NEMS, inciting mechanical vibration. The advantage of this actuation technique is simplicity; no on-chip electronics are required. The disadvantage is the narrow bandwidth offered by the PZ disk. The PZ disk has a frequency range of 1–20 MHz. At frequencies higher than 20 MHz, the PZ disk does not convert electrical signals efficiently, and so it does not produce significant mechanical vibrations at higher frequencies. This is the primary reason the device resonances are limited to less than 20 MHz, and why only the fundamental mode of the devices was studied in this thesis. Modes higher than the fundamental mode for the given geometries have resonance frequencies above or close to this 20 MHz threshold, making them difficult to detect. The power sent to the PZ disk can also be adjusted. For these experiments, the drive power to this disk was kept sufficiently low to maintain linear performance of the devices. High drive powers can lead to nonlinear behaviour, which is undesirable for this application [10].

The network analyzer is a very important part of the setup. The network ana-

lyzer is capable of driving and detecting the NEMS simultaneously. The input and output frequencies are swept over the same frequency range at the same time, which means that the NEMS are actuated specifically at their resonance frequency. When recording the frequency and phase data of the devices, a bandwidth of 300 Hz was used with 801 points in each scan. The span of each measurement ranged from 3 kHz to 100 kHz. This ensured that the data was not undersampled. A rule of thumb to ensure adequate sampling using the network analyzer is:

$$\frac{span}{bandwidth} < number\ of\ points \tag{3.1}$$

Using Equation 3.1, it can be verified that the largest span that can be sampled using a 300 Hz bandwidth and 801 points is 240.3 kHz. Since none of the spans measured exceeded 100 kHz, it is clear that adequate sampling was used to record the NEMS resonance and phase information.

During measurements, it is possible for the laser to heat the devices. Heating NEMS has been observed to shift their resonant frequencies and potentially degrade their quality factors of the devices [90]. In order to obtain the most accurate measurements, the laser power was reduced with a 1.0 neutral density filter to prevent heating of the NEMS. This, in combination with low drive powers, accounts for the relatively small amplitude of the measurements in comparison to other devices reported in the literature.

Both amplitude and phase measurements were obtained for each device measured. The amplitudes of the devices were measured linearly in frequency. The laser spot was focused on the centre of the DCBs and at the tip of the cantilevers to obtain an optimal signal. The signal was further optimized by adjusting the x-, y-, and z-axes of the flexure stage. Each curve was averaged on the network analyzer 16 times before capturing in order to reduce the noise. The data was captured using LabVIEW software connected to the network analyzer.

Chapter 4

Results and Analysis for NEMS

To understand the results obtained from the GLEMS, the results from the uncoated NEMS must first be examined. These results provide baseline data for the quality factors and resonance frequencies. This chapter will provide a detailed analysis of the uncoated NEMS. First, the more straightforward cantilever beams will be examined. The results from the uncoated DCBs will then be analyzed. The important findings from the uncoated NEMS will be summarized at the end of the chapter.

All of the data was recorded using the optical interferometry system described in Chapter 3. Additionally, the numerical values for the quality factors and resonance frequencies of the devices were obtained from the resonance curves by curve fitting using Equation 2.19. This method used nonlinear least squares regression in gnuplot (version 4.6) with the fitting variables γ, y_0, f_0, and Q. The curve fitting technique also outputs a percentage error for each fitting variable based on the fit. This is how the error in the quality factor and resonance frequency was obtained. The code used to fit the data, and a more thorough description of the curve fitting methodology, can be found in Appendix A. A sample resonance peak and corresponding phase data is shown in Figure 4.1. This data is for a cantilever device that is nominally 3.5 μm long. The fit to the amplitude is shown in the inset of Figure 4.1.

A minimum of three devices of each length (out of six possible devices) were measured to provide information about the variation in the resonance frequencies and quality factors. Minimal variation indicated that the fabrication process produced uniform devices, whereas significant differences in resonance frequency and quality factor indicated that the fabrication uniformity was poor. Measuring three devices was a good balance between obtaining sufficient data about the uniformity and minimizing the time spent performing the measurements. This improved the efficiency of the experiments.

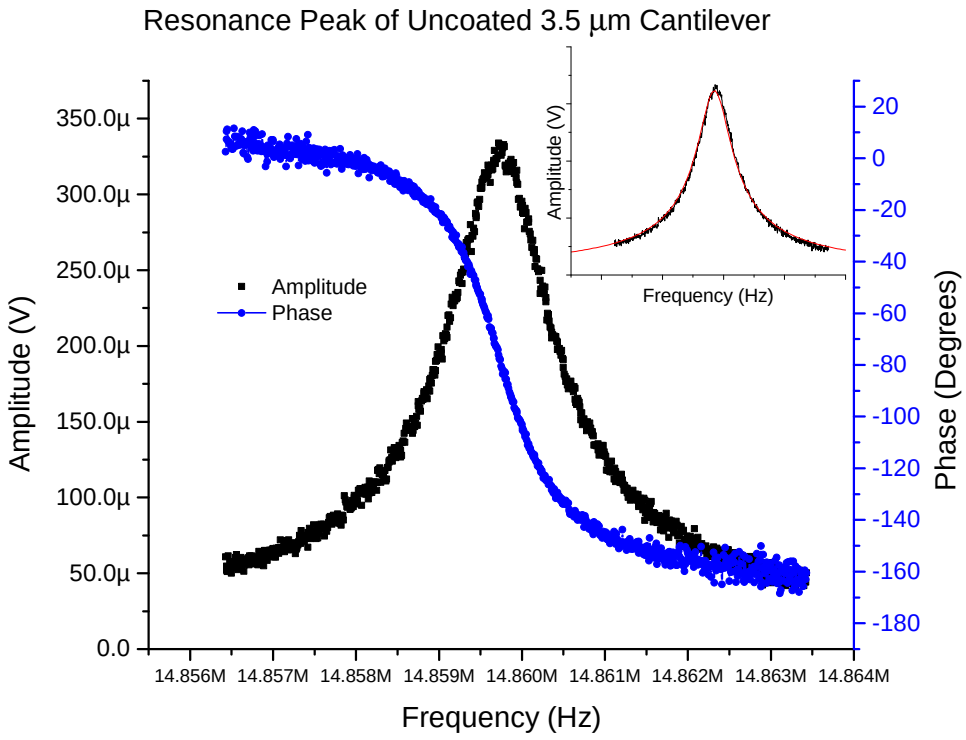

Figure 4.1: A sample resonance curve for a 3.5 μm long cantilever with no GLAD coating. The black curve shows that amplitude response and the blue curve shows the phase response. The inset shows the curve fit to the amplitude. The solid red line is the fit.

One device at a time was measured, starting with a column 1 device and moving along the row in increasing numerical order along each row according to Figure 3.8 until responses from three devices were measured. This meant that all devices of the same length were measured consecutively. Then, the laser spot was moved down to the next row and the measurements of the next length of device were made. For example, the cantilever measurements were done in the order a1, a2, a3, a4, etc. until responses from three "a" devices were successfully detected. Then, the "b" devices were measured, followed by the "c" devices. For the cantilevers, 30 resonance peaks were obtained. The same measurement strategy was used for the DCBs. Resonance peaks for the shortest DCBs, 7 μm long, were not detectable by the optical interferometry system. This is most likely because their resonance frequencies were above the 20 MHz frequency limit imposed by the PZ disk. Therefore, 21 resonance peaks were obtained for the DCBs instead of the desired 24 measurements.

Another experimental parameter that was important to quantify accurately was the length of the NEMS. There is uncertainty in the length of the devices because

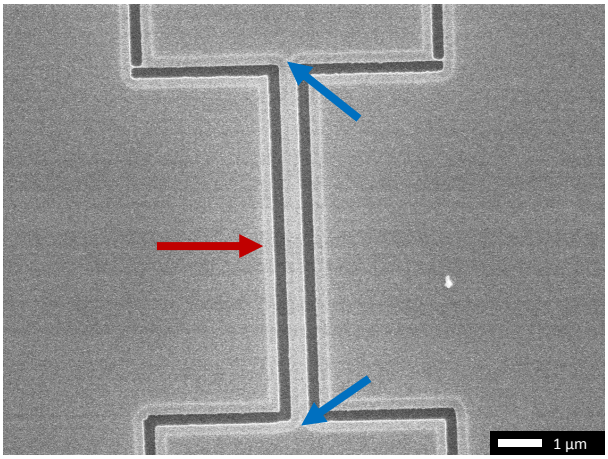

Figure 4.2: A standard NEMS DCB with nominal length 8 μm. The red arrow shows the bright line that is the edge of the undercut caused by the BOE etch. The blue arrows show the points between which the length measurements were taken.

the release step is a wet etch, which causes undercut in the beams. The undercut from the wet etch effectively lengthens the beams. In order to determine the actual length of the devices, SEM images were taken for both the cantilevers and DCBs. During the imaging, one device of each length was imaged using a slow scan rate to obtain an image that could be used to estimate the length of the device. Since the device layer is so thin, the undercut is visible on the SEM images. The released sections are brighter than the anchored sections, highlighted by the red arrow in Figure 4.2. Using image processing software called ImageJ, measurements of the length were made. The measurements were taken using a point-to-point line drawn between the centres of the released beams at the edge of the undercut. The blue arrows in Figure 4.2 show the two points between which the length was measured. These measurements were repeated five times for each image. The five measurements were averaged to give one overall length, with the standard deviation as the error in the length measurement. This method gave one length for each row of devices in Figure 3.8. Both the cantilevers and the DCBs were measured using this method. The nominal and measured lengths of the cantilevers are listed in Table 4.1. The nominal and measured lengths of the DCBs are listed in Table 4.2.

Table 4.1: Cantilever beam lengths were experimentally determined from SEM images. The corresponding error estimate is included with each measurement. The experimental lengths are compared to the nominal lengths.

Nominal length (μm)	Measured length (μm)
3.50	3.549 $\pm$ 0.009
3.75	3.852 $\pm$ 0.014
4.00	4.075 $\pm$ 0.013
4.25	4.275 $\pm$ 0.005
4.50	4.539 $\pm$ 0.015
4.75	4.862 $\pm$ 0.010
5.00	5.082 $\pm$ 0.004
5.50	5.646 $\pm$ 0.013
6.00	6.031 $\pm$ 0.021
7.00	7.042 $\pm$ 0.026

Table 4.2: Doubly clamped beam lengths were experimentally determined from SEM images. The corresponding error estimate is included with each measurement. The experimental lengths are compared to the nominal lengths.

Nominal Length (μm)	Experimental Length (μm)
7	7.122 $\pm$ 0.019
8	7.928 $\pm$ 0.036
9	8.831 $\pm$ 0.042
10	10.050 $\pm$ 0.051
11	11.280 $\pm$ 0.047
12	12.200 $\pm$ 0.031
13	13.266 $\pm$ 0.051
14	14.220 $\pm$ 0.065

To confirm the undercut added length to the NEMS, the measured lengths from Tables 4.1 and 4.2 were plotted against the nominal lengths listed in the same tables. Separate plots were done for the cantilevers and the DCBs, since the DCBs theoretically have twice the undercut of the cantilevers. These plots are shown in Figure 4.3a and 4.3b. Assuming the error in length introduced by the undercut was additive, the expected slope of these plots is 1. The slopes in both Figure 4.3a and 4.3b are very nearly 1; 1.03 $\pm$ 0.02 and 1.07 $\pm$ 0.02 respectively. These slopes are almost within error of 1. The errors listed in Tables 4.1 and 4.2 are due only to the image processing technique used to obtain the estimates for length, and do not reflect any of the error in the actual SEM itself. It is conceivable that the error is slightly larger, and therefore the slope could be within error of 1. This result confirms the undercut is adding a constant length to the devices, as expected.

An estimate of the undercut can be obtained by forcing the slopes in Figure 4.3

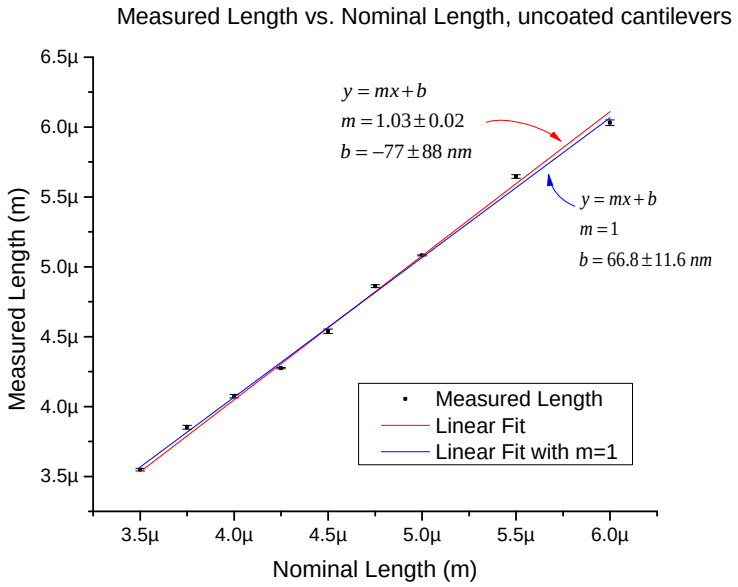

(a)

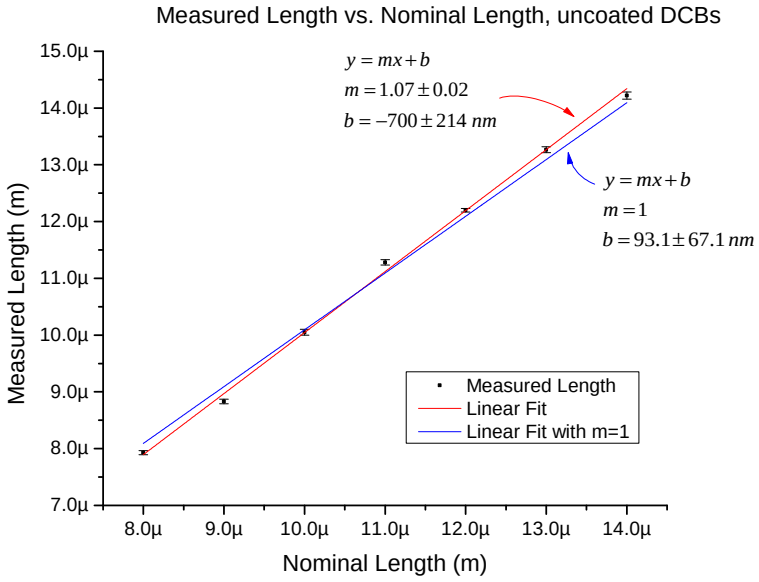

(b)

Figure 4.3: Measured length plotted versus the nominal length for (a) cantilevers and (b) DCBs. The slopes of both are very near 1. When the slope of forced to 1, the intercepts provide insight into the magnitude of the undercut.

to one, and examining the resulting y-intercepts. The y-intercepts represent an offset due to the undercut in the measured values compared to the nominal values. For the cantilevers, the y-intercept when the slope equals 1 is 66.8± 11.6 nm. For the DCBs, the y-intercept is 93.1± 67.1 nm. This intercept represents the magnitude of

the offset in length caused by the undercut. This means that the cantilever offset in length due to the undercut ranges from 55.2–78.4 nm. Likewise for the DCBs, the undercut ranges from 26.0–160.2 nm. Dividing the DCB value by 2 to account for both clamping points, the size of the undercut for the DCBs becomes 13.0–80.1 nm. The ranges obtained for the cantilevers and the DCBS overlap, indicating that the assessment of the undercut is consistent for both the cantilevers an DCBs. It can be concluded that the undercut adds a consistent length of ∼55.2–78.4 nm to each clamping point in the NEMS devices, effectively increasing their length.

The last parameter that is important in the analysis of the NEMS is the Young's modulus. The Young's modulus is a material parameter of the Si that varies depending on the crystal plane of the material [91]. Since it was unknown exactly which crystal plane the devices fabricated in this thesis were aligned with, an average value for the Young's modulus was used. This value, $E = 150$ GPa, is an average of the three possible values present in (100) Si.

Once the quality factors, resonance peaks, and lengths of the beams were determined, the analysis could be completed. The cantilevers will first be discussed, followed by the DCBs. In the analysis of the quality factors and the resonance frequencies, the measured lengths shown in Tables 4.1 and 4.2 were used for L.

4.1 Cantilevers

From the 6×10 array of cantilevers, results from three devices of each length were recorded for a total of 30 measurements. A total of 35 devices were tested, with five failed devices. Thus, the yield for the uncoated cantilevers was ∼86%. A sample cantilever resonance peak is shown in Figure 4.1.

The devices were imaged one day after the fabrication was completed. A single column of devices was imaged, however, the specific column was not recorded. This meant the electron beam was focused on that column of devices for much longer than the other devices on the chip, which proved to have ramification on the quality factor that will be discussed in the following section. When the imaging showed successful fabrication, the devices were tested using the optical interferometry setup the following day.

4.1.1 Quality Factor

The measured quality factors of the uncoated cantilevers are shown in Figure 4.4. In this graph, the quality factors of each device are plotted against the length. It is immediately apparent that there are two separate trends occurring in the data, forming two distinct datasets. One set had very high quality factors, ranging from (1.4–1.7)$\times 10^4$. The second set had reduced quality factors, from (0.6–1.1)$\times 10^4$.

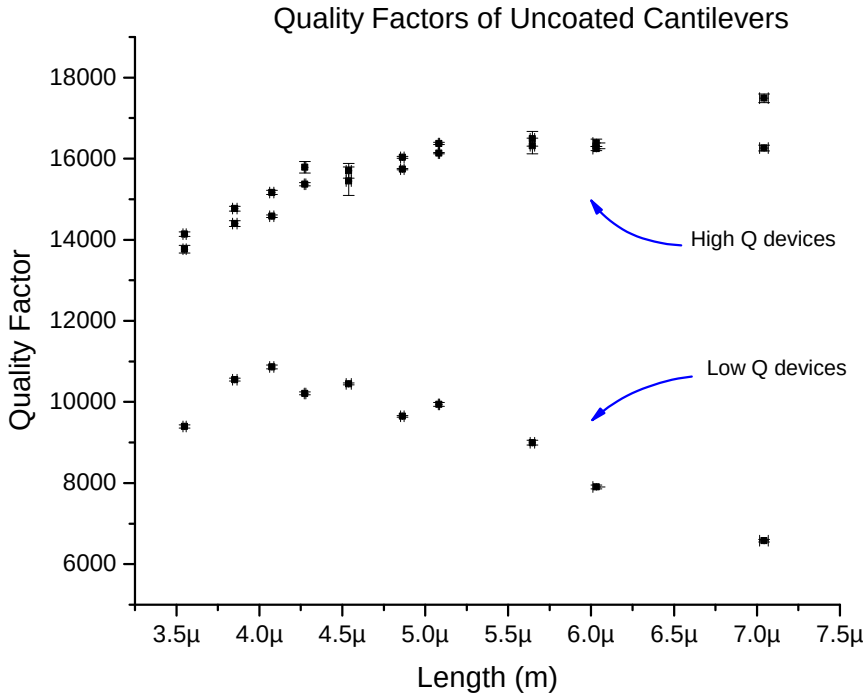

Figure 4.4: Quality factors of uncoated cantilevers. There are two trends in the data, one increasing as the length increases, and one decreasing as the length increases. The latter has a significantly lower Q.

After closely examining the data, it was noted that all of the devices with lower measured quality factors were from the third column. Theoretically, no difference in quality factor should have been observed between the different columns as the devices are almost identical. Furthermore, column 2 exhibits high quality factors and is adjacent to column 3. It was initially thought that the lower quality factors were due to column 3 being near or on the edge of the write field of the EBL. This meant that during the patterning of the devices, the electron beam had to deflect further to write the devices near the edge of the writefield. This could have caused an error in the third column of devices, reducing the quality factor. The devices were carefully imaged again using the higher resolution Hitachi S-4800. Two columns of

devices were imaged, columns 2 and 3. Although there was greater edge roughness for some of the devices in column 3 compared to column 2, there was no obvious difference to explain the dramatic difference in quality factor.

To determine if any other columns of devices were affected, the chip was re-measured in the optical interferometry setup. This time, only select device lengths were measured. The a, b, e, and g devices (Figure 3.8) were chosen as they had clear resonance peaks and contained no failed devices during the initial measurements . All six devices of each length were measured. The results are shown in Figure 4.5.

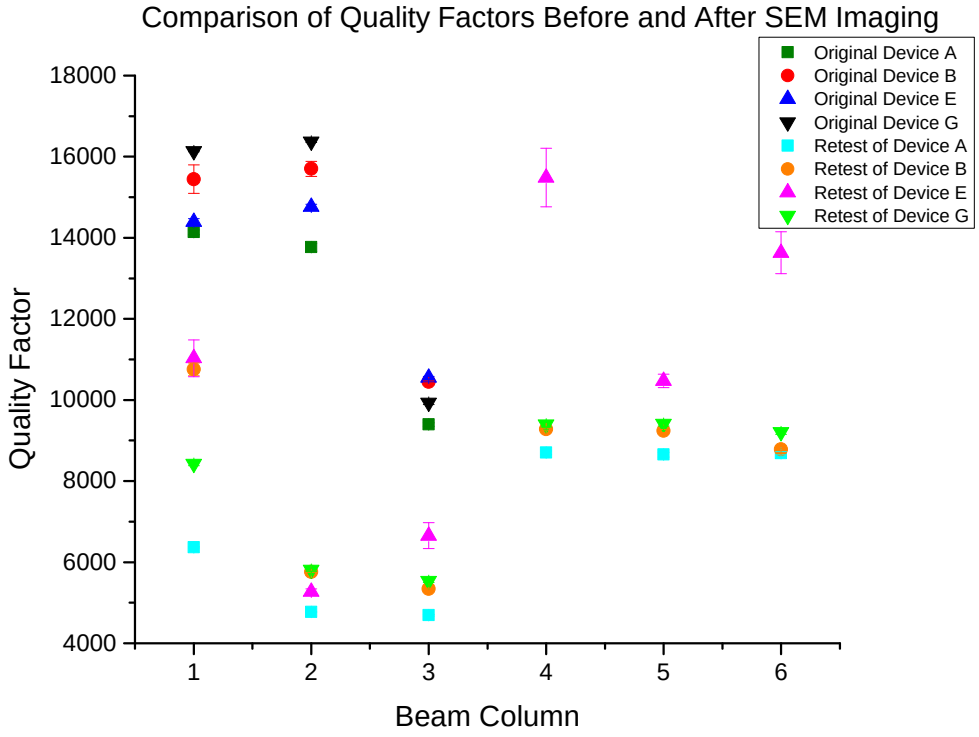

Figure 4.5: Comparison of quality factors of devices before and after SEM imaging. Column 2 devices show a substantial decrease in quality factor compared to devices of all other columns, indicating that damage during SEM imaging may be the cause of a decrease in Q.

The quality factors of the second measurements are lower than the initial measurements. This is to be expected as quality factors tend to degrade as the devices age due to surface contaminants and/or surface oxides [33]. The devices in columns 1 and 4–6 show fairly consistent quality factors. The Q for devices in column 3 are significantly lower, as expected. The devices in column 2 exhibit surprising behaviour. The quality factor has decreased much more significantly for the devices in

column 2 than any other column of devices, and the devices in column 2 now have Q's comparable to those observed in the column 3 devices. Additional imaging on the devices in columns 2 and 3 was the only change between the original measurements and the second measurements. Based on the observed decrease in Q of the devices in column 2, it can be concluded that SEM imaging has a fairly significant impact on the quality factor. By comparing the pre- and post-measurement SEM images, it was determined that the devices in column 3 were in fact the first devices imaged, and that SEM imaging was the cause of the original decrease in Q.

There are a few mechanisms for how SEM imaging could have reduced Q. Firstly, it is possible that carbon was deposited on the samples during imaging. Carbon contamination is a well-known phenomenon that has been studied for decades [92] and occurs because sources of carbon, such as carbon tape, are present in the SEM system. Carbon contamination could cause carbon to be deposited on the NEMS during imaging. This mechanism would also cause a frequency shift due to the added mass of the carbon on the sample. When examining the resonance frequencies of the column 2 devices before and after imaging, there is a consistent trend for the post-imaging measurements to be lower than the pre-imaging measurements, and so this is a possibility. However, the frequency shift could also be due to oxide growth or other surface contaminants, and so this evidence is not conclusive.

Another mechanism for the reduction in Q is damage to the silicon crystal lattice by the electron beam. High accelerating voltages (15–20 kV) were used in order to obtain high resolution images without the need for a conductive coating. High accelerating voltages increase the interaction volume of the electron beam with the sample and the energy of the electrons interacting with the sample, therefore increasing the possibility that electron-induced defects could be formed in the silicon. Defects are known to cause the quality factors of nanoscale resonators to decrease [18]. Regardless of the mechanism for device damage, it is clear that in the future more care should be taken to ensure the devices are measured before SEM imaging, or the SEM imaging is done on devices that will not be measured.

It is clear that some damage occurred to one third of the cantilever devices, reducing the Q substantially. The data from these devices will be removed from the remainder of the analysis. The devices labelled as "Low Q" in Figure 4.4 will be removed, leaving only the devices labeled "High Q". The high Q devices show a slight upward trend in quality factor as the length of the devices increases. This behaviour is consistent with both thermoelastic damping (Equation 2.13) and clamping loss (Equation 2.15), as well as many of the studies of Q in the literature [93, 44].

4.1.2 Resonance Frequencies

Sample resonance data is shown in Figure 4.1. The amplitude signal is a Lorentzian peak with a high signal-to-noise ratio. This result is typical of the uncoated cantilevers.

The resonance frequencies of the cantilevers are plotted versus their measured length in Figure 4.6. An initial look at the data shows that there is very little spread in frequency between devices of the same length. This indicates that the fabrication successfully produced uniform devices. The next step was to ensure that the measured data matched the theoretical behaviour for cantilevers described by Equation 2.10. The data was fit using Equation 2.10 using a least-squares regression in software called Origin 9, published by OriginLab. The fitting variable was the thickness of the SOI device layer. The fit produced a thickness of 147.5 $\pm$ 0.3 nm, which is well within the specification of 145 nm $\pm$ 10% provided by the SOI supplier. This result confirms the cantilevers are behaving as expected from Equation 2.10, and provides an experimental value for the thickness of the beams. This thickness is used in theoretical calculations throughout the remainder of this thesis.

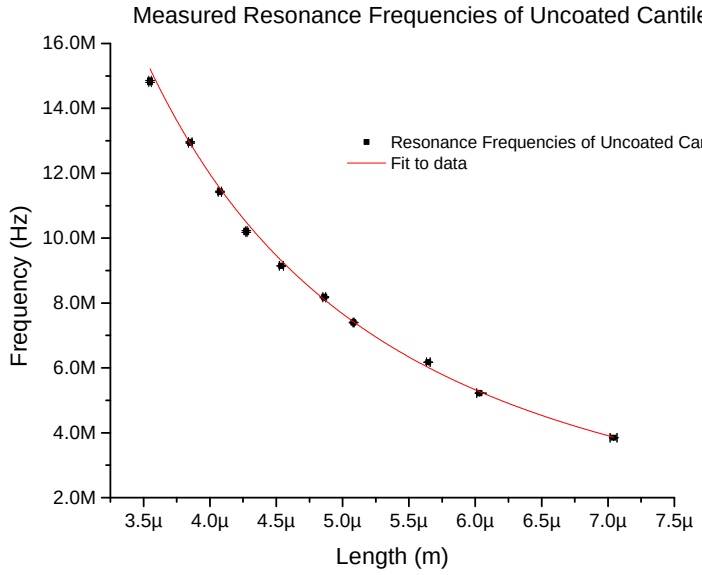

Figure 4.6: Resonance frequency plotted versus length of uncoated cantilevers. The data was fit using Equation 2.10 with the thickness of the device layer as the fitting variable. This produced a thickness of 147.5 $\pm$ 0.3 nm, well within the specifications of the SOI wafer.

4.1.3 Phase

In addition to the amplitude results, the phase data was examined. The phase changes of the cantilevers were 180° phase shifts, as expected. A sample phase measurement is shown in Figure 4.1 (blue curve). Another way to show the phase shift is to plot the phase in polar coordinates. This is shown in Figure 4.7 for the same data as Figure 4.1. The phase shift begins and ends at the origin and has a circular shape. This is a typical NEMS response, similar to that seen in the literature [22]. The result plotted in Figure 4.7 is representative of the other cantilevers.

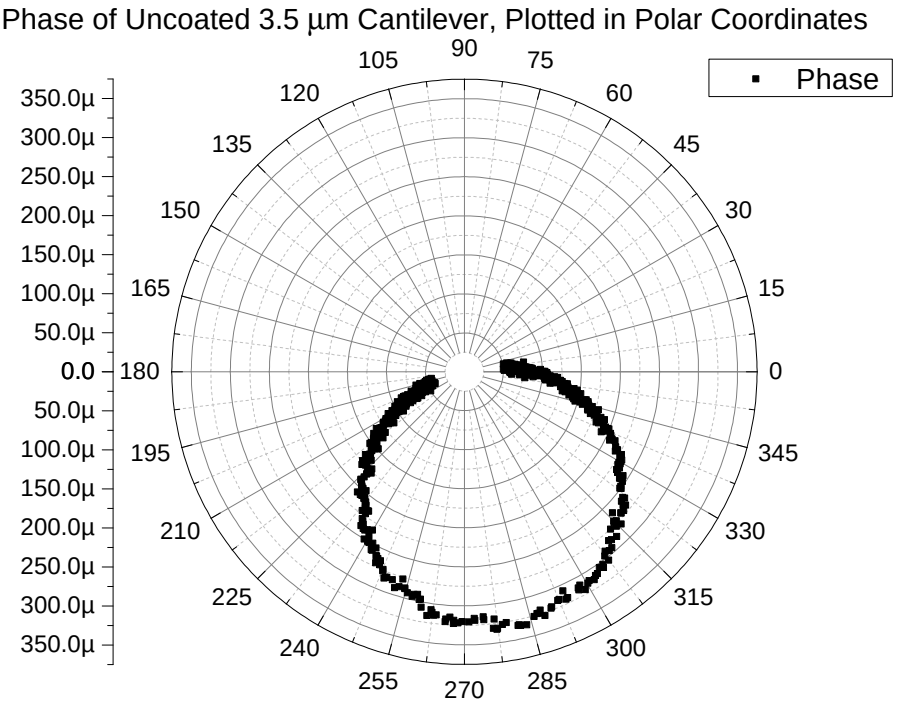

Figure 4.7: The phase shift for a 3.5 μm long cantilever has been plotted in polar coordinates. The phase goes through the origin and is circular, as expected.

4.2 Doubly Clamped Beams

The yield of the DCBs was 100%, which demonstrates successful fabrication. This yield excludes the shortest 7 μm beams. Since no resonance frequencies for these short beams could be found in the optical interferometry system, it was not conclusively determined whether or not they were functional. They could not, therefore, be included in the calculation of the yield. The devices were imaged at the same time as the cantilevers, and subsequently measured using optical interferometry. No

effect was apparent on the Q of the DCBs, indicating that the devices imaged were not measured. The 21 measurements taken for the DCBs are analyzed in the following subsections.

4.2.1 Resonance Frequencies

A sample resonance curve for a 10 μm doubly clamped beam is shown in Figure 4.8. The signal does not have as high signal-to-noise ratio as the cantilever resonance; however, the amplitude curve is still a Lorentzian response. This is a typical result for the uncoated DCBs.

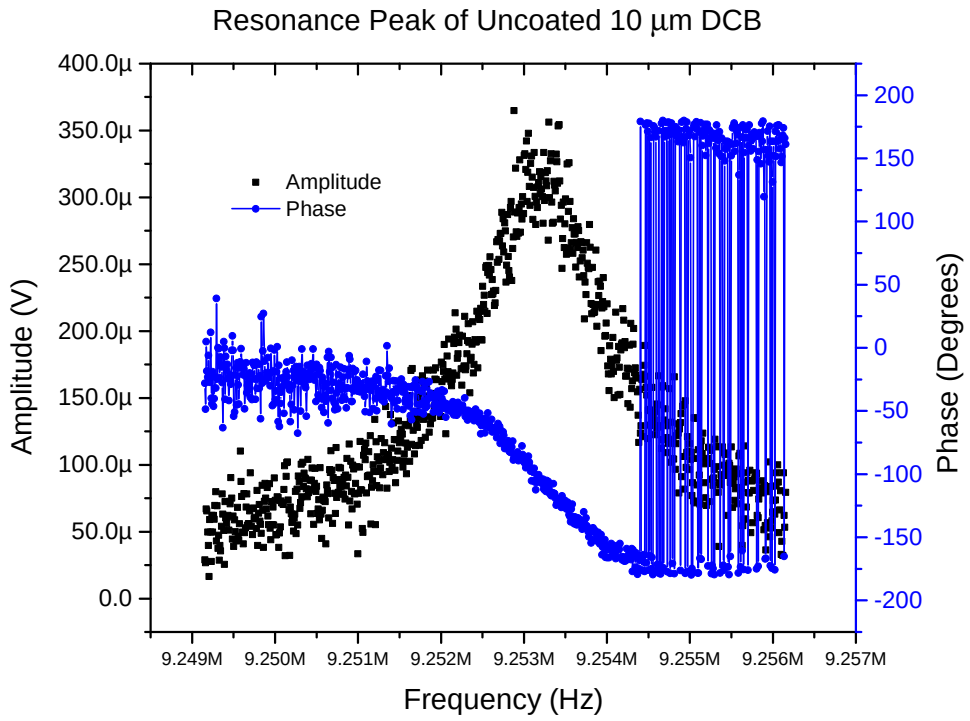

Figure 4.8: Sample resonance results for a 10 μm long uncoated DCB. The amplitude curve is a Lorentzian peak with a fairly narrow linewidth. The phase response is noisier than its cantilever equivalent. These results are typical of the uncoated DCBs.

The resonance frequencies of the DCBs are shown in Figure 4.9, and are substantially lower than predicted by the usual DCB resonance equation (Equation 2.5). The decrease in frequency was too large to be explained by erroneous length measurements, and so it was concluded that the sample must be under compressive stress. Many other devices fabricated from SOI in the literature show compressive

stress [35, 20]. As discussed in Chapter 2, both Equations 2.6 and 2.7 show how the resonance frequency can be modified to account for the effect of compressive stress.

The next step was to quantify the magnitude of the stress. This can be done by fitting the experimental data using either Equation 2.6 or Equation 2.7. The former has the advantage that it reduces to zero as the stress approaches zero, and has been used with success in other papers to describe the effects of tensile stress on DCBs [32, 33]. The latter, on the other hand, is advantageous because it separates the effects of the bending-induced stress and the residual stress. In this thesis, Equation 2.6 was used to fit the data, with the stress σ as the fitting variable. Equation 2.6 was chosen over Equation 2.7 because it reduced to the natural resonance frequency when $\sigma = 0$. It also produced a fit with a higher statistical correlation. The quantity used here to assess the quality of the fit is called the adjusted R^2. This a modified version of the determination coefficient. Here it has been adjusted to reflect the effect of increasing the number of fitting variables in the system, and prevent an increase in the number of fitting variables from artificially raising the R^2 value. The adjusted R^2 is a statistical measure of the distance between the data and the fit. An R^2 value of 1 indicates a perfect correlation, whereas an R^2 of 0 represents no correlation. In this way, the adjusted R^2 can provide feedback on the quality of the fit. For a more complete description of the adjusted R^2 and how it is calculated, the reader should refer to References [94], [95], and [96]. The first is an excellent textbook on the design of experiments, the second a textbook describing error analysis and linear regression, and the latter describes how the adjusted R^2 is calculated specifically in the Origin software. Fitting with Equation 2.6 produced $R^2 = 0.97027$. Fitting with Equation 2.7, alternatively, produced $R^2 = 0.96309$. The correlations of both fits are similar, however, the fit using Equation 2.6 had a slightly improved correlation.

The fit, shown in Figure 4.9, produced a value of $\sigma = -32.5 \pm 0.3$ MPa. The negative sign indicates compressive stress, as expected. This value agrees very well with other values for built-in stress in SOI found in the literature. For example, Iwase *et al.* found that their SOI had a stress of -39 MPa [35]. Visually, the fit correlates well at longer lengths but poorly at shorter lengths. The exact mechanism for this is uncertain. From a mathematical standpoint, it is possible that Equation 2.6 begins to fail as the length of the DCBs approaches zero. This is because as the length becomes very small, the stress term will have a much smaller contribution to the resonance frequency. In the case of a compressive stress, this will cause the equation to overestimate the resonance frequency at short beam lengths.

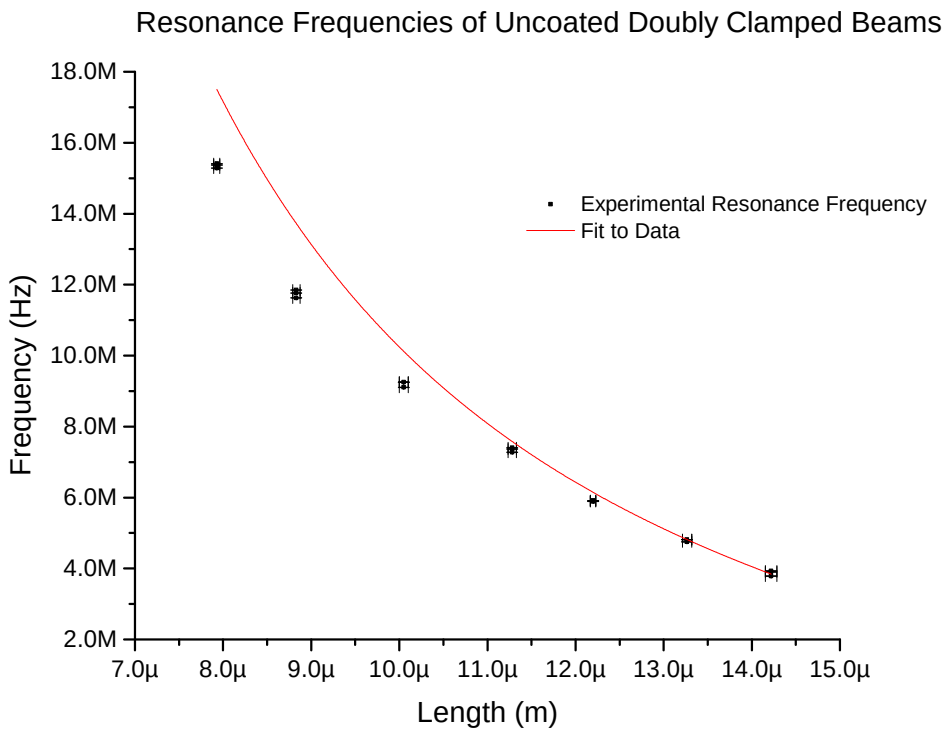

Figure 4.9: Resonance frequencies of DCBs versus length. The frequencies are much lower than expected, leading to the conclusion that compressive stress is present in the SOI. The results have been fitted using Equation 2.6, with σ as the fitting variable. The fit resulted in a stress of $\sigma = -32.5 \pm 0.3$ MPa.

It is also possible that there is a physical mechanism causing the deviation at shorter beam lengths. Stress is a complex phenomenon that may have unknown effects on the DCBs. The majority of the literature discussing compressively stressed DCBs relates to buckling. To ensure that buckling is not a concern in this work, the critical buckling length can be calculated using Equation 2.9. Substituting in $\sigma = -32.5$ MPa, the critical buckling length is found to be $L_c = 18.2$ μm, which is substantially longer than any of the beams fabricated in this work. Therefore, the DCBs are not near the buckling threshold, and buckling is likely not the cause of the poor fit in Figure 4.9. The lack of buckling is further validated by SEM imaging, as no buckled beams were observed when the devices were imaged. Some other mechanism, likely related to the large compressive stress, could be affecting the frequencies of the uncoated DCBs.

The highest resonance frequencies in Figure 4.9 are at ~15 MHz, and are for the 8 μm beams. Extrapolating the trend to estimate the resonance frequencies of the 7 μm beams indicates that the resonance frequencies would be close to 20 MHz,

which explains why these resonance peaks are not visible in the optical interferometry system.

4.2.2 Quality Factor

The quality factors of the uncoated DCBs are plotted in Figure 4.10. There is a fairly large spread in Q between devices of the same length. The Q also decreases as the length increases, which conflicts with the trends exhibited by both thermoelastic dissipation (Equation 2.13) and clamping loss (Equation 2.15). It seems as though there is another dissipation mechanism at work in the uncoated DCBs.

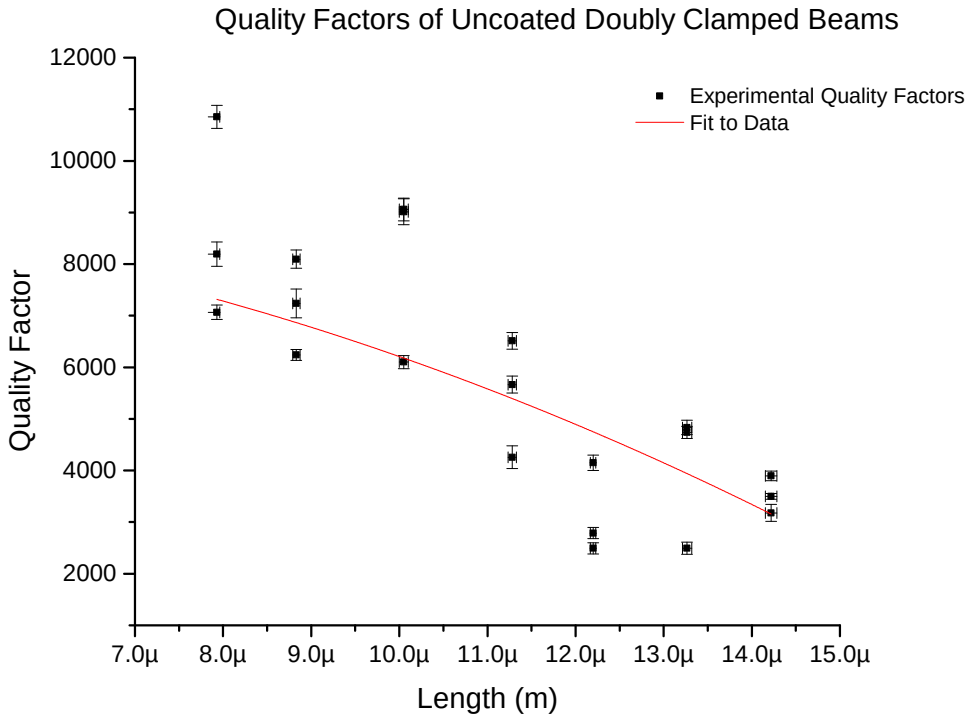

Figure 4.10: Quality factors of uncoated DCBs. The quality factors tend to decrease as the length increases. The data has been fit with Equation 4.6, with σ and E_2 used as fitting variables. The fit results in $\sigma = -35.9 \pm 3.5$ MPa and $E_2 = 16.3 \pm 1.6$ MPa.

In a recent work by the Kotthaus group, a model was derived for the effect of tensile stress on damping in nanostrings [18]. Their model is general, and here it has been modified to describe the dissipation in compressively stressed DCBs. The basis of this model is the expression of stress as function of both a real Young's modulus and complex Young's modulus:

$$\sigma = (E + iE_2)\epsilon \tag{4.1}$$

where E_2 is the complex Young's modulus and ϵ is the strain. The idea behind adding a complex Young's modulus to the standard stress-strain relation is that the complex modulus can be used to describe the dissipation in the system. For this reason, the complex Young's modulus is often called the loss modulus.

The next important equation from Reference [18] describes the energy loss per cycle based on the presence of the complex Young's modulus:

$$\mathrm{d}(\Delta U) = \pi E_2 \frac{wt_b}{8} \left(\frac{\partial u(x)}{\partial x} \right)^4 \mathrm{d}x + \pi E_2 \frac{wt_b^3}{12} \left(\frac{\partial^2 u(x)}{\partial x^2} \right)^2 \mathrm{d}x \tag{4.2}$$

where ΔU is the energy lost in the beam over one oscillation and $\mathrm{d}x$ is the differential element in the x-direction (along the length of the beam). The first term in this equation can be attributed to the elongation loss, and the second term is due to the bending loss. The elongation loss is caused by the beam stretching as it oscillates, and the bending loss is caused by the beam bending as it oscillates.

In order to simplify Equation 4.2, the authors have assumed the loss due to bending is much greater than the loss due to elongation. This permits the elimination of the first term in Equation 4.2 and greatly decreases the complexity of the model. Despite the fact that this assumption is made for very long nanostrings, it is also valid for the shorter DCBs in this work. Upon substitution of the mode shape $u(x)$ (Equation 2.4) into Equation 4.2, the assumption that the bending loss is greater than the elongation loss reduces to a simpler assumption, which is that the thickness of the beam is much greater than the amplitude of vibration. This can be confirmed by calculating the critical amplitude of the DCBs. Above the critical amplitude, the devices behave nonlinearly. As all of the measurements made in this study were in the linear regime, the amplitude of the DCBs cannot be above the critical amplitude. The critical amplitude can be calculated as follows [97]:

$$a_{cr} = 1.685 \frac{t_b}{\sqrt{Q}} \tag{4.3}$$

Assuming a lower bound of $Q = 2000$ for the DCBs from Figure 4.10 and substituting in the measured thickness from Section 4.1.2 t_b=147.5 nm, the critical amplitude is ∼5.6 nm, which is substantially lower than the thickness of the beam. This indicates that the elongation loss is negligible for the DCBs and the dissipation therefore becomes:

$$\Delta U = \pi E_2 \frac{wt_b^3}{12} \int_0^L \left(\frac{\partial^2 u(x)}{\partial x^2} \right)^2 \mathrm{d}x \tag{4.4}$$

Similarly, the total energy of the beam can be described in terms of the stress and the Young's modulus as follows:

$$U = \int_0^L \frac{wt_b\sigma}{2}\left(\frac{\partial u(x)}{\partial x}\right)^2 + \frac{Ewt_b^3}{24}\left(\frac{\partial^2 u(x)}{\partial^2 x}\right)^2 \mathrm{d}x \tag{4.5}$$

For a more complete derivation of these equations, please refer to the Supplementary Information of Reference [18].

The quality factor can be calculated as described in Equation 2.11. Substituting in the values for ΔU, U, and the mode shape $u(x)$ (Equation 2.4), then integrating over the length, an expression for the Q as a function of σ and E_2 can be obtained. This expression is as follows:

$$Q = \frac{0.295\sigma L^2}{E_2 t_b^2} + \frac{E}{E_2} \tag{4.6}$$

As the stress approaches zero, the equation for Q is defined simply as the ratio of the Young's modulus to the loss modulus, which agrees with the results found by Yasumura *et al.* in Reference [43]. To assess the validity of this expression, it has been fit to the data obtained from the DCBs in this study. The fitting variables were the stress σ and the loss modulus E_2. The fit can be seen as the solid red line in Figure 4.10. From this fit, $\sigma = -35.9 \pm 3.5$ MPa and $E_2 = 16.3 \pm 1.6$ MPa. The error is relatively high compared to the fit obtained in Figure 4.9; however this is not unexpected given the large spread in the Q data. The stress obtained from this fit matches within error to the stress value obtained in the previous section (Figure 4.9). It is difficult to state the validity of the value obtained for E_2, as the loss modulus is typically only measured experimentally for elastic materials such as polymers. Little information exists in the literature for the loss modulus of silicon.

From a more qualitative standpoint, Equation 4.6 shows how the quality factor varies with the length if a compressive (or tensile) stress is present. Equation 4.6 works well to explain why the Q is decreasing as the length of the beams increases, in contrast to other DCBs observed in the literature. The presence of a compressive stress is clearly detrimental to Q. In the future, compressive stress should be avoided. Suggestions to avoid compressive stress include choosing a different substrate, such as high tensile stress SiN, or fabricating cantilever structures that are not subject to compressive stress.

4.2.3 Phase

Figure 4.11 shows a polar phase plot for a standard DCB. The plot shown here is representative of the other uncoated DCBs. The phase meets at the origin and shows a 180° phase shift. In the phase results for the DCBs, there is often a slight asymmetry in the phase change when plotted in polar coordinates. This can be seen in Figure 4.11. This could mean there is background phase noise in the system that is causing asymmetry in the phase. Phase noise may be introduced by the PZ disk used to drive the devices. The PZ disk has its own unique resonances and can therefore introduce phase noise into the system. Since most of the DCBs exhibit this slight asymmetry regardless of their resonance frequencies, it is more likely that it is a feature of the devices themselves and not due to the PZ disk. The exact mechanism behind this slight phase asymmetry is uncertain.

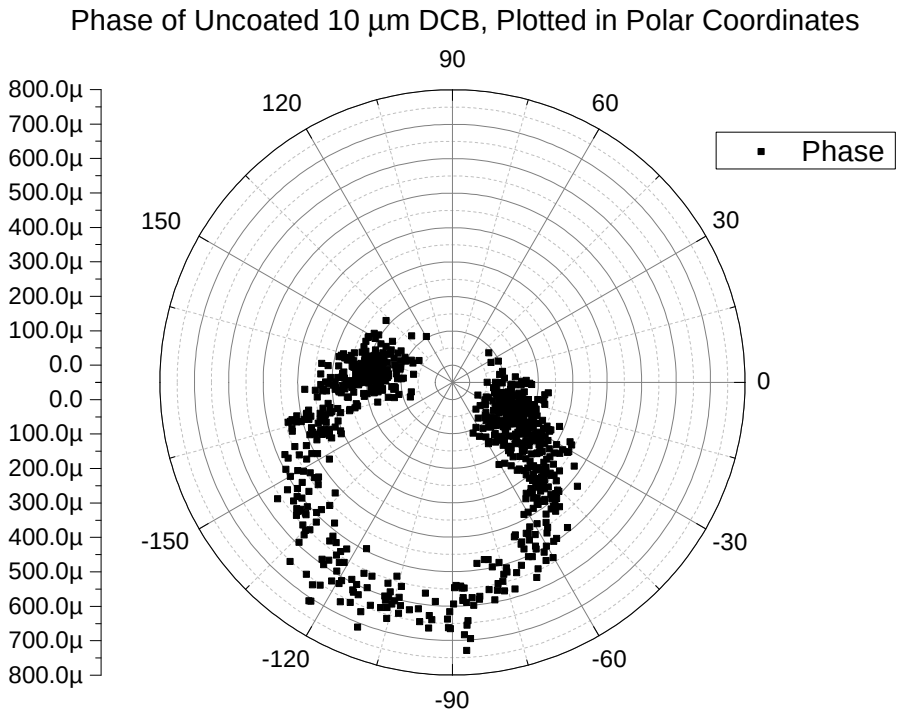

Figure 4.11: Phase shift on resonance for an 10 μm uncoated DCB. This phase data is the same shown in Figure 4.8, plotted in polar coordinates. This result shows a very slightly asymmetric phase change.

4.3 Summary of NEMS Analysis

The most important findings from the uncoated NEMS will be carried over into the analysis of the GLEMS. Table 4.3 shows a summary of the important values obtained from the curve fitting analysis described in this chapter. In addition to these values, the lengths listed in Table 4.1 and Table 4.2 will be used in future analysis.

Table 4.3: Summary of important results from the NEMS. These results will be used in Chapter 5 for the analysis of the GLEMS.

t_b	=	147.5 $\pm$ 0.3 nm
σ	=	$-32.5\pm$ 0.3 MPa

Chapter 5

Results and Analysis for GLEMS

This chapter will present the results and analysis for the GLAD-coated NEMS (GLEMS). First, the quality factors of the GLEMS will be discussed. Then, the effects of the GLAD coating on the resonance frequencies of the devices will be analyzed. A theoretical model for the resonance frequencies of the GLEMS will be derived. Finally, the effects of the GLAD film on the phase responses of the devices will be presented.

The GLEMS were measured using the identical methodology used for the uncoated devices. The optical interferometry system was used to detect the amplitude and phase responses of the GLEMS. Curve fitting was used to extract the resonance frequencies and quality factors. As the length of the beams was difficult to determine after the GLAD films had been deposited, the lengths from Tables 4.1 and 4.2 were used in the analysis of the GLEMS. Since all of the coated and uncoated devices were fabricated simultaneously on the same chip, they were essentially identical and the use of the measured lengths from Tables 4.1 and 4.2 is appropriate.

Two thicknesses of GLAD films were investigated, a film nominally 100 nm thick and a film nominally 300 nm thick. The thicknesses of the GLAD films were measured using SEM images of the film cross-sections. The samples were carefully prepared for cross sectional imaging using the method described in Chapter 3. The film thicknesses were measured using ImageJ. The thicknesses were measured five times, and from these five measurements an average thickness and a standard deviation were obtained. The nominally 100 nm thick film was measured to have a thickness of $t_{\mathrm{f}}^{100\mathrm{nm}} = 113.7 \pm 1.7$ nm. The nominally 300 nm thick film was measured to have a thickness of $t_{\mathrm{f}}^{300\mathrm{nm}} = 324.4 \pm 8.1$ nm. These experimental values for thickness are used for various calculations throughout this chapter.

5.1 Quality Factor

The quality factors of the coated devices are plotted with the uncoated devices for comparison in Figures 5.1 and 5.2. Figure 5.1 shows the results for the cantilevers, and Figure 5.2 shows the results for the DCBs.

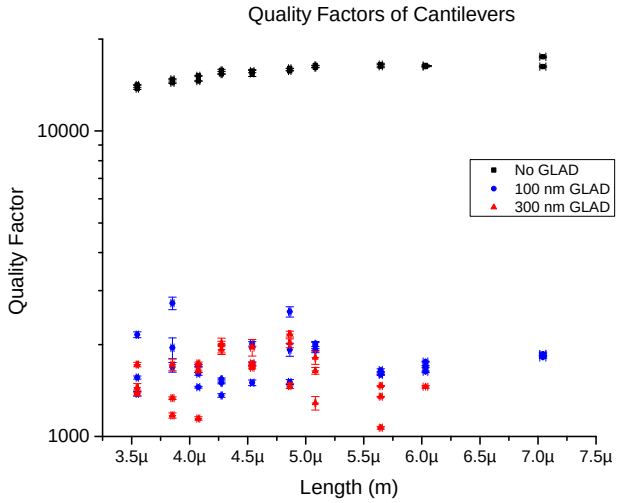

Figure 5.1: Quality factors of uncoated and coated cantilevers. There is approximately a one order-of-magnitude decrease in Q between the uncoated and coated devices. There is no effect of the coating thickness on Q.

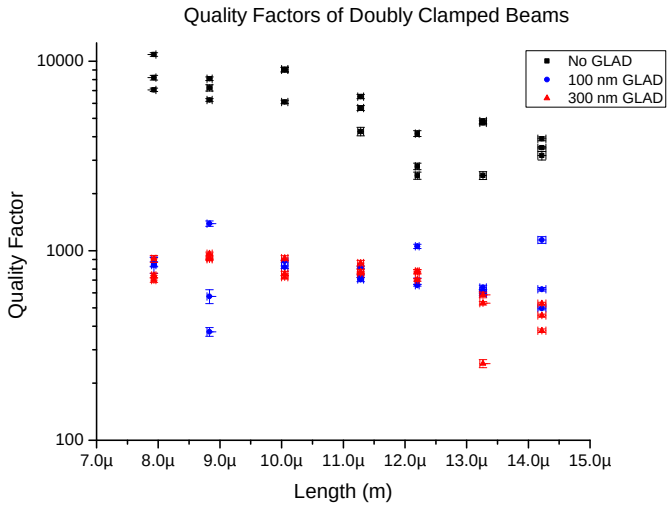

Figure 5.2: Quality factors of uncoated and coated DCBs. The quality factor is approximately one order-of-magnitude lower for the coated devices. There is no effect of the coating thickness on the Q.

For the cantilevers, the coating causes a clear one order-of-magnitude decrease in the quality factors. There is no apparent difference between the quality factors of the cantilevers coated with 100 nm of GLAD film and the cantilevers coated with 300 nm of GLAD film. Additionally, the uncoated cantilevers show increasing quality factors as the length increases, however, the coated devices do not follow this trend. Similarly for the DCBs, the GLAD coating results in an order of magnitude decrease at shorter beam lengths. As the beam length increases, the quality factors of the uncoated devices decrease due to the effect of the compressive stress, as discussed in Chapter 4. The coated devices do no exhibit this trend, and maintain a constant quality factor for all beam lengths. This indicates that the Q's of the coated DCBs are not limited by the residual compressive stress; rather, another mechanism is causing the reduction in Q.

As discussed in Chapter 2 (Equation 2.12), there are many possible sources of dissipation in NEMS. To determine which is the most probable in the GLEMS, each source of dissipation can be examined. The easiest to eliminate as a potential cause is viscous damping, because all of the measurements were done in vacuum. TED should also not be a major cause of damping because the devices are relatively large. For example, the smallest device in this thesis is a cantilever 3.5 μm long, and would therefore have the greatest TED. For this device, Equation 2.13 predicts a quality factor of approximately 5×10^4, whereas the actual quality factor is 1.4×10^4. This indicates that the quality factors observed for these devices are below the threshold for TED. The GLAD film may have some effect on the TED, however, this is difficult to test without subjecting the GLEMS to very low temperatures, for which a special experimental setup is required.

The clamping loss can also be examined. According to Equation 2.15, the smallest cantilever will have the highest clamping loss. This devices has a predicted Q_{clamping} of 8×10^6, which is several orders of magnitude greater than the observed quality factor. This means that clamping loss should not be responsible for the dissipation in the uncoated devices. For the GLEMS, however, clamping loss may still be a mechanism because the effect of GLAD films on the clamping loss is unknown. To experimentally test whether the clamping loss was a factor, the modified devices with narrowed clamping points (described in Section 3.3) can be examined. Examples of these devices are shown in Figures 3.9a and 3.9b. The width of the clamping points in these devices was 100 nm. If clamping loss was the dominant mechanism, a significant difference in the quality factors of the coated modified devices compared to the coated cantilevers and DCBs should be observed. A plot of the quality factors of the modified devices is shown in Figure 5.3. The modified devices also

showed a one order-of-magnitude decrease in quality factor when compared to the uncoated devices. This indicates clamping loss is not the dominant mechanism in the GLEMS, as the narrowed clamping point did not significantly change the loss experienced by the coated devices.

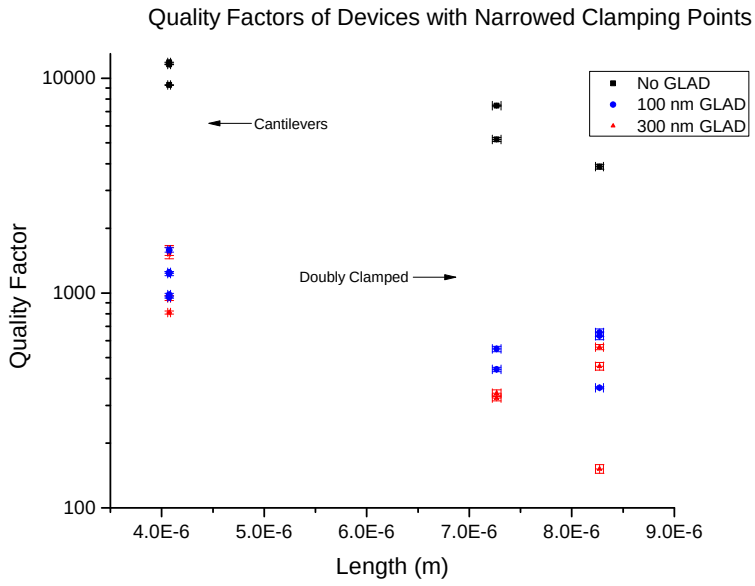

Figure 5.3: Quality factors of uncoated and coated devices with narrowed clamping points. Each device shows approximately a one order-of-magnitude decrease in quality factor after GLAD coating.

It is interesting to note that the 100 nm GLAD coating and the 300 nm GLAD coating produce the same quality factors. This is in direct contrast to the literature, where it is observed that increasing the thickness of the sensing layer has a direct and detrimental effect on Q. One work by the Boisen group showed that only 100 nm of Au on a cantilever caused an order of magnitude decrease in Q, and that subsequently thicker films worsened Q further [51]. Another example can be found in a 2007 paper by Dufour, in which the losses caused by the sensing layer were explained by including the viscoelastic properties of the sensing layer. This resulted in an equation for Q that was highly dependent on the thickness of the sensing layer [52]. The primary difference between typical sensing layers, such as polymers or Au, and the GLAD films is that the GLAD coating is made up of nanostructured pillars and does not act as a solid, viscoelastic layer. Instead, the posts flex with the beam motion and do not interact. Thus, no additional damping should be introduced as the film thickness increases, which is in fact observed in Figures 5.1 and 5.2. Since the thickness of the film does not significantly affect the dissipation, the dissipation is most likely caused by a surface effect of the GLAD film, instead of a bulk effect.

The question becomes how the presence of GLAD films, regardless of thickness, can substantially decrease the Q. The answer lies in the GLAD film growth mechanism.

Studies of GLAD films have shown that during the initial nucleation phase of GLAD growth, different materials nucleate in different ways. This is due to the surface energy of the materials. Lower surface energy materials such as Sn tend to form hemispheres as a more favourable energy state. Higher surface energy materials (such as SiO_2) better wet the substrate surface and are therefore more spread out during the initial nucleation phase [98]. At high deposition angles, the strong effect of shadowing quickly forms columnar structures; however, the initial few tens of nanometres of nucleation layer may still be fairly continuous. Even a thin continuous layer is likely sufficient to reduce the Q by a full order of magnitude. To assess whether the SiO_2 films grown in this thesis are connected at the base of the posts by a continuous layer, SEM images of the 100 nm thick and 300 nm thick GLAD film witness samples were taken. These are shown below in Figure 5.4.

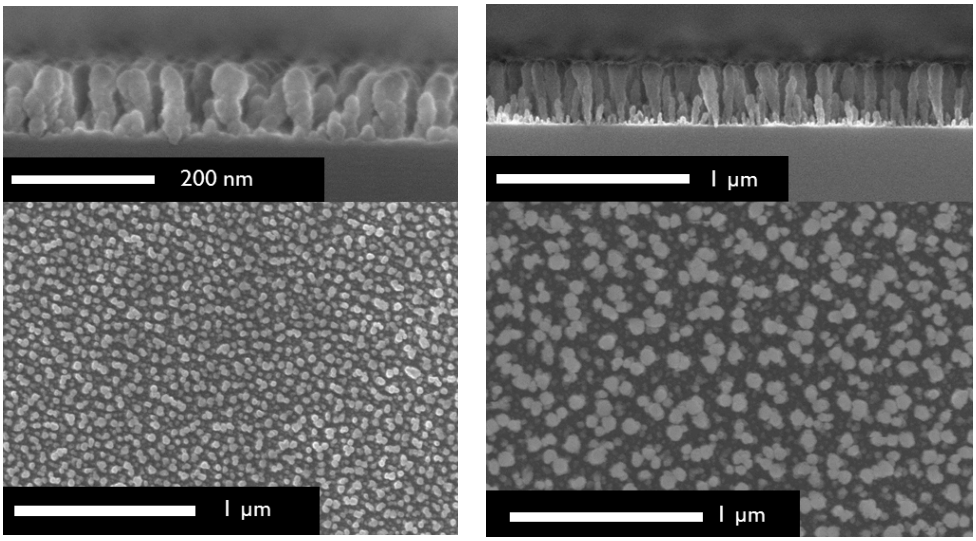

(a) (b)

Figure 5.4: Cross sections (top) and top-down (bottom) views of (a) 100 nm thick GLAD posts and (b) 300 nm thick GLAD posts. At the base of the cross sectional views, a thin layer of quasi-continuous film is observed. The 100 nm posts are also closer together than the 300 nm posts with a significant amount of material visible between the larger posts. In (b), the nucleation layer is obscured by the taller, wider posts. These images suggest there may be a quasi-continuous layer at the base of the GLAD film.

In Figure 5.4a, the 100 nm GLAD film is imaged both from a top-down view and a cross sectional view. In the cross section, an uneven, quasi-continuous base layer is present. There is also a significant amount of material between the larger posts,

indicating that the posts may be more connected at their bases. These effects are not as visible in the thicker films as the shadowing mechanism dominates to form well-separated posts (Figure 5.4b). From these images, it appears that the bases of the posts are connected by a quasi-continuous layer. This quasi-continuous layer is clearly sufficient to decrease the Q by one order of magnitude. Fortunately, since increasing this thickness of the GLAD posts does not have any noticeable effect on Q, the GLAD film thickness could be increased past 300 nm. This would have a beneficial effect on the LOD (Equation 1.1) both in terms of the sensing layer thickness and increased surface area.

5.2 Resonance Frequencies

The addition of the GLAD films causes a noticeable decrease in the resonance frequencies of both the cantilevers and doubly clamped beams. First, the results from the cantilevers will be examined. Then, the results from the DCBs will be analyzed based on the findings from the cantilevers.

5.2.1 Cantilevers

Sample resonance frequencies of 100 nm and 300 nm GLAD-coated cantilevers are shown in Figure 5.5. The signal-to-noise ratio is lower in both cases than the uncoated case examined in Chapter 4.

The resonance frequencies of the GLEMS are lower than the uncoated devices, and are plotted versus the cantilever length in Figure 5.6. This is unsurprising, as the added mass of the GLAD film should decrease the resonance frequency due to the mass loading effect described in Equation 2.20. Equation 2.20 cannot, however, be used to predict the frequency shift caused by the added mass of the GLAD film because this equation assumes the added mass is a small fraction of the overall mass of the resonator. In the case of the GLEMS, the added mass of the GLAD thin film is 15% of the overall beam mass for the 100 nm films, and 44% of the overall beam mass for the 300 nm films. These are clearly not small fractions of the overall resonator mass, and so a different approach must be used to calculate the resonance frequencies. Using the method of Sader [99], an alternative formula can be derived to account for the mass of the added GLAD film. This equation can be used to predict the resonance frequencies of the GLEMS. The method described by Sader involves correcting density and Young's modulus to account for the contributions from the additional thin film. In this case, only the density contribution is included. This is because the GLAD films are composed of independent, isolated pillars, and

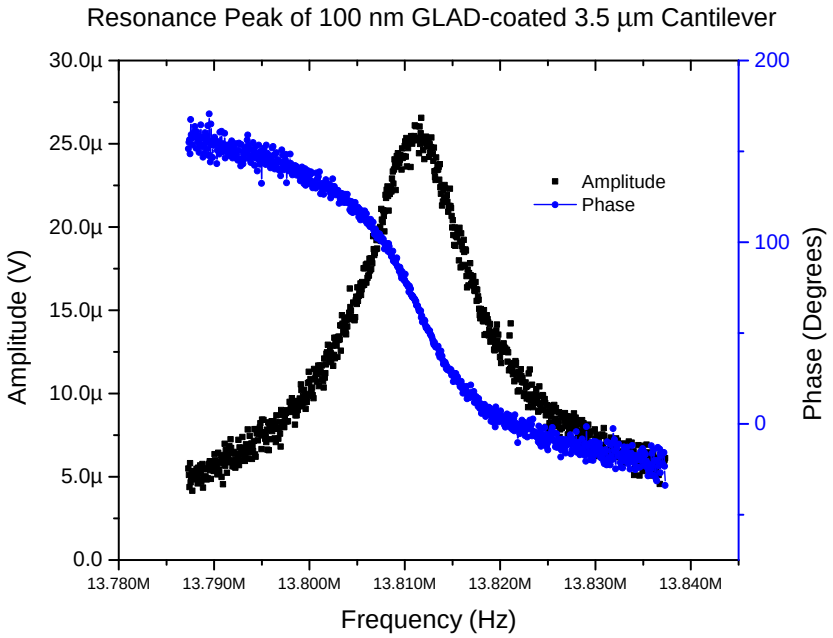

(a)

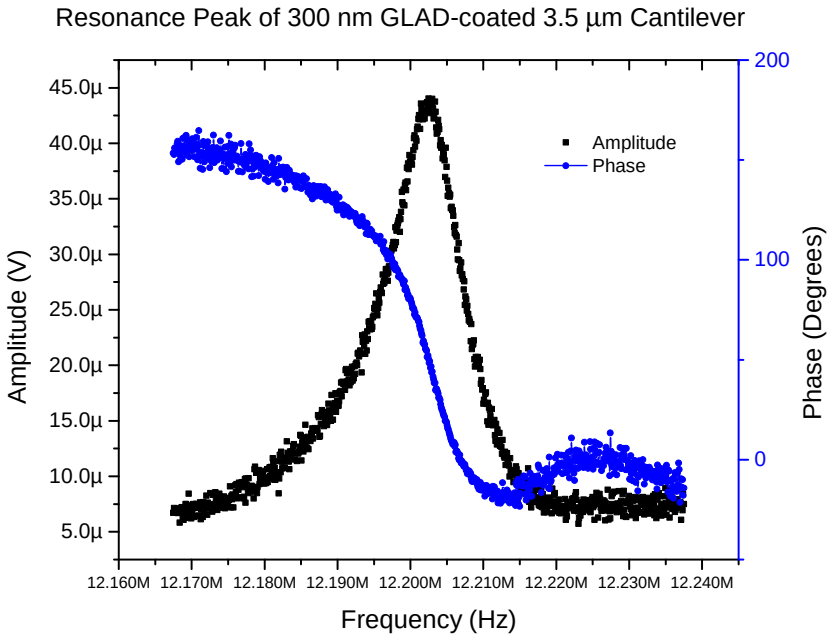

(b)

Figure 5.5: Sample resonance frequencies and phase shifts of (a) 100 nm GLAD-coated and (b) 300 nm GLAD-coated cantilevers. Both devices are 3.5 μm long and are representative of the other coated cantilevers.

so it is assumed that the mechanical contribution to the system is negligible. Therefore, no modification of the Young's modulus is required.

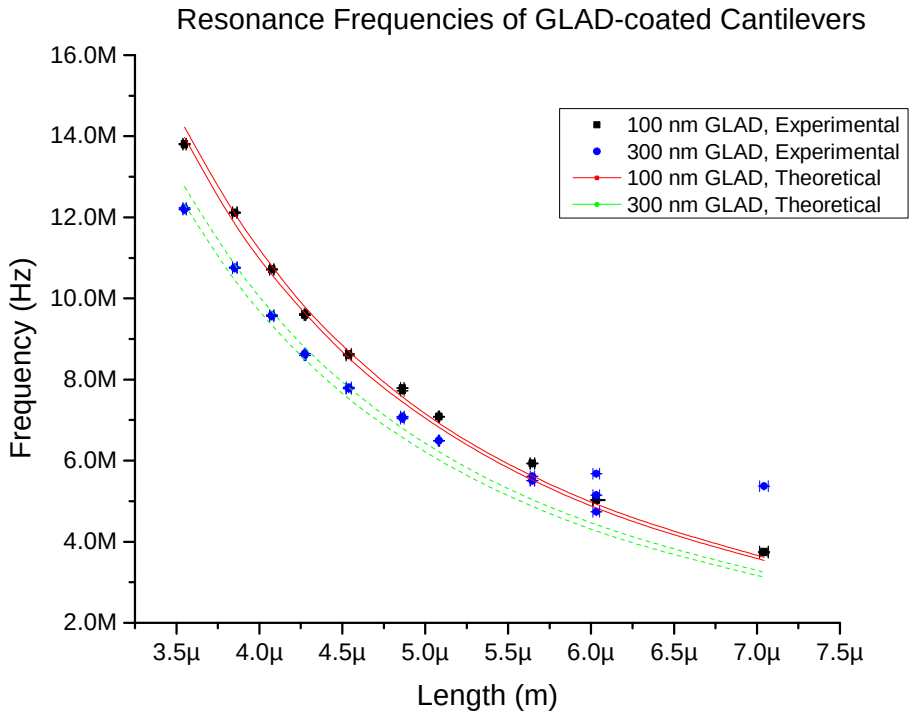

Figure 5.6: Resonance frequencies of 100 nm and 300 nm GLAD-coated cantilevers plotted versus cantilever length. The lines show the upper and lower bounds on the mathematical model derived to predict the resonance frequencies for the 100 nm (solid lines) and 300 nm (dotted lines) GLAD coatings.

The derivation begins with Equation 2.10, the resonance of a cantilever beam. This equation is then modified to take into account the added mass of the GLAD film by modifying ρ. The definition of density is mass divided by volume. The effective density of the resonator and GLAD film together can be expressed as:

$$\rho_{\text{total}} = \frac{M + M_f}{Lwt_b} \tag{5.1}$$

where M is the mass of the beam and M_{f} is the mass of the GLAD film. The volume is simply the volume of the beam, as the GLAD film is extremely porous and adds a negligible volume contribution to the system. Substituting in the mass of the beam and the mass of the film results in Equation 5.2:

$$\rho_{\text{total}} = \frac{t_b\rho + t_f\rho_f}{t_b} \tag{5.2}$$

where ρ_{f} is the film density. Equation 5.2 can be substituted into Equation 2.10 to give a final equation for the resonance of the GLEMS cantilevers:

$$f_0^{\mathrm{C,GLEMS}} = \frac{0.162}{L^2}\sqrt{\frac{Et_b^3}{t_f\rho_f + t_b\rho}} \tag{5.3}$$

This equation accurately predicts the resonance frequencies of the cantilever devices, as shown by Figure 5.6. In Figure 5.6, the solid red lines are the upper and lower boundaries given by Equation 5.3 for the 100 nm GLAD coating. The dotted green lines are the upper and lower bounds given by Equation 5.3 for the 300 nm GLAD coating. The reason upper and lower bounds are necessary is due to the use of experimental parameters in calculating Equation 5.3. For example, t_{b}, L, t_{f}, and ρ_{f} all have errors associated with them as they are experimentally determined parameters. The values for L and t_{b} are those obtained in Chapter 4 (Tables 4.1 and 4.3). The values for film thickness $t_{\mathrm{f}}^{100\mathrm{nm}}$ and $t_{\mathrm{f}}^{300\mathrm{nm}}$ were obtained as described at the beginning of this chapter. The value for ρ_{f} was obtained from Reference [68]. This value was $\rho_{\mathrm{f}} = 500$ kg/m^3, a value specific to vertical post SiO_2 GLAD films deposited at 86°. A 10% error was assigned to this value as it was an experimentally measured parameter with an unknown error.

From Figure 5.6, it can be seen that Equation 5.3 predicts the resonance frequencies very well for the 100 nm thick GLAD coating on the cantilever devices. For the 300 nm thick GLAD coating, the fit begins to degrade as the beam length increases past 5.5 μm. SEM imaging revealed that GLAD film coverage of the beams worsened as the beams length increased. Figure 5.7 shows several cantilever beams. From these images is it easily observed that the long cantilevers have poor GLAD film coverage, whereas coverage improved as the beam length decreases. This lack of coverage caused the theoretical model to differ from experimental results at long cantilever lengths because there less mass than predicted on the beams. This lack of coverage is due to a surface stress introduced by the GLAD film, which bent the beam out of the incoming SiO_2 flux duriing the GLAD deposition. This surface stress was likely caused by the same quasi-continuous layer that caused the quality factor to decrease.

Although the introduction of a surface stress from the GLAD film is not ideal, it provides an avenue to estimate the surface stress caused by the GLAD layer. Ideally, the cantilever deflection could be measured directly and then the stress could be easily calculated. This was attempted using an optical profilometer (Zygo). However, the beams were too small for the optical profilometer to resolve. Contact profilometry was not attempted because the stylus of the contact profilometer was substantially larger than the devices. Since a direct measurement could not

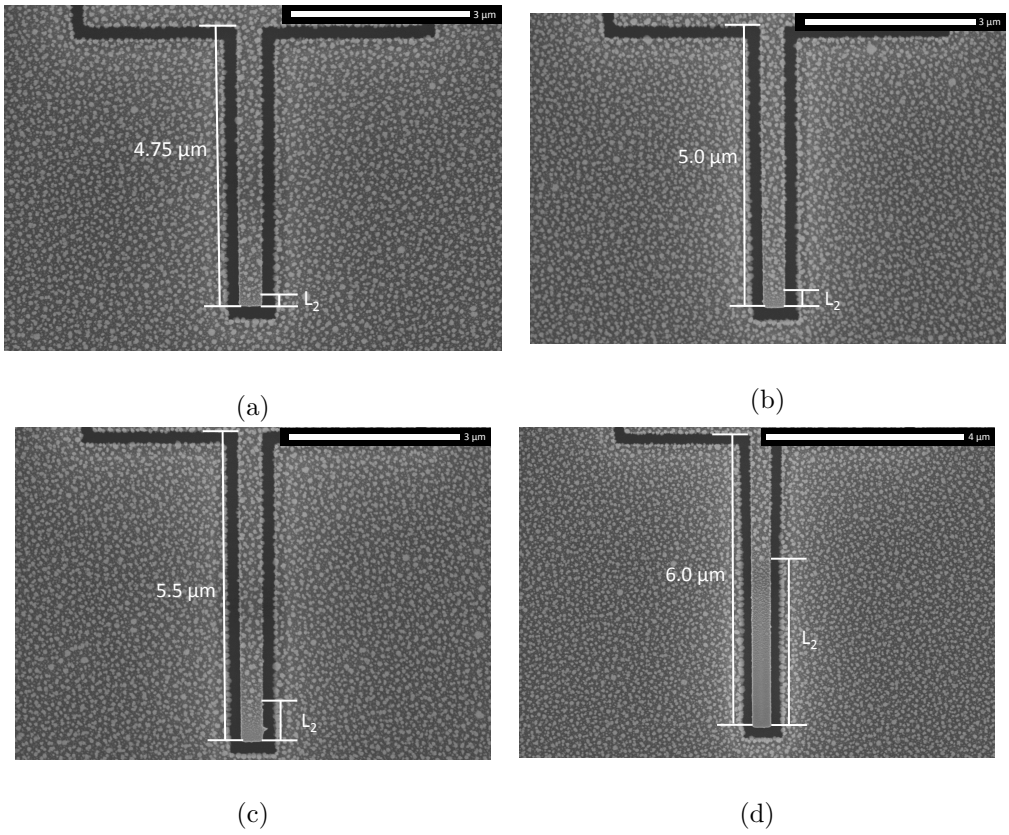

Figure 5.7: 300 nm GLAD coated cantilevers of varying lengths showing the GLAD film coverage. The coverage worsens as the beams increase in length. The nominal beam lengths are (a) 4.75 μm, (b) 5.00 μm, (c) 5.50 μm, and (d) 6.00 μm.

be made, an indirect calculation based on the geometry of the GLAD deposition process was used to estimate the stress.

Due to the geometry of the devices, there is a minimum deflection (Δz_{min}) for which no GLAD will be deposited. Any deflections greater than this minimum deflection will result in no GLAD deposition. Deflections less than Δz_{min} will result in full coverage of the cantilevers. Δz_{min} is calculated from simple geometry based on the deposition angle of $\alpha = 86°$. At deflections larger than Δz_{min}, the side walls will shadow the incoming flux and prevent the GLAD from depositing on the beam. A schematic of how this was calculated is shown in Figure 5.8. In this figure, the dotted green line is Δz_{min}. Any deflections greater than the green line will have no GLAD deposited. Based on the cantilever width of 400 nm and the gap width of 250 nm, $\Delta z_{\text{min}} = 45.5$ nm.

Once the minimum deflection was calculated, the length of cantilever left uncoated by the GLAD deposition process had to be measured for each length of

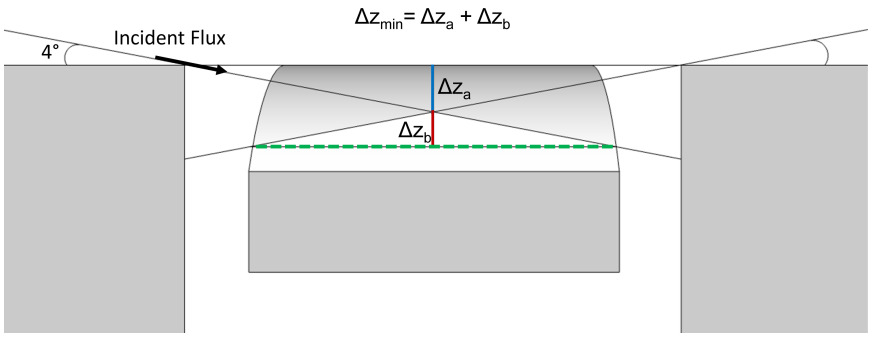

Figure 5.8: The methodology for calculating $\Delta z_{\min}$. This is a simple geometric argument showing that GLAD deposition cannot occur if the cantilever is deflected more than $\Delta z_{\min}$. This is because the side walls shadow the incoming flux. The dotted green line is $\Delta z_{\min}$. This figure shows that $\Delta z_{\min} = \Delta z_{\mathrm{a}} + \Delta z_{\mathrm{b}}$. Since the width of the cantilever is known (400 nm) and the gap width is known (250 nm), $\Delta z_{\min}$ can be easily calculated using simple trigonometry.

cantilever. SEM images of every cantilever length were taken for the devices coated with 300 nm of GLAD film. These images were then processed using ImageJ to measure the uncoated length of cantilever. The uncoated length is called L_2. Each measurement was taken five times and then averaged to produce an average L_2 and a standard deviation that was used as the error in L_2. Only the cantilevers coated with 300 nm of GLAD film were analyzed using this methodology. The 100 nm GLAD-coated cantilevers were excluded because the uncoated length of the beam was extremely difficult to determine. Since the GLAD posts are significantly smaller, it is very difficult to distinguish the fully grown posts from the nucleation layer in the top-down images of the cantilever beams. Figure 5.9 highlights this difficulty well. Comparing Figure 5.9 to any of the cantilevers shown in Figure 5.7, it is clear that L_2 is much easier to measure on the cantilevers coated with 300 nm of GLAD film than the ones coated with only 100 nm of GLAD film. Therefore, only the cantilevers coated with 300 nm of GLAD film were analyzed.

The next step was to calculate the total deflection of each cantilever. This was done using simple geometry, similarly to Reference [100]. A constant radius of curvature (R) was assumed. Figure 5.10 shows the schematic of the cantilever deflection used to calculate the total deflection at the tip of the cantilever (Δz). L_1 is the coated length of the cantilever, and can be calculated from the expression $L \approx L_1 + L_2$ where L is the measured length of the cantilevers obtained in Chapter 4 (Table 4.1). This expression may be slightly inaccurate because L is technically the deflected length of the cantilever, and not the projection of the deflected length onto the x-axis. However, the deflection of the cantilever is very small in comparison to the radius of curvature of the beam, meaning that the length L of the undeflected

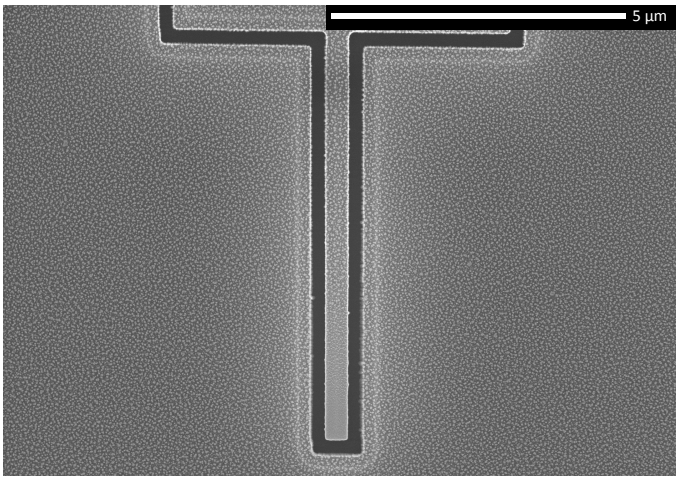

Figure 5.9: A nominally 7 μm long cantilever coated with 100 nm of GLAD film. It is very difficult to determine the point on the beam at which the GLAD ceases to deposit, and so these devices were excluded from the surface stress analysis.

cantilever is approximately equal to $L_1 + L_2$. L_1 could not be measured directly from the SEM images because the undercut caused by the BOE etch is not visible in the SEM images after the NEMS have been coated with GLAD films. This meant the starting point of the beam could not be observed and any measurements of L_1 would be inaccurate because they would not include the undercut. Thus, L_1 had to be calculated using L and L_2.

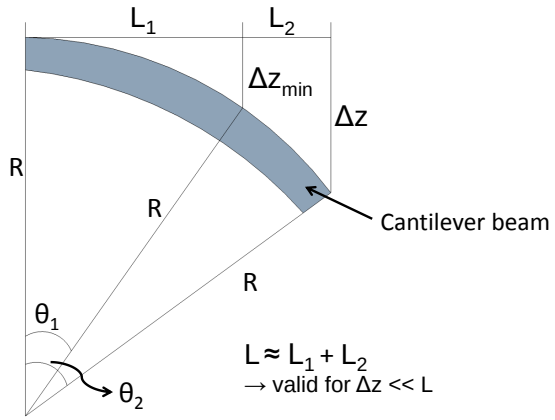

Figure 5.10: The total deflection is calculated using simple geometry based on this figure. L and L_2 are known from SEM images, and therefore L_1 can be calculated using the formula on the figure. The radius of curvature can then be calculated using $\Delta z_{\min}$ and L_1. R and L_2 are then used to calculate θ_2, which can finally be used to calculate Δz.

L_1 and $\Delta z_{\min}$ can be used to calculate the radius of curvature. It was assumed

the deflection at the point where the GLAD coverage ceased was $\Delta z_{\min}$. The next step was to use the radius of curvature to calculate θ_2. This is straightforward using L_2 and R. Finally, the total deflection at the tip of the cantilever was calculated using the following geometric relation [100]:

$$\Delta z = R(1 - \cos\theta_2) \tag{5.4}$$

With the length L and the total deflection Δz obtained, Stoney's formula could then be used to calculate the surface stress present on the cantilever beams [14]. Stoney's formula is a standard equation commonly used to determine the surface stress in cantilevers operating in static detection mode. The equation is as follows:

$$\Delta z = \frac{3(1-\nu)\sigma_s}{Et_b^2}L^2 \tag{5.5}$$

where ν is Poisson's ratio and σ_s is the surface stress caused by the thin film. Poisson's ratio is a material parameter that varies according to the Si crystal plane to which the devices were aligned. The Poisson's ratio corresponding to the Young's modulus of 150 GPa used throughout this thesis is $\nu = 0.235$. This value is an average of the Poisson's ratio of the possible three crystal planes in the (100) Si [91]. In order to find the surface stress, the deflection Δz was plotted against the length squared (L^2). In this plot (Figure 5.11), there are two data points that show a significantly larger deflection than all the other devices. These are the longest cantilevers and have deflections of ~200 nm and greater. These devices are most likely stictioned, as the BOE etch would only etch a depth of ~190 nm underneath the beam, compared to the etch depth in the gaps of ~275 nm. The area under the beam is etched somewhat slower than the gaps because the beam must be etched around before the oxide directly under the beam can be accessed by the BOE. The fact that these two beams, labeled as stictioned in Figure 5.11, have deflections near the etch depth and are much more significantly deflected than the other beams shown in the plot, indicates that these beams are most likely stictioned and should be removed from the analysis.

The remaining data was fit using linear regression. The slope of the fit was used to calculate σ_s using Equation 5.5. From the linear regression, the equation of the line was found to be $y = (962\pm62)\text{m}^{-1}x+(28\pm1)\text{nm}$. Ideally, the y-intercept should be zero. It is near zero, but not zero within error. This means that there is likely some error in the measurements that is unaccounted for. Repeating this experiment with more data points may result in a y-intercept closer to zero. When Equation 5.5 is used to calculate the slope, the result is $\sigma_s = 1.34 \pm 0.09$ N/m (Figure 5.11).

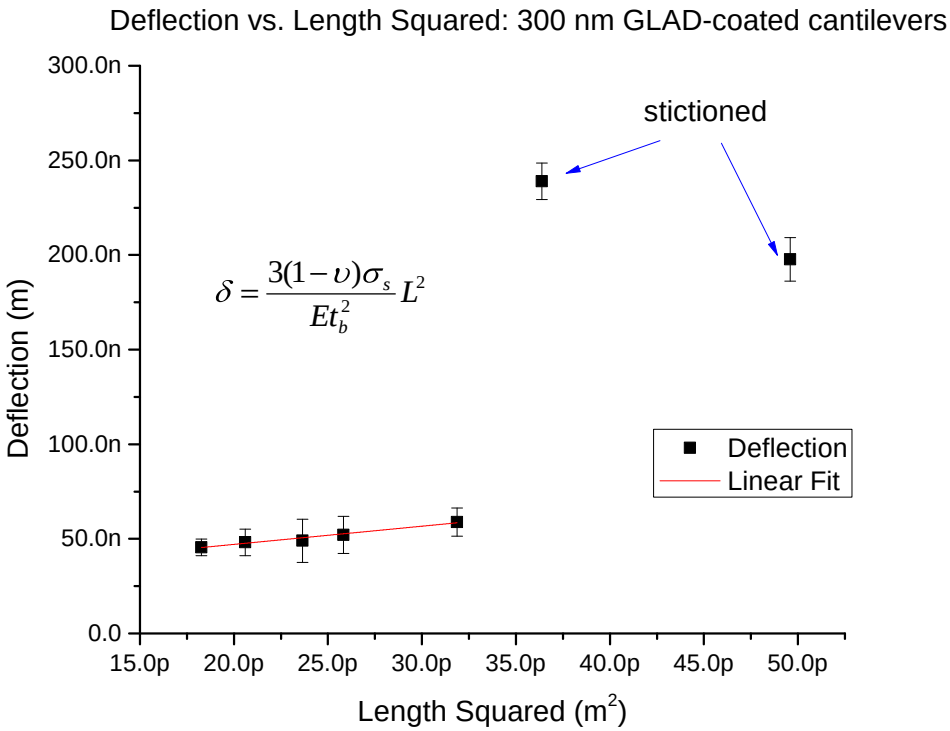

Figure 5.11: The cantilever deflections were plotted versus their length squared in order to find the slope of the linear fit. This slope was then used to calculate the surface stress using Equation 5.5, also shown on this plot. The two points on the right (labeled "stictioned") were excluded from the fit, as their deflections indicated that the beams had become stictioned. This is because their deflections are very close to the depth of the oxide etched out by the BOE.

It should be noted that the surface stress is not a "true" stress because the units are [N/m], instead of [N/m^2]. Rather, σ_s is in the units of a surface energy or interfacial stress [100]. This value cannot be compared directly to other stress values for GLAD in the literature, and so it is necessary to convert this surface stress to a normal stress. An estimate for the overall stress can be obtained by normalizing the surface stress σ_s over the thickness of the beam. Essentially, this means dividing σ_s by the beam thickness t_b. This resulted in a stress induced by the GLAD film on the cantilevers of $\Delta\sigma^{C}_{300nm} = -9.3 \pm 0.6$ MPa. This stress is consistent with that found in Reference [101] for MgF_2 slanted posts deposited at 70°. That study found greater compressive stresses of -20 MPa, however, the vastly different morphologies and deposition angles used in Reference [101] and in this thesis work certainly contribute to the different magnitude of stress observed in the GLAD films.

Although the coverage of the longer cantilevers is incomplete, the shorter can-

tilevers do exhibit full coverage. The resonance frequencies of the shorter cantilevers ($< 5.5\mu$m) are also well predicted by the theoretical model. This means that the shorter cantilevers are the most suitable for use in sensing experiments in the future. The long cantilevers ($> 5.5\mu$m) are not ideal for sensing experiments due to their incomplete coverage. The long cantilevers, however, may be suitable for measuring the stress caused by GLAD films.

5.2.2 Doubly Clamped Beams

Sample resonance frequencies of the coated DCBs are shown in Figure 5.12. These have lower signal-to-noise ratios than the cantilevers, and are typical amplitude responses of the coated DCBs.

The frequency responses of the DCBs were more difficult to analyze than the cantilevers due to the added complexity of the residual stress in the SOI. The model to describe the resonance frequency was derived using the same methodology outlined in the previous section, by substituting in Equation 5.2 into Equation 2.6. This resulted in the following equation:

$$f_0^{\text{DCB,GLAD}} = \frac{1.03t_b}{L^2}\sqrt{\frac{Et_b^3}{\rho t_b + \rho_f t_f} + \frac{\sigma_{tot} t_b L^2}{3.4(\rho t_b + \rho_f t_f)}} \tag{5.6}$$

where σ_{tot} is the total stress due to both the residual stress in the SOI and the additional stress from the GLAD film. This stress is not a surface stress, but rather a bulk stress in units of [Pa]. Figure 5.13 shows the resonance frequencies of the coated DCBs plotted versus the length. The black and blue points are for the 100 nm thick and 300 nm thick coated devices, respectively. The red and green lines are fits to the 100 nm and 300 nm data with σ_{tot} as the fitting variable. The fits are fairly good at longer beam lengths, and relatively poor at shorter beam lengths. This is the same trend that was observed in Chapter 4 for the uncoated DCBs. The same mechanism described in Chapter 4 is likely responsible for these fits diverging at shorter beam lengths.

This data was fit with σ_{tot} as the fitting variable. An initial plot of the data with the theoretical model resulted in the theoretical model being substantially different from the experimental results. After the observations of compressive stress in the coated cantilevers (previous section), it was determined that additional compressive stress was present in the DCBs as well. Therefore, the data was fit using Equation 5.6 with σ_{tot} as the fitting variable. The fit produced $\sigma_{\text{tot}}^{100\text{nm}} = -37.8 \pm 1.1$ MPa for the 100 nm GLAD-coated DCBs. For the 300 nm GLAD-coated DCBs,

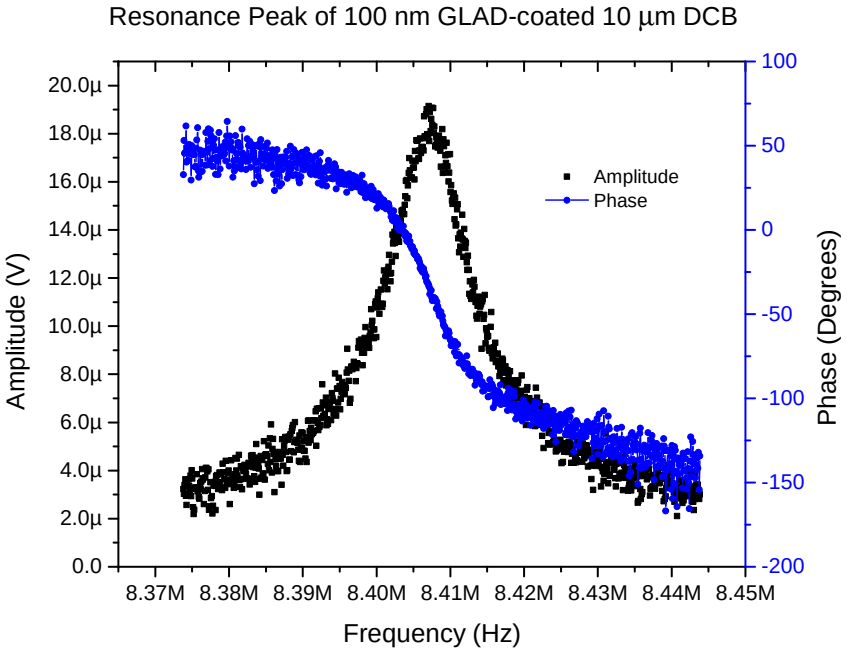

(a)

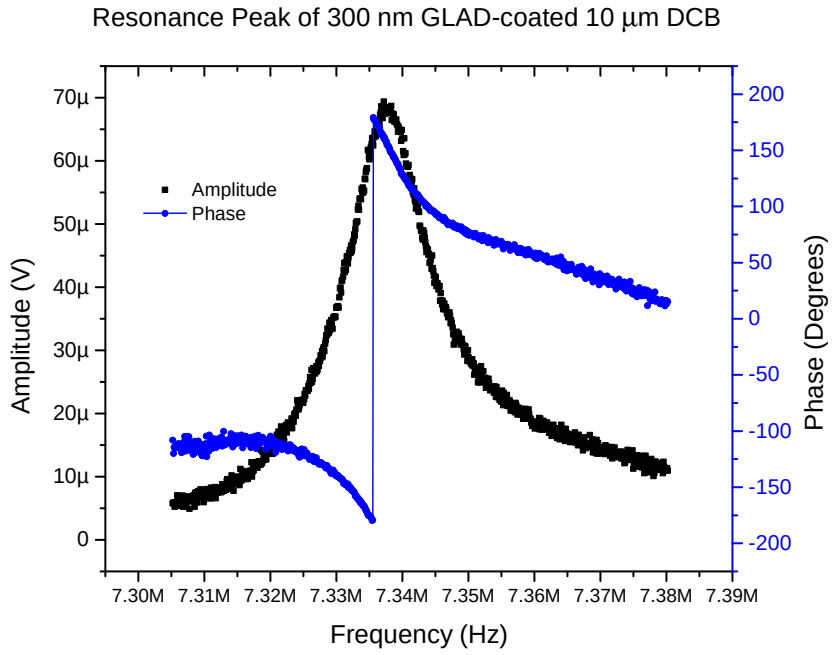

(b)

Figure 5.12: Sample resonance peaks and phase shifts of 10 μm long DCBs that are coated with (a) 100 nm GLAD film and (b) 300 nm GLAD film. The amplitude responses are typical of the coated DCBs.

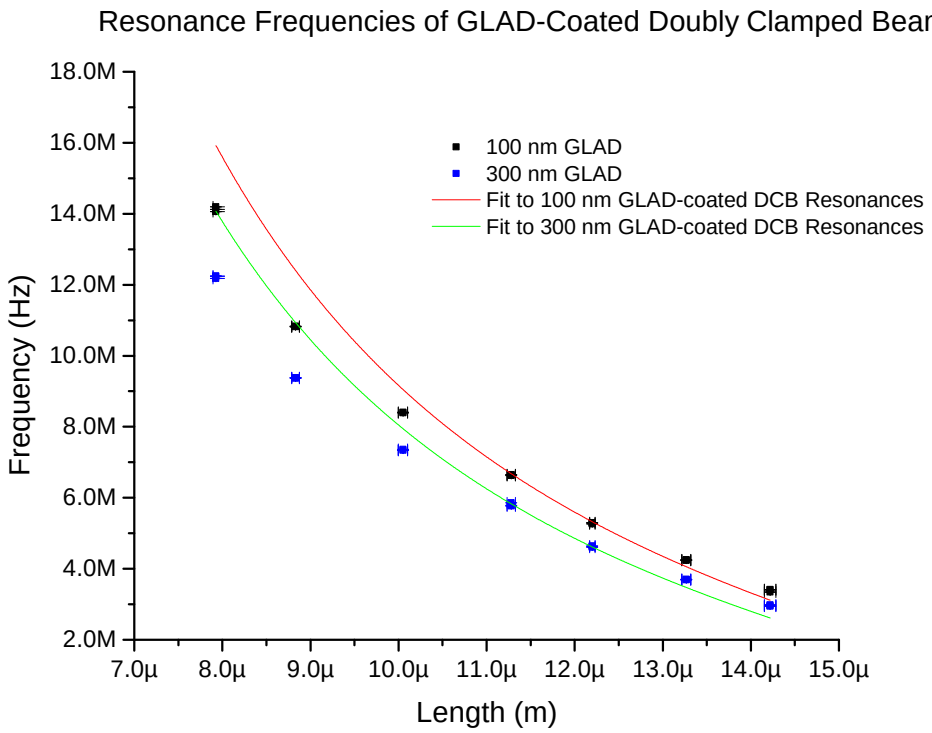

Figure 5.13: Resonance frequencies of the coated DCBs plotted versus the length. The experimental results from the 100 nm and 300 nm GLAD-coated DCBs are shown by the black and blue points, respectively. The red and green lines show fits to the data using Equation 5.6.

$\sigma_{\text{tot}}^{300\text{nm}} = -39.7 \pm 2.0$ MPa. These results agree within error, which indicates that the stress added by the GLAD film is not significantly dependent on the thickness of the film, which is expected if the stress is only introduced by the first few tens of nanometres of GLAD film.

The stress introduced by the GLAD film found in the previous section for the cantilevers can be compared to the additional stress observed for the DCBs. In order to obtain an estimate for the stress caused by the GLAD film growth in the DCBs, the value obtained for σ in Chapter 4 can be substracted from both $\sigma_{\text{tot}}^{100\text{nm}}$ and $\sigma_{\text{tot}}^{300\text{nm}}$. This results in $\Delta\sigma_{100\text{nm}}^{\text{DCB}} = -5.3 \pm 1.1$ MPa, and $\Delta\sigma_{300\text{nm}}^{\text{DCB}} = -7.2 \pm 2.0$ MPa. These results are within error of each other, and the result for the 300 nm GLAD-coated DCBs is within error of the cantilever estimate derived in the previous section. The values are relatively close within error, indicating that the stress caused by the GLAD film can be estimated resonably well using cantilevers or DCBs. The fact that these values are in close agreement also supports the use of Equation 5.6 to model the frequencies of the GLAD-coated DCBs.

The addition of a compressive stress by both the SOI and the GLAD films complicates the analysis of the GLAD-coated DCBs. Despite this, the stress induced by the GLAD film growth can be extracted. This estimate for stress has a relatively high confidence level as the stress calculated for the 100 nm GLAD coated DCBs and the 300 nm GLAD-coated DCBs are within error, and are comparable to the results obtained from the cantilevers. In this way, the DCBs could be used to measure the stress of the GLAD films.

5.3 Phase

Sample phase data plotted against the frequency for GLAD-coated cantilevers is shown in Figure 5.5 for both the 100 nm and 300 nm thick coatings. The same data for the GLAD-coated DCBs is shown in Figure 5.12. It can be seen in these plots that the phase shifts for the 100 nm GLAD-coated cantilevers and DCBs are fairly similar to the phase shifts observed for the uncoated devices, although the signals are noisier. Examining the polar plots for the coated cantilevers shows that the phase shifts are symmetric and the responses begin and end at the origin (Figures 5.14a and 5.14c). For the 300 nm GLAD-coated cantilevers and DCBs, however, there appears to be a background signal in the phase. This is noted by the slope present in the background of the phase signals in Figures 5.5b and 5.12b. In order to examine these phase signals more closely, they have been plotted on polar phase plots in Figures 5.14c and 5.14d for the cantilever and DCB responses, respectively.

The responses shown in Figures 5.14c 5.14d for the 300 nm GLAD-coated devices and are somewhat asymmetric, and the ends of the phase responses do not meet in the origin. These responses represent a middle ground in the data. Some of the responses are nearly symmetric and appear very similar to the uncoated responses. Others exhibit even more asymmetric responses with the tails very far from the origin. The mechanism for this decrease in the quality of the phase signal is uncertain. There is the possibility of a frequency-dependent background. This background is not introduced by the PZ disk because these responses are observed across the frequency spectrum, and not just at frequencies where the PZ disk had a phase signal.

The phase noise should not be introduced by the individual resonances of the GLAD posts. Modeling an individual GLAD post as a cantilever to estimate the resonance frequencies of the posts using Equation 2.10 gives a resonance frequencies in the GHz range. Therefore, any phase response from the individual posts should

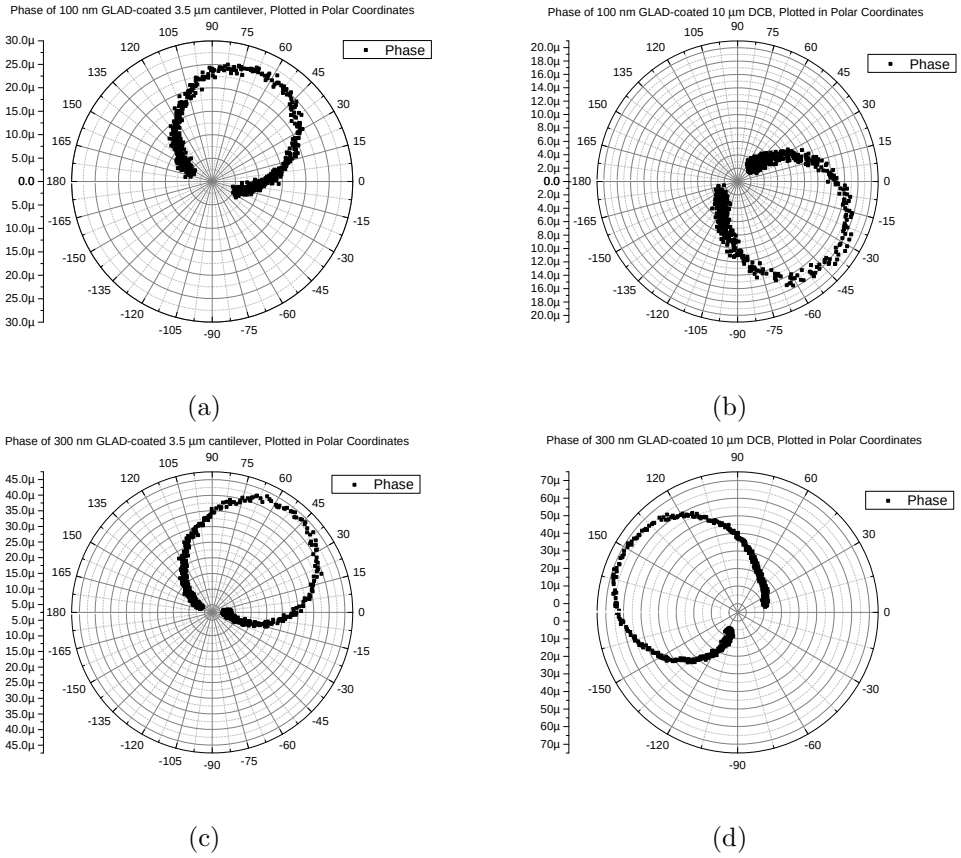

Figure 5.14: Polar phase plots of the coated devices. (a) 100 nm GLAD-coated 3.5 μm long cantilever, (b) 100 nm GLAD-coated 10 μm long DCB, (c) 300 nm GLAD-coated 3.5 μm long cantilever, (d) 300 nm GLAD-coated 10 μm long DCB.

not be visible at the MHz resonance frequencies used in this thesis work. It is possible than an ensemble of posts, a large post, or piece of surface debris on the NEMS, provided some phase background. This may be why the phase response was more asymmetric in some devices than others. Further study of this degradation in phase would be required to ascertain the exact mechanism.

Despite the fact that there was some asymmetry in the phase responses for some of the coated devices, the overall phase responses were still of a high enough quality to be tracked with a phase-locked loop. This means that the GLAD-coated devices would be viable in a sensing experiment requiring this type of technology, which is highly beneficial.

5.4 Summary of GLEMS Analysis

The quality factors, resonance frequencies, and phase responses of the GLEMS have been analyzed. A summary of the important numerical findings is included in Table 5.1. Examination of the quality factors showed an order of magnitude decrease in the Q of the GLEMS compared to the uncoated NEMS. This decrease in Q is most likely due to the quasi-continuous GLAD nucleation layer. This layer is only tens of nanometres thick, and as a result, the Q is unaffected by increasing the GLAD film thickness.

The resonance frequencies of the GLAD-coated cantilevers are well predicted by the model derived in this thesis (Equation 5.3). The resonance frequencies of the GLAD-coated DCBs are predicted reasonably well for long device lengths; however, the resonance frequencies of the shorter devices are overestimated by the derived model (Equation 5.6). This overestimation is consistent with the overestimation observed in the uncoated devices. Therefore, the model fits relatively well; however, an improvement to the original frequency model for the uncoated devices would result in more accurate prediction of the GLEMS DCBs resonance frequencies.

The GLAD film introduced compressive stress into the cantilevers and DCBs. The stress caused by the GLAD film was calculated in both cases. The values of these stresses can be seen below in Table 5.1. These stresses agreed within error or nearly within error of each other, indicating a reasonably accurate estimation of the compressive stress introduced by the GLAD film. Although the introduction of a compressive stress is not ideal for sensing experiments, the GLEMS have demonstrated the capability of quantifying both the magnitude and type of stress.

The GLEMS showed clear 180° phase responses, although some of these responses also showed background phase noise. The source of this phase noise is uncertain and requires more study to determine an exact cause.

Table 5.1: Summary of important results from the GLEMS

t_{f}^{100nm}	=	113.7 ± 1.7 nm
t_{f}^{300nm}	=	324.4 ± 8.0 nm
$\Delta\sigma_{300\mathrm{nm}}^{\mathrm{C}}$	=	-9.3 ± 0.6 MPa
$\Delta\sigma_{100\mathrm{nm}}^{\mathrm{DCB}}$	=	-5.3 ± 1.1 MPa
$\Delta\sigma_{300\mathrm{nm}}^{\mathrm{DCB}}$	=	-7.2 ± 2.0 MPa

Chapter 6

Conclusions

The goal of this thesis work was to develop a fabrication procedure for high surface area nanoelectromechanical systems (NEMS), and to thoroughly characterize the devices. The devices were designed for use in NEMS-based gravimetric sensing applications such as gas chromatography. Glancing angle deposition (GLAD) thin films were used as the high surface area layer. GLAD film properties such as high surface area, low density, and vertical post morphology were highly compatible with NEMS resonators. SiO_2 vertical posts deposited with GLAD at 86° were successfully deposited onto NEMS cantilevers and doubly clamped beams (DCBs) with good film uniformity and limited edge effects. Some of the longer cantilevers were uncoated by GLAD films at the tips of the cantilevers. The short cantilevers and DCBs all displayed full, uniform coverage by the high surface area GLAD films. The GLAD film-coated NEMS were called GLEMS for brevity. To the best of our knowledge, these devices are the first-ever high surface area NEMS.

The quality factors of the GLEMS were one order of magnitude lower than their uncoated counterparts. The reduction in quality factor is most likely due to the presence of a thin, quasi-continuous nucleation layer at the base of the GLAD film. This nucleation layer is sufficiently continuous to act as a viscoelastic layer, which damps the GLEMS substantially. The order-of-magnitude decrease in quality factor is present for both the cantilever and doubly clamped beams.

The resonance frequencies of the GLEMS were lower than the uncoated devices because the GLAD films introduced a mass loading effect. Theoretical models were derived to predict the resonance frequencies of the GLEMS by introducing a density correction into the formulas for resonance frequency. This model predicts the resonance frequencies of the GLEMS cantilevers with a high accuracy. The only exception to this is the longer cantilevers that are incompletely coated by the GLAD films. These cantilevers have higher resonance frequencies than predicted by the

model because there is less mass loading by the film than expected. The model describes the resonance frequencies of the shorter, fully coated, cantilevers within error.

The model accurately describes the resonance frequencies of the long DCBs, however, the model tends to overestimate the frequencies of the short DCBs. This is not a flaw in the model derived in this thesis. Rather, it is a flaw of the equation from the literature used to model the uncoated DCBs. There was an initial residual compressive stress in the substrate from which the devices were fabricated. Therefore, a modified formula for the resonance frequency had to be used to model the uncoated DCBs. This formula is typically used for tensile stress in NEMS, but it is theoretically valid for compressive stress as well. This equation overestimated the resonance frequencies of the shorter uncoated DCBs, and this error was carried through for the short GLAD-coated DCBs. An improved equation describing compressively stressed DCBs would greatly benefit the GLAD-coated DCB frequency model.

It was observed that the GLAD film introduced an additional compressive stress into the GLEMS. This was visually observed in SEM images of the cantilevers. The tips of the cantilevers were uncoated due to a compressive stress introduced by the GLAD film bending the beams out of the path of the incoming vapour flux during deposition. Using a geometrical argument, an estimate of the stress caused by the GLAD film was extracted from the cantilevers. This estimate was corroborated with estimates obtained from curve-fitting to the resonance frequencies of the DCBs. These estimates gave compressive stresses in the range of 5.3–9.3 MPa, comparable to results obtained from other GLAD films in the literature. The introduction of a compressive stress by the GLAD film is undesirable for sensor applications, as it results in the cantilevers being incompletely coated and difficulty in the prediction of the resonance frequencies of the DCBs. However, the quantification of the stress introduced by the GLAD film is useful in and of itself. The longer GLAD-coated cantilevers and the GLAD-coated DCBs may find additional use as stress measurement devices for GLAD films.

6.1 Directions for Future Work

The loss of quality factor is one of the most significant drawbacks of the GLEMS. This may be remedied by introducing a seed layer at the base of the GLAD films. Seeding is a technique where small dots of material are introduced at regular spacings to provide nucleation points for the GLAD films. This can be done using electron beam lithography, nano-imprint lithography, or by performing depositions

of specific materials at high temperatures. The GLAD films are deposited on top of the seeding layer. The benefit of seeded films is that the nucleation points are specifically introduced by the seeds, which means that the semi-continuous layer causing the damping in the GLEMS would be reduced or eliminated. Therefore, the seeding layer would likely improve the quality factor and decrease the stress introduced by the GLAD film.

The next step in this project would be to functionalize the GLAD film using a surface functionalization technique. Ideally, the surface functionalization procedure should not affect the quality factor or the surface stress of the GLEMS, however, the effect of surface functionalization on the GLEMS would have to be determined experimentally.

The most important future work would be to use the GLEMS in a sensing experiment to determine the true effect of the high surface area layer on the sensitivity and limit of detection (LOD). The GLEMS should be compared to uncoated devices to quantify enhancements in sensitivity, LOD, and response time introduced by the GLAD film.

6.2 Summary

High surface area NEMS were successfully fabricated through the deposition of GLAD thin films on already-released NEMS. This is the first report of successful fabrication and characterization of high surface area NEMS. The quality factors and resonance frequencies of the GLEMS were analyzed to provide insights into the device physics. The stress introduced by the GLAD film was quantified. High surface area NEMS may be used as thin film stress sensors, but are primarily suited for surface area enhanced NEMS-based gravimetric sensors.

Bibliography

[1] B. Dick, M. J. Brett, and T. Smy. Controlled growth of periodic pillars by glancing angle deposition. *Journal of Vacuum Science & Technology B*, 21(1):23–28, 2003.

[2] M. T. Taschuk, M. M. Hawkeye, and M. J. Brett. Glancing Angle Deposition. In *Handbook of Deposition Technologies for Films and Coatings: Science, Applications and Technology*, chapter 13, pages 621–678. Elsevier Books, 2010.

[3] S. Fanget, S. Hentz, P. Puget, J. Arcamone, M. Matheron, E. Colinet, P. Andreucci, L. Duraffourg, Ed. Myers, and M.L. Roukes. Gas sensors based on gravimetric detectionA review. *Sensors and Actuators B: Chemical*, 160(1):804–821, December 2011.

[4] H. G. Craighead. Nanoelectromechanical Systems. *Science*, 290(5496):1532–1535, November 2000.

[5] D. Vick, V. Sauer, A. E. Fraser, M. R. Freeman, and W. K. Hiebert. Bulk focused ion beam fabrication with three-dimensional shape control of nanoelectromechanical systems. *Journal of Micromechanics and Microengineering*, 20(10):105005, October 2010.

[6] K. L. Ekinci. Electromechanical transducers at the nanoscale: actuation and sensing of motion in nanoelectromechanical systems (NEMS). *Small*, 1(8-9):786–797, August 2005.

[7] Mo Li, W. H. P. Pernice, C. Xiong, T. Baehr-Jones, M. Hochberg, and H. X. Tang. Harnessing optical forces in integrated photonic circuits. *Nature*, 456:480–4, November 2008.

[8] Mo Li, H. X. Tang, and M. L. Roukes. Ultra-sensitive NEMS-based cantilevers for sensing, scanned probe and very high-frequency applications. *Nature Nanotechnology*, 2(2):114–20, February 2007.

[9] P. Ivaldi, J. Abergel, M. H. Matheny, L. G. Villanueva, R. B. Karabalin, M. L. Roukes, P. Andreucci, S. Hentz, and E. Defaÿ. 50 nm thick AlN film-based piezoelectric cantilevers for gravimetric detection. *Journal of Micromechanics and Microengineering*, 21(8):085023, August 2011.

[10] W. K. Hiebert, D. Vick, V. T. K. Sauer, and M. R. Freeman. Optical interferometric displacement calibration and thermomechanical noise detection in bulk focused ion beam-fabricated nanoelectromechanical systems. *Journal of Micromechanics and Microengineering*, 20(11):115038, November 2010.

[11] J. L. Arlett, J. R. Maloney, B. Gudlewski, M. Muluneh, and M. L. Roukes. Self-Sensing Micro- and Nanocantilevers with Attonewton-Scale Force Resolution. *Nano Letters*, 6(5):1000–1006, May 2006.

[12] V. T. K. Sauer, Z. Diao, M. R. Freeman, and W. K. Hiebert. Nanophotonic detection of side-coupled nanomechanical cantilevers. *Applied Physics Letters*, 100(26):261102, 2012.

[13] K. L. Ekinci and M. L. Roukes. Nanoelectromechanical systems. *Review of Scientific Instruments*, 76(6):061101, 2005.

[14] A. Boisen, S. Dohn, S. S. Keller, S. Schmid, and M. Tenje. Cantilever-like micromechanical sensors. *Reports on Progress in Physics*, 74(3):036101, March 2011.

[15] N. Lobontiu, B. Ilic, E. Garcia, T. Reissman, and H. G. Craighead. Modeling of nanofabricated paddle bridges for resonant mass sensing. *Review of Scientific Instruments*, 77(7):073301, 2006.

[16] X. Zhang, X. Sun, and H. X. Tang. A 1.16-μm radius disk cavity in a sunflower-type circular photonic crystal with ultrahigh quality factor. *Optics Letters*, 37(15):3195–3197, August 2012.

[17] A. Suhel, B. D. Hauer, T. S. Biswas, K. S. D. Beach, and J. P. Davis. Dissipation mechanisms in thermomechanically driven silicon nitride nanostrings. *Applied Physics Letters*, 100(17):173111, 2012.

[18] Q. P. Unterreithmeier, T. Faust, and J. P. Kotthaus. Damping of Nanomechanical Resonators. *Physical Review Letters*, 105(2):027205, July 2010.

[19] O. Y. Loh and H. D. Espinosa. Nanoelectromechanical contact switches. *Nature Nanotechnology*, 7(5):283–95, May 2012.

[20] M. Bagheri, M. Poot, M. Li, W. P. H. Pernice, and H. X. Tang. Dynamic manipulation of nanomechanical resonators in the high-amplitude regime and non-volatile mechanical memory operation. *Nature Nanotechnology*, 6(11):726–732, November 2011.

[21] A. K. Naik, M. S. Hanay, W. K. Hiebert, X. L. Feng, and M. L. Roukes. Towards single-molecule nanomechanical mass spectrometry. *Nature Nanotechnology*, 4(7):445–450, 2009.

[22] Mo Li, E. B. Myers, H. X. Tang, S. J. Aldridge, H. C. McCaig, J. J. Whiting, R. J. Simonson, N. S. Lewis, and M. L. Roukes. Nanoelectromechanical resonator arrays for ultrafast, gas-phase chromatographic chemical analysis. *Nano Letters*, 10(10):3899–903, October 2010.

[23] J. L. Arlett, E. B. Myers, and M. L. Roukes. Comparative advantages of mechanical biosensors. *Nature Nanotechnology*, 6(4):203–215, April 2011.

[24] N. V. Lavrik, M.J. Sepaniak, and P. G. Datskos. Cantilever transducers as a platform for chemical and biological sensors. *Review of Scientific Instruments*, 75(7):2229–2253, 2004.

[25] A. N. Cleland. *Foundations of Nanomechanics*. Springer New York, 2003.

[26] K. L. Ekinci, Y. T. Yang, and M. L. Roukes. Ultimate limits to inertial mass sensing based upon nanoelectromechanical systems. *Journal of Applied Physics*, 95(5):2682–2689, 2004.

[27] R. B. Karabalin, S. C. Masmanidis, and M. L. Roukes. Efficient parametric amplification in high and very high frequency piezoelectric nanoelectromechanical systems. *Applied Physics Letters*, 97(18):183101, 2010.

[28] A. N. Cleland and M. L. Roukes. Noise processes in nanomechanical resonators. *Journal of Applied Physics*, 92(5):2758–2769, 2002.

[29] S. S. Verbridge, J. M. Parpia, R. B. Reichenbach, L. M. Bellan, and H. G. Craighead. High quality factor resonance at room temperature with nanostrings under high tensile stress. *Journal of Applied Physics*, 99(12):124304, 2006.

[30] D. F. Wang, T. Ono, and M. Esashi. Thermal treatments and gas adsorption influences on nanomechanics of ultra-thin silicon resonators for ultimate sensing. *Nanotechnology*, 15(12):1851–1854, December 2004.

[31] A. Bokaian. Natural frequencies of beams under compressive axial loads. *Journal of Sound and Vibration*, 126(1):49–65, 1988.

[32] S. C. Jun, X. M. H. Huang, M. Manolidis, C. A. Zorman, M. Mehregany, and J. Hone. Electrothermal tuning of AlSiC nanomechanical resonators. *Nanotechnology*, 17(5):1506–1511, March 2006.

[33] S. S. Verbridge, D. F. Shapiro, H. G. Craighead, and J. M. Parpia. Macroscopic tuning of nanomechanics: substrate bending for reversible control of frequency and quality factor of nanostring resonators. *Nano Letters*, 7(6):1728–35, June 2007.

[34] H. W. Postma, I. Kozinsky, A. Husain, and M. L. Roukes. Dynamic range of nanotube- and nanowire-based electromechanical systems. *Applied Physics Letters*, 86(22):223105, 2005.

[35] E. Iwase, P.-C. Hui, D. Woolf, A. W. Rodriguez, S. G. Johnson, F. Capasso, and M. Loncar. Control of buckling in large micromembranes using engineered support structures. *Journal of Micromechanics and Microengineering*, 22(6):065028, 2012.

[36] P. Li and X. Li. A single-sided micromachined piezoresistive SiO 2 cantilever sensor for ultra-sensitive detection of gaseous chemicals. *Journal of Micromechanics and Microengineering*, 16(12):2539–2546, December 2006.

[37] Y. Chen, P. Xu, and X. Li. Self-assembling siloxane bilayer directly on SiO2 surface of micro-cantilevers for long-term highly repeatable sensing to trace explosives. *Nanotechnology*, 21(26):265501, July 2010.

[38] H. Duan. Surface-enhanced cantilever sensors with nano-porous films. *Acta Mechanica Solida Sinica*, 23(1):1–12, 2010.

[39] Y. T. Yang, C. Callegari, X. L. Feng, K. L. Ekinci, and M. L. Roukes. Zeptogram-scale nanomechanical mass sensing. *Nano Letters*, 6(4):583–6, April 2006.

[40] M. Bao and H. Yang. Squeeze film air damping in MEMS. *Sensors and Actuators A: Physical*, 136(1):3–27, May 2007.

[41] R. Lifshitz and M. L. Roukes. Thermoelastic damping in micro- and nanomechanical systems. *Physical Review B*, 61(8):5600–5609, February 2000.

[42] P. Mohanty, D. Harrington, K. Ekinci, Y. Yang, M. Murphy, and M. L. Roukes. Intrinsic dissipation in high-frequency micromechanical resonators. *Physical Review B*, 66(8):085416, August 2002.

[43] K. Y. Yasumura, T. D. Stowe, E. M. Chow, T. Pfafman, T. W. Kenny, B. C. Stipe, and D. Rugar. Quality factors in micron-and submicron-thick cantilevers. *Journal of Microelectromechanical Systems*, 9(1):117–125, 2000.

[44] J. Yang, T. Ono, and M. Esashi. Energy dissipation in submicrometer thick single-crystal silicon cantilevers. *Journal of Microelectromechanical Systems*, 11(6):775–783, 2002.

[45] J. A. Judge, D. M. Photiadis, J. F. Vignola, B. H. Houston, and J. Jarzynski. Attachment loss of micromechanical and nanomechanical resonators in the limits of thick and thin support structures. *Journal of Applied Physics*, 101(1):013521, 2007.

[46] D. M. Photiadis and J. A. Judge. Attachment losses of high Q oscillators. *Applied Physics Letters*, 85(3):482–484, 2004.

[47] I. Wilson-Rae. Intrinsic dissipation in nanomechanical resonators due to phonon tunneling. *Physical Review B*, 77(24):245418, June 2008.

[48] R. A. Barton, S. S. Verbridge, D. R. Southworth, B. Ilic, H. G. Craighead, J. M. Parpia, and I. Wilson-Rae. High-Q Nanomechanics via Destructive Interference of Elastic Waves. *Physical Review Letters*, 106(4):047205, January 2011.

[49] M. J. Lachut and J. E. Sader. Effect of surface stress on the stiffness of thin elastic plates and beams. *Physical Review B*, 85(8):085440, February 2012.

[50] Y. T. Yang, C. Callegari, X. L. Feng, and M. L. Roukes. Surface adsorbate fluctuations and noise in nanoelectromechanical systems. *Nano Letters*, 11(4):1753–9, April 2011.

[51] R. Sandberg, K. Mø lhave, A. Boisen, and W. Svendsen. Effect of gold coating on the Q -factor of a resonant cantilever. *Journal of Micromechanics and Microengineering*, 15(12):2249–2253, December 2005.

[52] I. Dufour, F. Lochon, S. M. Heinrich, F. Josse, and D. Rebiere. Effect of coating viscoelasticity on quality factor and limit of detection of microcantilever chemical sensors. *IEEE Sensors Journal*, 7(2):230–236, 2007.

[53] S. Dohn, W. Svendsen, A. Boisen, and O. Hansen. Mass and position determination of attached particles on cantilever based mass sensors. *The Review of Scientific Instruments*, 78(10):103303, October 2007.

[54] S. Dohn, S. Schmid, F. Amiot, and A. Boisen. Position and mass determination of multiple particles using cantilever based mass sensors. *Applied Physics Letters*, 97(4):044103, 2010.

[55] Y. T. Yang, K. L. Ekinci, X. M. H. Huang, L. M. Schiavone, M. L. Roukes, C. A. Zorman, and M. Mehregany. Monocrystalline silicon carbide nanoelectromechanical systems. *Applied Physics Letters*, 78(2):162–164, 2001.

[56] V. Sazonova, Y. Yaish, H. Ustünel, D. Roundy, T. A. Arias, and P. L. McEuen. A tunable carbon nanotube electromechanical oscillator. *Nature*, 431:284–7, September 2004.

[57] J. Chaste, A. Eichler, J. Moser, G. Ceballos, R. Rurali, and A. Bachtold. A nanomechanical mass sensor with yoctogram resolution. *Nature Nanotechnology*, 7(5):301–304, May 2012.

[58] W. K. Hiebert. Mass sensing: Devices reach single-proton limit. *Nature nanotechnology*, 7(5):278–280, May 2012.

[59] B. Ilic, H. G. Craighead, S. Krylov, W. Senaratne, and C. Ober. Attogram detection using nanoelectromechanical oscillators. *Journal of Applied Physics*, 95(7):3694–3703, 2004.

[60] M. Li, R. B. Bhiladvala, T. J. Morrow, J. A. Sioss, K.-K. Lew, J. M. Redwing, C. D. Keating, and T. S. Mayer. Bottom-up assembly of large-area nanowire resonator arrays. *Nature Nanotechnology*, 3(2):88–92, February 2008.

[61] J. A. Sioss, R. B. Bhiladvala, W. Pan, M. Li, S. Patrick, P. Xin, S. L. Dean, C. D. Keating, T. S. Mayer, and G. A. Clawson. Nanoresonator chip-based RNA sensor strategy for detection of circulating tumor cells: response using PCA3 as a prostate cancer marker. *Nanomedicine: Nanotechnology, Biology, and Medicine*, 8(6):1017–25, August 2012.

[62] J. Arcamone, A. Niel, V. Gouttenoire, M. Petitjean, N. David, R. Barattin, M. Matheron, F. Ricoul, T. Bordy, H. Blanc, J. Ruellan, D. Mercier, G. Costa, V. Agache, S. Hentz, J. C Gabriel, F. Baleras, C. Marcoux, T. Ernst, L. Duraffourg, E. Colinet, E.B. B Myers, M.L. L Roukes, P. Andreucci, E. Ollier, P. Puget, and N. Pereira-Rodrigues. VLSI silicon multi-gas analyzer coupling gas chromatography and NEMS detectors. In *2011 International Electron Devices Meeting*, number 5, pages 29.3.1–29.3.4. IEEE, December 2011.

[63] D. A. Rider, R. T. Tucker, B. J. Worfolk, K. M. Krause, A. Lalany, M. J. Brett, J. M. Buriak, and K. D. Harris. Indium tin oxide nanopillar electrodes in polymer/fullerene solar cells. *Nanotechnology*, 22(8):085706, February 2011.

[64] J. J. Steele, A. C. van Popta, M. M. Hawkeye, J. C. Sit, and M. J. Brett. Nanostructured gradient index optical filter for high-speed humidity sensing. *Sensors and Actuators B: Chemical*, 120(1):213–219, December 2006.

[65] M. M. Hawkeye and M. J. Brett. Glancing angle deposition: Fabrication, properties, and applications of micro- and nanostructured thin films. *Journal of Vacuum Science & Technology A: Vacuum, Surfaces, and Films*, 25(5):1317–1335, 2007.

[66] K. Robbie, J. C. Sit, and M. J. Brett. Advanced techniques for glancing angle deposition. *Journal of Vacuum Science & Technology B*, 16(3):1115–122, May 1998.

[67] M. O. Jensen and M. J. Brett. Periodically structured glancing angle deposition thin films. *IEEE Transactions on Nanotechnology*, 4(2):269–277, 2005.

[68] K. M. Krause, M.T. Taschuk, K. D. Harris, D. A. Rider, N. G. Wakefield, J. C. Sit, J. M. Buriak, M. Thommes, and M. J. Brett. Surface area characterization of obliquely deposited metal oxide nanostructured thin films. *Langmuir*, 26(6):4368–76, March 2010.

[69] P. C. P. Hrudey, K. L. Westra, and M. J. Brett. Highly Ordered Organic Alq3 Chiral Luminescent Thin Films Fabricated by Glancing-Angle Deposition. *Advanced Materials*, 18(2):224–228, January 2006.

[70] B. Dick, M. J. Brett, T. J. Smy, M. R. Freeman, M. Malac, and R. F. Egerton. Periodic magnetic microstructures by glancing angle deposition. *Journal of Vacuum Science & Technology A*, 18(4):1838, 2000.

[71] J. J. Steele, J. P. Gospodyn, J. C. Sit, and M. J. Brett. Impact of morphology on high-speed humidity sensor performance. *IEEE Sensors Journal*, 6(1):24–27, February 2006.

[72] N. A. Beckers, M. T. Taschuk, and M. J. Brett. Selective room temperature nanostructured thin film alcohol sensor as a virtual sensor array. *Sensors and Actuators B: Chemical*, 176:1096–1102, January 2013.

[73] K. M. Krause and M. J. Brett. Spatially Graded Nanostructured Chiral Films as Tunable Circular Polarizers. *Advanced Functional Materials*, 18(20):3111–3118, October 2008.

[74] P. Hajireza, K. Krause, M. J. Brett, and R. Zemp. Glancing angle deposited nanostructured film Fabry-Perot etalons for optical detection of ultrasound. *Optics Express*, 21(5):6391–6400, March 2013.

[75] J. K. Kwan and J. C. Sit. High sensitivity Love-wave humidity sensors using glancing angle deposited thin films. *Sensors and Actuators B: Chemical*, 173:164–168, October 2012.

[76] A. L. Elias, K. D. Harris, and M. J. Brett. Fabrication of Helically Perforated Gold, Nickel, and Polystyrene Thin Films. *Journal of Microelectromechanical Systems*, 13(5):808–813, October 2004.

[77] P. Stempflé, A. Besnard, N. Martin, A. Domatti, and J. Takadoum. Accurate control of friction with nanosculptured thin coatings: Application to gripping in microscale assembly. *Tribology International*, 59:67–78, March 2013.

[78] Derek Strembicke, A. M. Robinson, F E Venneulen, Mary Set, Keith B. Brown, F. E. Vermeulen, and M. Seto. Humidity measurement using resonating CMOS microcantilever structures. In *Proceedings of the 1999 IEEE Canadian Conference on Electrical and Computer Engineering*, pages 1658–1661, 1999.

[79] S. Tsoi, E. Fok, J. C. Sit, and J. G. C. Veinot. Surface functionalization of porous nanostructured metal oxide thin films fabricated by glancing angle deposition. *Chemistry of Materials*, 18(22):5260–5266, 2006.

[80] J. J. Steele, M. T. Taschuk, and M. J. Brett. Response time of nanostructured relative humidity sensors. *Sensors and Actuators B: Chemical*, 140(2):610–615, July 2009.

[81] G. Celler and M. Wolf. Smart-Cut: A guide to the technology, the process, the products. Technical report, 2003.

[82] J.-G. Fan, D. Dyer, G. Zhang, and Y.-P. Zhao. Nanocarpet Effect: Pattern Formation during the Wetting of Vertically Aligned Nanorod Arrays. *Nano Letters*, 4(11):2133–2138, November 2004.

[83] J.-G. Fan, J.-X. Fu, A. Collins, and Y.-P. Zhao. The effect of the shape of nanorod arrays on the nanocarpet effect. *Nanotechnology*, 19(4):045713, January 2008.

[84] J. K. Kwan and J. C. Sit. The use of ion-milling to control clustering of nanostructured, columnar thin films. *Nanotechnology*, 21(29):295301, 2010.

[85] M. Seto, K. Westra, and M. J. Brett. Arrays of self-sealed microchambers and channels. *Journal of Materials Chemistry*, 12(8):2348–2351, July 2002.

[86] D. Sander and H. Ibach. Experimental determination of adsorbate-induced surface stress: Oxygen on Si(111) and Si(100). *Physical Review B*, 43(5):4263–4267, 1991.

[87] X. Zhang, T. Y. Zhang, M. Wong, and Y. Zohar. Residual-stress relaxation in polysilicon thin films by high-temperature rapid thermal annealing. *Sensors and Actuators A: Physical*, 64(1):109–115, 1998.

[88] X. Ding, W. H. Ko, and J. M. Mansour. Residual stress and mechanical properties of boron-doped p+-silicon films. *Sensors and Actuators A: Physical*, 23(1-3):866–871, April 1990.

[89] H. Guckel, D. W. Burns, C. C. G. Visser, H. A. C. Tilmans, and D. Deroo. Fine-grained polysilicon films with built-in tensile strain. *IEEE Transactions on Electron Devices*, 35(6):800–801, June 1988.

[90] S. C. Jun, H. Son, C. W. Baik, J. M. Kim, S. W. Moon, H. J. Kim, X. M. H. Huang, and J. Hone. Electrothermal noise analysis in frequency tuning of nanoresonators. *Solid-State Electronics*, 52(9):1388–1393, September 2008.

[91] M. A . Hopcroft, W. D. Nix, and T. W. Kenny. What is the Young's Modulus of Silicon? *Journal of Microelectromechanical Systems*, 19(2):229–238, 2010.

[92] M. T. Postek. An approach to the reduction of hydrocarbon contamination in the scanning electron microscope. *Scanning*, 18:269–274, 1996.

[93] J. Yang, T. Ono, and M. Esashi. Surface effects and high quality factors in ultrathin single-crystal silicon cantilevers. *Applied Physics Letters*, 77(23):3860–3862, 2000.

[94] Douglas C. Montgomery. *Design and Analysis of Experiments*. John Wiley & Sons, 7th edition, 2008.

[95] John Robert Taylor. *An Introduction to Error Analysis: The Study of Uncertainties in Physical Measurements*. University Science Books, 2nd edition, 1997.

[96] OriginLab. Origin 9.0, 2012.

[97] N. Kacem, S. Hentz, D. Pinto, B. Reig, and V. Nguyen. Nonlinear dynamics of nanomechanical beam resonators: improving the performance of NEMS-based sensors. *Nanotechnology*, 20(27):275501, July 2009.

[98] G. H. Hunt. *Effects of In-Situ Temperature Control on the Nanostructure of Glancing Angle Deposition Thin Films*. Msc, University of Alberta, 2013.

[99] J. E. Sader, I. Larson, P. Mulvaney, and L. R. White. Method for the calibration of atomic force microscope cantilevers. *Review of Scientific Instruments*, 66(7):3789–3798, 1995.

[100] D. W. Dareing and T. Thundat. Simulation of adsorption-induced stress of a microcantilever sensor. *Journal of Applied Physics*, 97(4):043526, 2005.

[101] C.-C. Jaing, M.-C. Liu, C.-C. Lee, W.-H. Cho, W.-T. Shen, C.-J. Tang, and B.-H. Liao. Residual stress in obliquely deposited MgF2 thin films. *Applied Optics*, 47(13):C266–70, May 2008.

Appendix A

Gnuplot Curve Fitting

```
#curve fitting using lorentzian for resonance
measurements

FIT_LIMIT = 1e-20

set fit errorvariables

#initial parameters
a=2e7
yo=-1.6437e-5
fo=4.95215e6
q=190.878

#defining function, for derivation see Nanomechanics by Cleland

lorentzian(x)=yo+a*sqrt(1/((x**2-fo**2)**2+(fo**2/q)**2))

#fitting function

fit lorentzian(x) '12_6.001.dat' every ::5 using 1:2 via a, yo, fo, q
plot '12_6.001.dat' every ::5, lorentzian(x)
save var '12_6.txt'
```

The code used to fit the resonance curves is shown above. The Lorenztian function is Equation 2.19. The code was run for each resonance curve. The values were initialized based on a visual inspection of the curve. If the values were initialized too far from the actual values, the code would not converge, and so choosing appropriate initial values was important. The code was typically run several times for each curve in order to improve the initial conditions and obtain the fit with minimal error.